**Diogo Rafael
Bento Barros**

**Impacto e Compensação da Largura de Banda
Vídeo em Amplificadores de Potência de Elevado
Rendimento**

**Video-Bandwidth Impact and Compensation in
Wideband High-Efficiency Power Amplifiers**

**Diogo Rafael
Bento Barros**

**Impacto e Compensação da Largura de Banda
Vídeo em Amplificadores de Potência de Elevado
Rendimento**

**Video-Bandwidth Impact and Compensation in
Wideband High-Efficiency Power Amplifiers**

Tese apresentada à Universidade de Aveiro para cumprimento dos requisitos
necessários à obtenção do grau de Doutor no Programa Doutoral em Engen-
haria Eletrotécnica, realizada sob a orientação científica do Doutor Pedro
Miguel da Silva Cabral, Professor Auxiliar do Departamento de Eletrónica
Telecomunicações e Informática da Universidade de Aveiro e sob a coori-
entação científica do Doutor José Carlos Esteves Duarte Pedro, Professor
Catedrático do Departamento de Eletrónica Telecomunicações e Informática
da Universidade de Aveiro.

o júri / the jury

Presidente / President   **Doutor Vitor José Babau Torres**
                                Professor Catedrático da Universidade de Aveiro

Vogais / Members   **Doutor Nuno Miguel Gonçalves Borges de Carvalho**
                                Professor Catedrático da Universidade de Aveiro

                                Doutora Taylor Wallis Barton
                                Professora Associada, University of Colorado Boulder

                                Doutor João Manuel Torres Caldinhas Simões Vaz
                                Professor Auxiliar, Universidade de Lisboa

                                Doutor Manuel Cândido Duarte dos Santos
                                Professor Auxiliar, Universidade do Porto

                                Doutor Pedro Miguel da Silva Cabral (Orientador)
                                Professor Auxiliar, Universidade de Aveiro

agradecimentos

palavras-chave   Amplificador de potência, banda-larga, distorção não-linear, impedância de banda-base, largura-de-banda vídeo, modelação de amplificadores, multibanda concorrente, radiofrequência, rendimento energético

resumo   O objetivo deste trabalho é determinar, quantificar e modelar a degradação do desempenho de amplificadores de banda-larga quando submetidos a excitação multi-banda concorrente, com particular ênfase na variação do rendimento energético. As origens desta degradação são devidas a duas das principais propriedades do transístor: a geração de corrente em banda-base na saída pela variação não-linear da transcondutância, e a geração de corrente de banda-base na entrada pela variação não-linear da capacidade interna porta-fonte. Cada um destes mecanismos é analisado isoladamente, primeiro por uma explicação qualitativa e intuitiva dos processos que levam à degradação de eficiência observada e, em seguida, através da derivação de modelos que permitem a previsão da degradação do rendimento médio em função da largura de banda do sinal de entrada. O conhecimento resultante foi utilizado para melhorar o desenvolvimento de malhas de adaptação, por forma a otimizar as terminações de impedância em banda-base e previnir a degradação do rendimento. Os modelos desenvolvidos foram validados experimentalmente em vários amplificadores de potência implementados com transístores de tecnologia GaN HEMT, utilizando malhas de adaptação convencionais e otimizadas, onde se obteve 400MHz de largura de banda instantânea sem degradação do rendimento. A consolidação dos mecanismos de degradação descritos neste trabalho são um importante passo para a modelação e projeto de amplificadores de elevado rendimento e largura-de-banda para os sistemas de comunicação multi-banda concorrente convencionais e do futuro.

| keywords | Amplifier modelling, baseband impedance, concurrent multi-band, energy efficiency, video bandwidth, nonlinear distortion, power amplifier, radiofrequency, wideband |

| abstract | The aim of this work is to determine, quantify and model the performance degradation of wideband power amplifiers when subject to concurrent multi-band excitation, with a particular focus on the average efficiency variation. The origins of this degradation are traced to two main transistor properties: the output baseband current generation by the nonlinear transconductance, and the input baseband current generation by the nonlinear gate-source capacitance variation. Each mechanism is analysed separately, first by providing a qualitative and intuitive explanation of the processes that lead to the observed efficiency degradation, and then by deriving models that allow the prediction of the average efficiency dependence with the input signal bandwidth. The resulting knowledge was used to improve matching network design, in order to optimize baseband impedance terminations and prevent the efficiency degradation. The derived models were experimentally validated with several PA prototypes implemented with Gallium Nitride HEMT devices, using both conventional and optimized baseband impedance matching networks, achieving over 400MHz instantaneous bandwidth with uncompromised efficiency. The consolidation of the wideband degradation mechanisms described in this work are an important step for modelling and design of wideband, high-efficiency power amplifiers in current and future concurrent multi-band communication systems. |

Contents

List of Figures

List of Acronyms

2G 2nd Generation

5G 5th Generation

ACPR adjacent channel power ratio

AMAM amplitude modulation to amplitude modulation

CDMA Code Division Multiple Access

CPA Chireix power amplifier

CW continuous wave

DPA Doherty power amplifier

DPD digital pre-distortion

DISO double-input single-output

DLM dynamic load modulation

DOPA Doherty-Outphasing power amplifier

DSP digital signal processing

EER envelope elimination and restoration

ET envelope tracking

FWA fixed wireless access

LMBA load modulated balanced amplifier

IMD intermodulation distortion

IMS International Microwave Symposium

IoT Internet of Things

LUT look-up table

LTE Long-Term Evolution

M2M machine-to-machine

MIMO multiple-input multiple-output

MISO multiple-input single-output

PA power amplifier

PAPR peak-to-average power ratio

PUF power utilization factor

OFDM Orthogonal Frequency-division Multiplexing

OPBO output power back-off

QAM Quadrature Amplitude Modulation

QPSK Quadrature Phase Shift Keying

QWTL quarter-wavelength transmission line

RF radiofrequency

RFPA radiofrequency power amplifier

TMTT Transactions on Microwave Theory and Techniques

VBW video bandwidth

ZVDS zero-voltage derivative switching

ZVS zero-voltage switching

Chapter 1

Background and Motivation

Wireless communication systems have revolutionized the world as we know it by providing the means to exchange information anytime and anywhere around the globe. The number of users and connected devices has been steadily increasing ever since, and the resulting traffic volume and data rate demand shape the evolution of wireless systems and infrastructures.

The evolution of the global data traffic from Q1 2014 to Q1 2021 is presented in Fig.1.1. Currently, global mobile data traffic is increasing at an yearly rate of 46%, fueled by both higher consumed data volume by mobile subscription and the number of smartphone subscriptions, which are projected to increase by 1.7 billion, or 28%, by 2026 [1]. The main social driving factors for these figures include the easy and affordable access to more powerful smartphone devices and to demanding web content, mainly video streaming, at anytime, and anywhere. The volume of the consumed data will only tend to increase, as higher resolution video streaming becomes more and more prevalent in social media, such as news and social networks. These factors are expected to remain in the near future as the penetration rate of 5G continues to increase to a projected 3.5 billion users by 2026, reaching 40% of all subscriptions and further stimulating the data traffic consumption [1].

It is estimated that by 2024 the data volume consumed by smartphones will increase nearly four times, reaching 21 GB of data per month and per user. Additionally, we are at the advent of large scale machine-to-machine (M2M) communications, also known as the Internet of Things (IoT), allowing virtually any object to connect and exchange information with one another. Currently, IoT installments are, mainly, low throughput sensing, monitoring and data control applications that use 2nd Generation (2G) devices and that do not represent a significant part of the data traffic. However, this reality can quickly change as Long-Term Evolution (LTE) network improvements and 5th Generation (5G) technology will allow the deployment of systems for other types of applications, such as drone and autonomous vehicular communications, that despite their lower number of connected devices, can generate much higher data volume.

Fifth generation comercial systems also achieve higher data rates allowing service providers to expand fixed wireless access (FWA) service offerings and compete with DSL and even fiber optic solutions in cases where the deployment cost is prohibitively high. Projections estimate that the total mobile data traffic will increase by a factor of five over the next six years, where 20% is accounted by FWA services [1]. To cope with these figures, and to be able to serve the increasing number of users, mobile networks need to be improved to attain higher capacity. Simply increasing the transmitted power is not a viable solution

since it would require a unsustainable amount of energy with severe health and environmental implications. Therefore, the capacity of mobile networks must be improved through higher data rate, spectral efficiency and energy efficiency, i.e., lower the energy required to transmit the same amount of information. Consequently, bandwidth and energy efficiency have become two of the most important factors that shape the evolution of wireless communication systems.
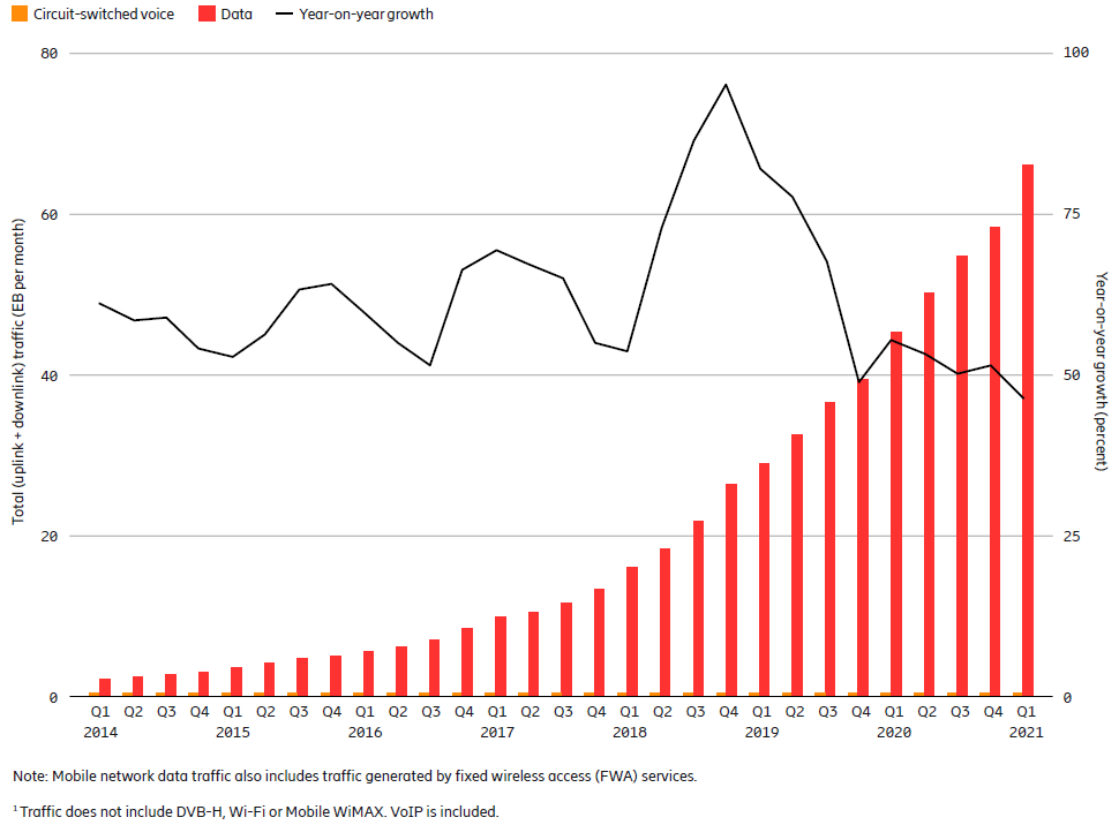
Figure 1.1: Evolution of the global mobile data traffic from Q1 2014 to Q1 2021, as reported in [1].

A typical wireless network energy consumption chain is presented in Fig. 1.2. Wireless communications networks have initially evolved to promote the quality and reliability of the network by focusing on data rate, coverage, capacity and spectral efficiency. As a result, the capability to respond to unexpected traffic peaks or other events by allowing redundancy on the network became common practice, at the cost of more resources being allocated, even when the traffic is low [2]. Therefore, since this power is not actually converted into transmitted power outside of peak times, it is effectively wasted.

As of 2011, as reported in [3, 4], the power consumed by base-stations amounts to 80% of the total energy sent to telecommunication sites. Multiple techniques for efficient energy management at base-station have been investigated, such as optimized sleep-mode [5–7], resource allocation [8] and caching [9, 10]. The typical power consumption of each element in macro and micro cells is presented in Fig. 1.3 where it can be seen that the high power radiofrequency power amplifiers (RFPAs), i.e. the transmitter's output stage, are the most power demanding elements.
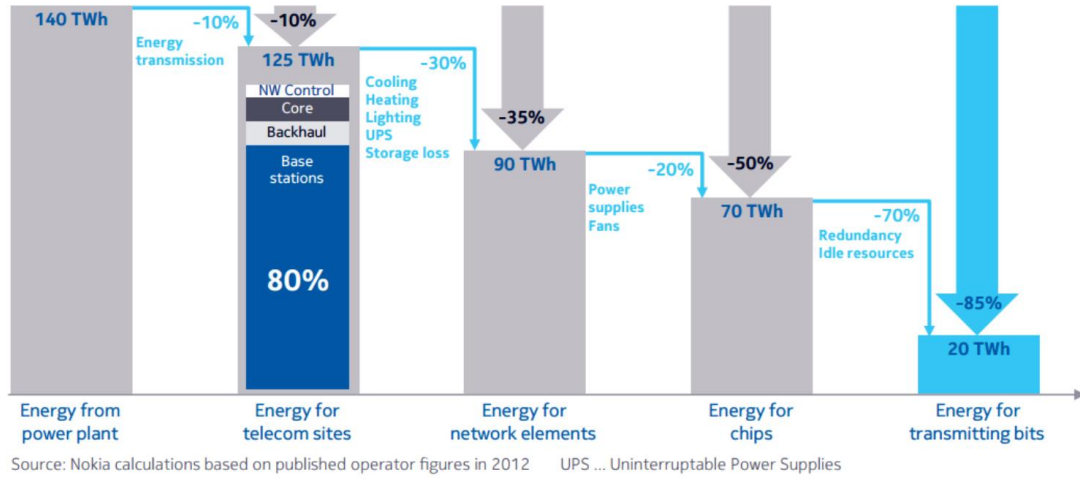
Figure 1.2: Typical energy transfer chain between the different sites and elements in a wireless telecommunications network. Source: [11]
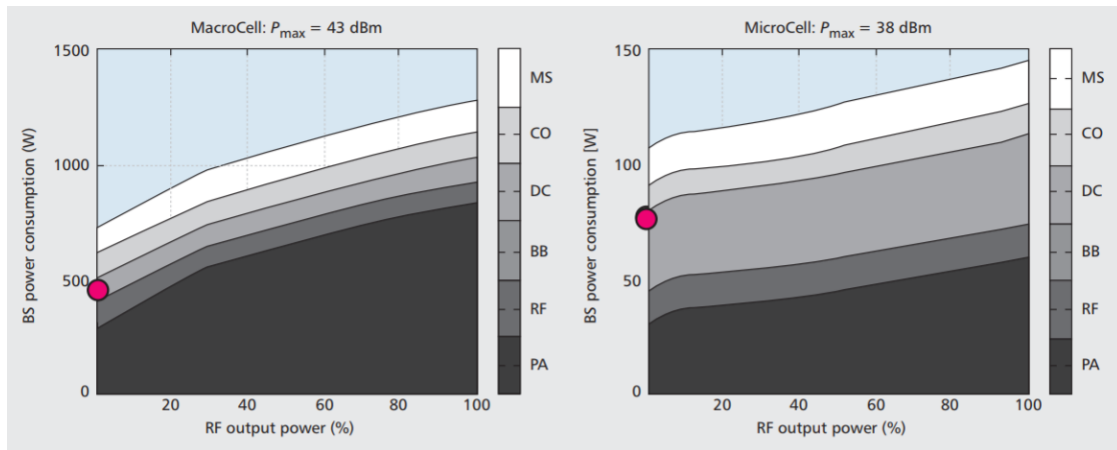
Figure 1.3: Base-station power consumption as a function of the load percentage for macro and micro cells, operating with 10MHz LTE and 2x2 MIMO. The specified elements are the power amplifier - PA, small signal RF transceiver - RF, baseband processor - BB, DC-DC converters - DC, active cooling - CO, main power supply - MS. Source: [3].

Power dissipation is one of the most important factors in commercial base-station transmitters as it not only contributes directly to increased operational costs through energy waste, but also to the installation costs since large cooling hardware occupies additional volume and adds weight to the transmitter, both of which have caps depending on the rented location. Therefore, the PAs' energetic efficiency is of paramount importance to the total energy consumption and cost minimization of the base-station, especially for macro cells. In MIMO applications the power consumed by the digital baseband processing units also becomes significantly higher depending on the complexity of the system.

The efficiency of conventional single-ended power amplifiers is strongly dependent on the output power level at which they are excited, being most efficient when driven close to their maximum power capabilities. However, in order to maximize the capacity and spectral efficiency, the peak-to-average power ratio (PAPR) and bandwidth of wireless communication signals have increased substantially and both can lead to severe efficiency and linearity degradation.

The high signal PAPR forces the PA to be designed to reach the peak power requirement but is operated, on average, at a much lower output power, where the efficiency is substantially lower. To mitigate the average efficiency loss, several advanced design techniques have been proposed in the literature to extend the high efficiency region to lower output power levels, such as dynamic load modulation (DLM), envelope tracking (ET) and envelope elimination and restoration (EER). The wide bandwidth of wireless signals can also lead to performance degradation. Although wide bandwidth can be achieved using more complex design techniques, such as the continuous modes that extend the design space of traditional classes of operation, there are phenomena that do not depend on the CW performance alone. For instance, research has reported substantial efficiency and linearity degradation due to memory effects introduced at the baseband frequencies by the impedance terminations, mainly imposed by the bias circuitry in the matching networks. These phenomena may lead not only to higher digital pre-distortion (DPD) complexity to achieve the required linearity level, but also to a substantially lower average efficiency than predicted from CW performance, which is only accurate for narrowband operation.

The analysis and modelling of the dynamic phenomena that occur in wideband PAs can lead to improved design techniques to ensure optimal performance, which is a valuable step in the development of wireless communication systems. Therefore, this has emerged in recent years as a research hot-topic and is the main focus of this work.

Chapter 2

State-of-the-Art

The aim of this research work is to study and improve the design of wideband, high efficiency PAs by taking into account the dynamic phenomena due to concurrent band excitation. In order to support this objective, the most recent research and publications on the topics related to power amplifier design, high efficiency architectures and wideband performance will be presented in this section. To the best of the author's knowledge, they constitute the current state-of-the-art on these research topics, which sustain the objectives of the PhD project that is proposed in Chapter 3.

2.1   Continuous Modes and Mode Transfer

Wireless communication systems have evolved to use wider spectral allocation and allow wider signal bandwidth. These have lead to higher bandwidth requirements in PA design without compromising the efficiency and linearity. Unfortunately, most high efficiency classes of operation, as they were initially proposed, rely on specific harmonic terminations that can only be reliably implemented over a narrow bandwidth. One possibility to overcome this limitation and improve the design process of wideband PAs is to select the best impedance terminations from load-pull measurements over the desired frequency band and for a wide range of output terminations at the fundamental and harmonics.

In [12], Wright *et al.* designed a wideband class-J power amplifier with efficiency higher than 60% over 50% relative bandwidth using load-pull measurements to determine the best load impedance terminations at the fundamental and its harmonics. Later, in [13] the authors were able to extend the relative bandwidth to 60% and introduced a new design tool known as the "clipping contours", which is reported in detail in [14] and later reformulated in [15]. These contours consist on the borderline impedance terminations that define the smith chart region where the corresponding waveforms do not clip, as shown in Fig. 2.1. Therefore, it is possible to achieve high efficiency and output power performance with low nonlinear distortion by choosing the best efficiency load impedance termination in the clip contour.

In [16], Cripps *et al.* have shown that the waveforms of reduced conduction angle modes with an short-circuit at all harmonic frequencies are, in fact, a particular solution of a broader family of waveforms all with the same efficiency performance. The authors demonstrate that there is a continuum of solutions that contains class-J, class-B and class-J*, that can be used to design wideband PAs that gradually move from one class to another over the design bandwidth. The results were then validated through load-pull measurements. The

disadvantage however is that the power utilization factor (PUF) decreases substantially as the operation mode is changed from the class-B into either the class-J or class-J*.
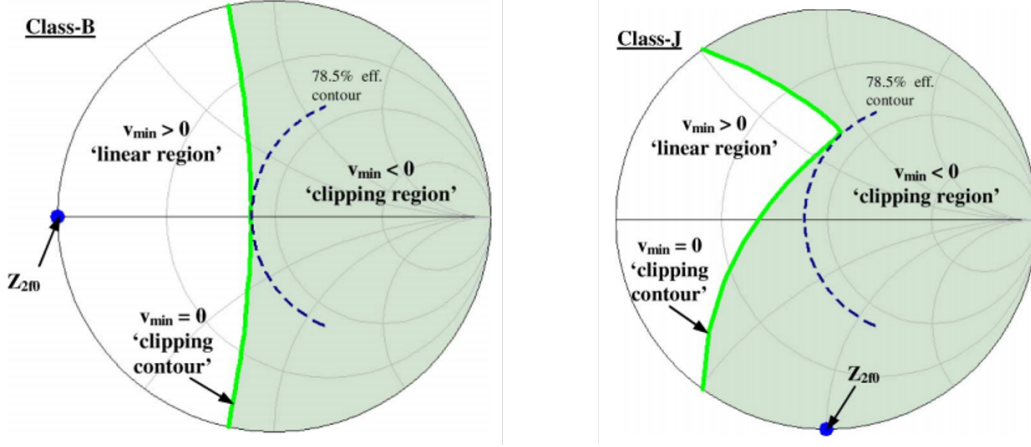
Figure 2.1: Clipping contours for ideal class-B (left) and class-J (right) indicating the optimal load termination for linearity and high efficiency (78.5%), as reported in [13]

In [17], Carruba *et al.* have shown that a similar continuum of waveforms can be defined for class-F, ranging from class-FJ* through class-F and into class-FJ and over which both the efficiency and output power can be kept constant. The continuum is created by simultaneously changing the reactive parts of the fundamental and second harmonic load impedances, while keeping the third harmonic fixed at an open-circuit (also known as class-F$_3$). The advantage over the continuum class-J-J* mode is that the PUF is substantially higher. In a later publication [18], Carruba *et al.* further extend the design space to also include second harmonic terminations that are not purely reactive, greatly improving the design flexibility while still ensuring a high drain efficiency over the entire bandwidth.
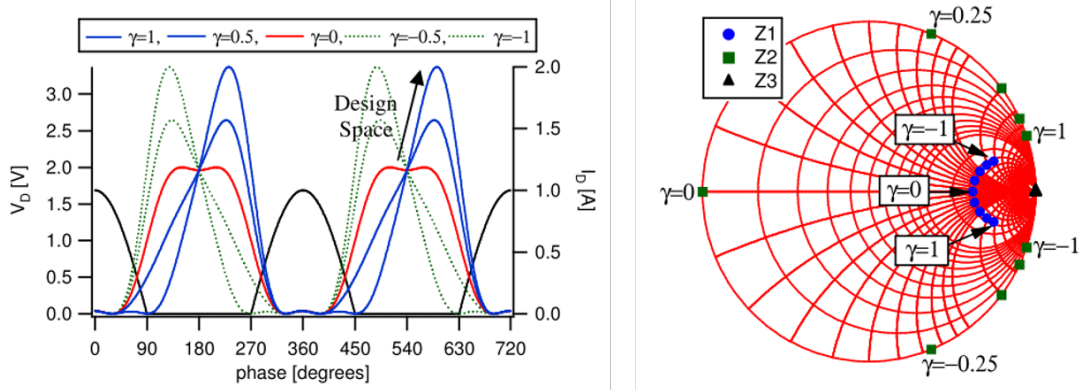
Figure 2.2: Theoretical time domain waveforms (left) and load impedances at the fundamental and second harmonic (right) for the continuous class-F mode, reported in [17].

Similarly, in [19], Friesicke and Jacob demonstrate that a continuum of solutions also exists for class-F^{-1}, by fixing the second harmonic at an open-circuit and changing the reactive part of the fundamental and third harmonic, denominated as class-F$_2^{-1}$, reaching a theoretical 90%

efficiency. The authors also present the comparison between the PUF of these continuous modes. Later, in [20], Carruba *et al.* further extend the design space of the continuous class-F^{-1} to also include second harmonic terminations with real part. Since purely reactive terminations are difficult to realize over a wide bandwidth, this new design space allows additional flexibility in matching network design. However, as the magnitude of the real part of the 2nd harmonic termination increases, the achievable theoretical efficiency decreases, so there is a trade-off between implementation flexibility and efficiency performance that can be explored during the design stage.
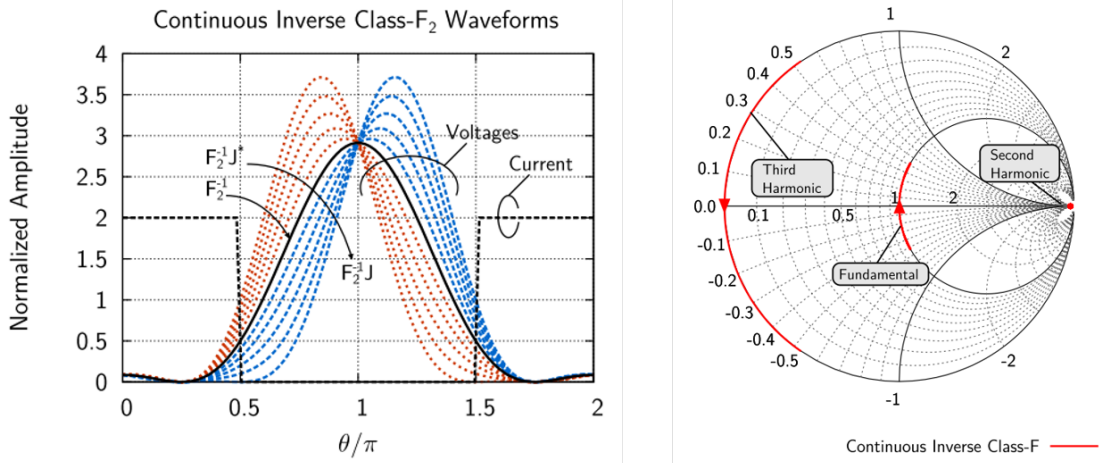
Figure 2.3: Theoretical time domain waveforms (left) and load impedances at the fundamental and second harmonic (right) for the continuous inverse class-F mode, reported in [19].

In [21] and [22], Chen and Peroulis propose and demonstrate for the first time that a PA can operate between class-F and inverse class-F at different frequencies over PAs bandwidth, a technique known as mode transferring. Using this approach, a 50% bandwidth wideband PA was designed with over 60% drain efficiency.

In [23], Ozen *et al.* present novel closed-form solutions that define the continuum operation for class-E PAs, which also includes the class-E/F$_2$, and the class-EF$_2$. The derivation ensures the zero-voltage switching (ZVS) and zero-voltage derivative switching (ZVDS) conditions for a reactive second harmonic load impedance profile selected arbitrarily, granting higher flexibility for wide band designs.

In [24], Chen *et al.* propose a new formulation for continuous operation that further extends the design space of the continuous class-F modes, allowing higher design flexibility due to a wider range of possible fundamental load impedance terminations that lead to nearly the same efficiency performance. In [25] a series of inverse continuous modes formulation is proposed by Shi *et al.*, which is derived from voltage waveform engineering of the inverse class-F continuum.

In [26], Rezaei *et al.* presents a new design space for continuous class-C operation, which includes the fundamental and second harmonic load impedance terminations and allow the design of wide band class-C PAs with constant output power, gain and efficiency.

Finally, in [27], Li *et al.* have reported a new theory for harmonically tuned PA design that achieves maximally flat waveforms and constant output power and efficiency. The optimal fundamental impedance is obtained after independently setting the load impedance at the
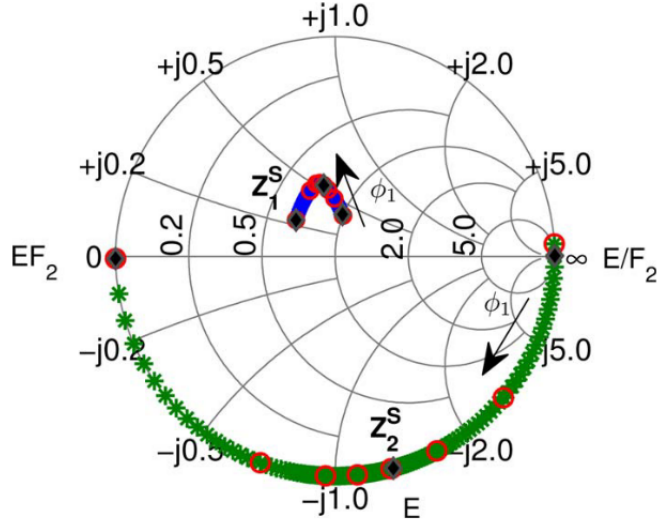
Figure 2.4: Impedance design space for the continuous class-E PA as reported in [23].

second and third harmonics and a wide locus of fundamental load impedances is obtained.

A list of wideband single-ended PA designs, reported in the literature, based on continuous mode design space extensions of the conventional classes of operation is presented on Table 2.1.

Unfortunately, today's communications standards, which are optimized to achieve high spectral efficiency, use signals that have an high PAPR, forcing the PA to operate at a large output power back-off to retain a sufficiently linear characteristic. The PAPR of current wireless signals can range from 3-6dB for Quadrature Phase Shift Keying (QPSK), Quadrature Amplitude Modulation (QAM) or Code Division Multiple Access (CDMA) signals, up to 8-13dB for LTE [40]. Therefore, the average efficiency of all the previously mentioned classes of operation is much lower when excited with real wireless communications signals.

2.2 Wideband Load-Modulated High-Efficiency Amplifiers

Highly efficient and linear amplification of high PAPR signals is an important research topic that has led to the development of several PA design methodologies and advanced high efficiency architectures, such as ET, EER and load modulation based architectures. This work is focused on architectures that use load modulation techniques to improve the average efficiency of the PA, which consist of dynamically changing the load impedance presented to the device, so that it operates with maximum efficiency over a large output power range.

There are several methods to perform the desired load modulation profile. One option is to use variable components in the matching networks that can be dynamically controlled to change the impedance matching, also known as DLM. The other is to use several devices and a non-isolated power combiner, so that the drain voltage of each device becomes dependent on the current injected by the other devices into the combiner, thus changing their perceived load impedance. This is the core mechanism of the Doherty power amplifier (DPA), one of the most used architectures for base station applications due to its high back-off efficiency, simple

Table 2.1: **State-of-the-Art on wideband single-ended PAs based on Continuous modes technology.**

Ref.	Mode	Central Freq. (MHz)	BW (%)	Output Power (dBm)	Drain Eff. (%)
[13]	Class-J	1800	50	40	60-70
[12]	Class-J	2000	60	39	55-65
[18]	Class-F Cont.	737.5	51	40.2	70-80
[18]	Class-F Cont.	825	66.6	40.2	65-80
[28]	Class-F Cont.	1950	51	40.4 - 42.3	70-81
[22]	Class-F/F^{-1}	2300	87	40	60-85
[29]	Class-E Cont.	925	86.5	>39	70-85
[14]	Class-B/J	1950	97.4	>39.3	>60
[24]	SCMPA	2150	51	40.1 - 42.5	70.3 - 81.9
		2200	54.5	39.1 - 42.5	67.5 - 81.9
[30]	Class-F-F^{-1}	690	67	>40	>60
[26]	Class-C Cont.	2000	50	26 - 27	59.4 - 64.4
[31]	Class-F^{-1}	1925	60	41 - 42.3	68 - 82
[32]	Res.-Rea. Class-F/F^{-1}	3075	43.9	>40.8	66 - 71
[25]	Res.-Rea. SCM	1925	117	40 - 43.16	57.4 - 79.1
[25]	SCIMs	3150	47.6	39.6 - 41.4	62.2 - 74.7
[33]	Class-B/J Cont.	3550	39.5	40.9 - 41.9	58 - 78
[34]	Class-F^{-1} Cont.	725	62	38 - 40	73 - 79
[35]	Res.-Res. SCF^{-1}	1350	140.7	39 - 42	62.3 - 80.5
[27]	Class-X	1920	64	37 - 39.9	70 - 86
[36]	Class-J / Class-F Cont.	2400	100	40 - 42.2	60 - 72
[37]	SCM	2000	120	39.6 - 41.3	62 - 68
[38]	Class-F Cont. / Res. Class-F^{-1} Cont.	2500	88	39 - 40.4	56.5 - 75.8
[39]	BJF^{-1}	2500	24	41 - 43	65.9 - 79.7

implementation and early DPD developments. However, other load modulation based PA architectures, such as the Chireix power amplifier (CPA), have also been proposed as viable alternatives as more sophisticated DPD techniques started to emerge. In particular, the former had several advantages in that, being an RF-input PA of simpler driving and design methodology, it could directly replace traditional class-B and class-AB PA in base station without major changes in the transmitter topology. Although conceptually simple and of low design complexity, practical implementations of DPAs and CPAs exhibit highly nonlinear behaviour and bandwidth limitations due to several device and implementation imperfections that are not accounted for in the ideal therory. In fact, as DPD techniques have become advanced enough to allow DPAs to meet the stringent linearity requirements of communication standards [41–43], the DPA quickly became the workhorse of wireless communications even up to this day.

Research has also been focusing multiple-input single-output (MISO) PA architectures, not only to improve the performance and design flexibility of Doherty and Chireix PAs through

mixed-mode excitation, but also to allow a hybrid operation between the two, where the specific driving conditions lead the load to be modulated as in a DPA or as a CPA at different power levels.

Another recent and promising PA architecture is the load modulated balanced amplifier (LMBA), that uses a quadrature coupler as the output combiner and an additional PA to inject power at the isolated port of the coupler. By controlling the amplitude and phase of the power injected into the isolated port, the impedance presented to the devices at the input ports can be changed dynamically to achieve Doherty-like efficiency profiles over a wide radiofrequency (RF) bandwidth.

In this section, the operation principles, capabilities and limitations of each of the previously mentioned architectures will be discussed.

2.2.1 Doherty Power Amplifier

The Doherty PA is one of the first solutions to increase the average efficiency of power amplifiers under amplitude modulated stimulus. The architecture was proposed by W. H. Doherty in 1936 [44] to stimulate the increase of transmitted power without increasing the required cooling systems and operational costs of broadcast stations.

The structure of the Doherty PA is shown in Fig.2.5. It is composed of two devices and a non isolated impedance inverting combiner network. The core idea is to use the additional device, the "peaking", to induce the optimal load modulation on the "main" device to maximize the fundamental voltage even when the device is supplying lower current. This minimizes the consumed DC current for a wider range of output power and, therefore, maximizes its efficiency. The fundamental voltage and current components of each device is presented in Fig.2.6(a) and Fig.2.6(b) respectively.
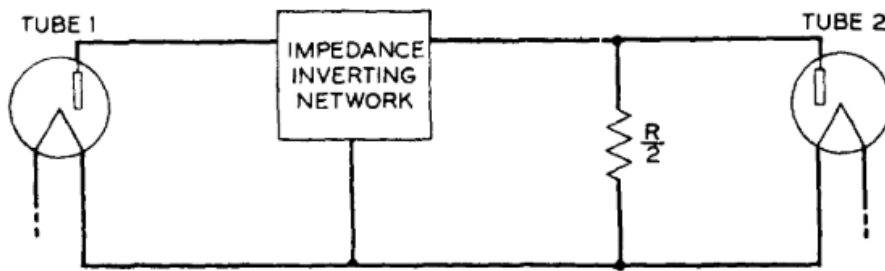
Figure 2.5: Simplified circuit schematic of a Doherty PA, as reported originally in [44].

The simple structure, design and implementation of the DPA and the ability to directly replace the traditional class-AB PAs without major changes in the transmitter's architecture made it, even to this day, one of the most well established methods to boost the efficiency of wireless transmitters. In addition, DPD techniques could also be more easily applied to DPAs than to more complex alternative architectures, such as envelope tracking and outphasing, in order to meet the stringent requirements of wireless communications standards.
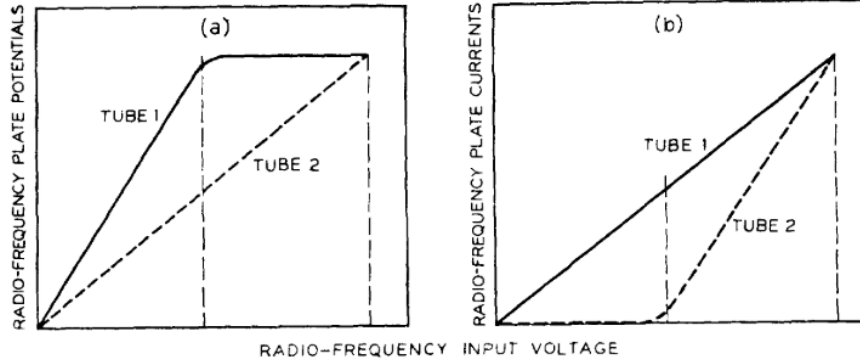
Figure 2.6: Fundamental a) voltage component and b) current component of each device that composes the Doherty PA, as reported originally in [44].

Bandwidth Limits

There are several aspects of the traditional ideal Doherty PA that are difficult to implement over wide bandwidth. Therefore, an extensive research effort has been made to develop new design techniques that improve the bandwidth and performance of the DPA in wideband multi-band and multi-standard scenarios.

The impedance inverting network implemented using a quarter-wavelength transmission line (QWTL) is inherently narrowband and limits the fractional bandwidth [45]. Several publications report alternative combiner designs to achieve wider bandwidth.

In [46], Sarkeshi *et al.* present an adaptive frequency dependant quarter-wavelength transformer by using varactors.

In [47], Wu and Boumaiza use a Klopfenstein taper in place of the traditional quarter-wavelength transmission line. A similar approach is used in [48] where the tapper is included into the matching network of the Main amplifier.

In [49], Bathich *et al.* have used multi-section matching networks to preserve the bandwidth performance. In [45] the same author presented a comprehensive analysis on the bandwidth limits of traditional Doherty PAs due to the frequency response of the QWTL that is used as the output combiner. As the frequency deviates from the design value, the real part of the impedance presented to the main PA becomes progressively lower, reducing the fundamental voltage component and the efficiency at back-off power. The authors demonstrate that reducing the transformation ratio of the QWTL improves the back-off efficiency over a wider bandwidth.

Appropriately designed offset lines at the output of the Main and Peaking PAs can also be used to extend the bandwidth of the DPA, as reported in [50] and [51].

In [52], [53] and [54], an architecture based on single-section and dual-section couplers has been proposed, where the latter solution was able to reach 36.3% of fractional bandwidth. In [55] the authors have also developed a new closed-form design technique for the input and output splitting and combining networks to obtain very wideband performance on the order of 83% fractional bandwidth.

In [56], Fang and Chen propose a new configuration and theoretical analysis to improve both the bandwidth and PUF of wideband DPAs, focused on the optimal design of the Peaking

PA's impedance transformer.

The post-matching techniques have been proposed with several variants in [57], [58], [59], [60], [61], [62], [63]. The core idea is to perform the impedance matching of the devices after the combiner network, to separate it from the load modulation performed by the combiner.

Another important aspect is that the Peaking device presents a large input impedance variation with the input power and lower transconductance due to the deep class-C bias conditions, leading to an inconsistent power division ratio at the input. This issue is analysed in [64], in which Kang *et al.* propose a novel direct input power divider by taking into account both the input impedance variation and the output matching networks, and also using a DPD technique.

The nonlinear output capacitance of the device also damages the ideal load modulation and needs to be taken into account when designing the wideband output matching networks and combiner. In [65], Qureshi *et al.* incorporated the output capacitance of the device into the combiner design to achieve higher bandwidth. Sun and Jansen [66] make use of the real frequency technique to design the combiner and matching networks based on the desired S-Parameters. In [67], a new technique is used to design and preserve the broadband performance of the combiner for devices with large output capacitance.

Digital Doherty

The Digital Doherty consists of driving the main and peaking amplifiers of the conventional Doherty PA independently by using a digital signal processing (DSP) unit to generate the required amplitude ratio and phase difference between the two channels. Contrary to using a conventional analog power divider, this method allows creation of different phase difference profiles at distinct power levels to provide an additional degree of freedom to adjust the load modulation.

Because of this, digitally driven Doherty PAs have increased design flexibility, since the impairments of the main and peaking PAs can now be corrected using improved amplitude and phase driving profiles, leading to mixed-mode digitally driven MISO PAs, in which the amplifier is no longer excited with either a pure phase modulation as in CPAs or pure amplitude modulation as in DPAs, but with a combination of both at each power level.

The first digitally driven DPA has been proposed by Darraji *et al.* [51], where he demonstrates that the PAs bandwidth and back-off efficiency can be significantly improved by changing the input power division ratio between the peaking and main PAs at different frequencies. In a later publication [68], Darraji and Ghannouchi use an alternative power ratios to minimize the power dissipation in the peaking PA at back-off, resulting in improved efficiency. More recently in [69], Piacibello *et al.* have performed a thorough analysis of the performance enhancement that can be obtained with a power dependent splitting ratio and phase alignment in a dual-input Doherty PA over its equivalent single-input implementation.

2.2.2 Outphasing/Chireix Power Amplifier

The Chireix-outphasing PA was proposed in 1935 by H. Chireix [70]. A pure outphasing amplifier is composed of two identical high efficiency amplifiers, such as switching mode or operating in saturation, and an input splitting network, usually a DSP unit, that splits the amplitude and phase-modulated excitation signal into two separate signals of constant amplitude and with a phase relationship that depends on the amplitude of the excitation.

Both PAs are assumed to operate independently of one another and always at their maximum output power. Then, their output power is combined with the phase difference that is imposed by the DSP, to reproduce the amplitude and phase-modulation of the excitation signal at the load.

This simple operation mechanism hides an important drawback in terms of energy efficiency. When the input excitation amplitude is very low, the DSP will generate two signals that are in near opposite phase, so that the resulting output power is also low. However, since both PAs operate at their maximum output power capability, the excess power must be dissipated on the combiner, drastically reducing the overall system efficiency if this energy is not reused for some other useful application.

If the combiner is passive and non-dissipative, both PAs will perceive an amplitude dependent varying impedance that becomes highly reactive due to the reflected power ate the combiner. In order to improve the efficiency of the pure outphasing PA, H. Chireix proposes a compensation network at the output of each PA, that can be designed to resonate with the reactive component of the load at a given amplitude level, at which the load becomes purely resistive. In this way, the designer can choose a power level that matches the average power statistics of the excitation signal and design the appropriate compensation network to obtain high efficiency performance for that application. This is what is usually called the CPA.
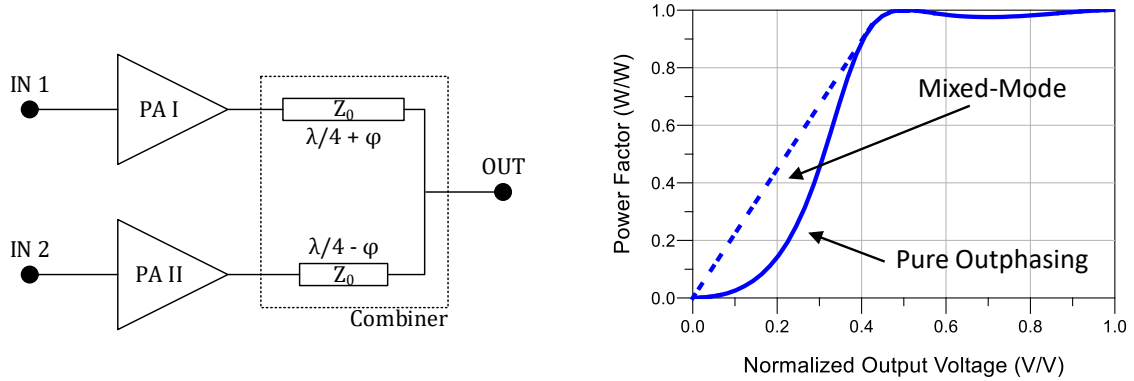
Figure 2.7: Circuit schematic of a transmission line Chireix PA implementation (left) and the theoretical efficiency performance for the pure outphasing and mixed-mode excitation modes (right), as reported in [71].

This compensation network can be implemented in several ways. The original proposal was to use a lumped inductor in one amplifier and a lumped capacitor at the other. However, at higher frequencies, it becomes more practical to use two transmission lines of different widths to implement the required phase difference. In practice however, this networks can be designed together with the necessary impedance matching of each device to promote a compact implementation, minimize losses and improve the bandwidth.

Conventional Chireix PA implementations are usually dual-input with DSP to provide the required phase relationship between channels. Only recently have RF-input CPAs been reported in the literature by Barton *et al.* [72, 73], where a new analog input signal decomposition network is proposed to synthesize the required excitation signals without expensive baseband processing hardware.

The bandwidth of Chireix PAs has also been a research focus. Piacibello *et al.* [74] have shown that both the transmission line output combiner and the intrinsic elements of packaged

devices are the most limiting factors in wideband implementations. For this reason, accurate transistor models, and the respective deembedding models, are becoming an invaluable tool in PA design [75, 76].

However, the efficiency profile of the CPA is still very low at low amplitude excitation, as can be seen from in Fig. 2.7. Actually it is even worse that a typical single-ended PA at the same operation region. Because of this, practical implementations of the CPA do not perform the usual outphasing input splitting at this levels, but, instead, simply drive the amplifiers with a linear amplitude profile and a constant phase difference that forces the power of each PA to sum in-phase at the output, effectively operating as two single-ended PAs in parallel.

Qureshi *et al.* [77] reported for the first time a mixed-mode CPA, where driving conditions impose class-B operation in the low power region to improve the efficiency below the back-off. Calvillo-Cortes and Vreede [78] have performed a thorough comparison between pure-mode and mixed-mode CPAs and provided analytical expressions for the input drive profiles. Nunes *et al.* [71] recently reported an analytical derivation of the driving required to impose current-mode operation in a CPA, leading to improved linearity for the same efficiency profile.

Recent research has also been able to derive a modified combiner and input splitting profile that allow a mixed operation between class-B, Chireix/outphasing and Doherty load modulations at distinct output power levels, denominated as Doherty-Outphasing power amplifier (DOPA). In [79], Qureshi proposed a new dual-input PA architecture that allows the transition from a Chireix to a Doherty load modulation as the input power increases, greatly improving the efficiency over -12dB output power back-off (OPBO).

The same concept can be used to drastically improve the bandwidth of load modulated amplifiers by developing an output combiner that imposes Doherty and Chireix operation at different frequencies, denominated as Doherty-Outphasing Continuum PAs. Despite their advantages, the design procedure of MISO PAs relies to a great extent on Monte Carlo simulations to determine the best load modulation profiles and the respective excitation signals. Such simulations can be extremely time consuming and do not guarantee that an optimal solution is found. Therefore, new design methodologies are currently needed so that MISO architectures can reach their full potential.

2.2.3 Doherty-Outphasing Continuum

The Doherty-Outphasing Continuum is a double-input single-output (DISO) PA proposed by Andersson and Gustafsson [80, 81] that is capable of achieving high efficiency at OPBO with over 100% relative bandwidth.
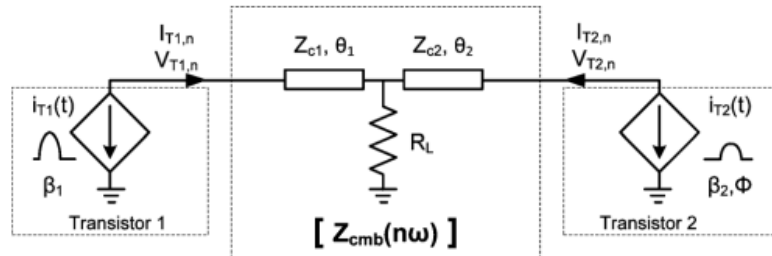
Figure 2.8: Output combiner topology for Doherty-Outphasing Continuum operation, as reported in [82].

The simplified diagram of the PA is presented in Fig.2.8. The PA is composed of two transmitter branches and an non-isolated transmission line output combiner, that is fully characterized by the electric lengths at the central frequency θ_1, θ_2, and the characteristic impedances Z_{c1} and Z_{c2}.

For each value of the combiner's parameters, there is a combination of input driving profiles that induce an optimal load modulation on each device that maximizes the efficiency of the PA. For instance, that for $\theta_1 = 90$ and $\theta_2 = 0$ the combiner is essentially a QWTL and, as expected, the optimal load modulation corresponds to that of a DPA. If $\theta_1 = 60$ and $\theta_2 = 120$ it is shown that the optimal driving profiles lead to mixed-mode operation between class-B and Outphasing/Chireix. In fact, the resulting combiner can be expressed in the form $\theta_1 = 90 - \delta$ and $\theta_2 = 90 + \delta$ with $\delta = 30$, which is a commonly used combiner in compensated CPA design. These two solutions are reported in the work of Gustafsson in [82] and replicated in Fig.2.9 for reference. Since the frequency response of the combiner can be thought of as a change of the electrical lengths of each transmission line, distinct load modulation profiles with high average efficiency can be mapped to different frequencies, drastically improving the design space of the combiner.

(a)

(b)
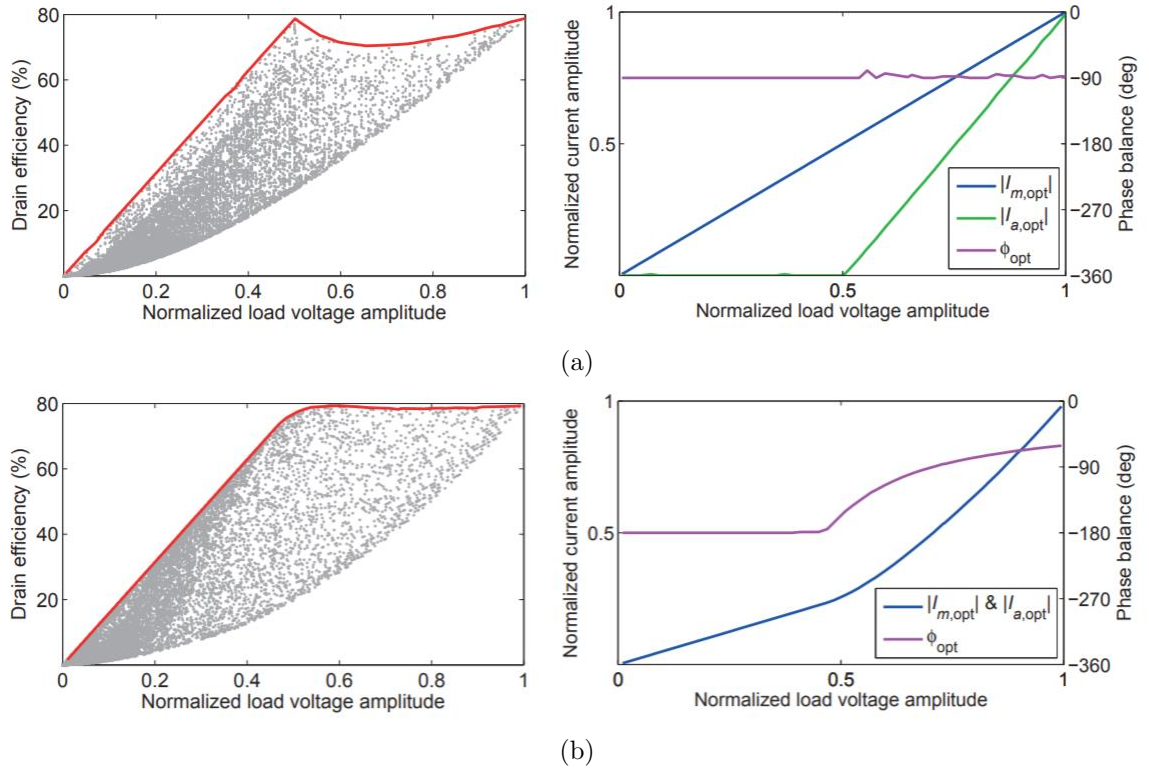
Figure 2.9: Efficiency and input excitation profiles for a) $\theta_1 = 90$ and $\theta_2 = 0$, corresponding to a Doherty load modulation b) $\theta_1 = 60$ and $\theta_2 = 120$, corresponding to an Outphasing load modulation, reported in [82].

The Doherty-Outphasing Continuum technique allows the bandwidth extension of Doherty/Chireix PAs without the degradation of their back-off efficiency performance. However, there are several design challenges that still need to be addressed.

- **Output Combiner Design** The structure presented in [80] allows a theoretical back-off efficiency higher than 60% in over 100% relative bandwidth. However, it is not known if this is the optimum combiner topology, both in terms of bandwidth and achievable back-off efficiency.

- **Input Driving Profiles** Currently, the simplest way of obtaining the optimum input driving profiles for a given combiner topology is through brute-force Monte Carlo simulations. Therefore, reaching an optimal solution in this way can be extremely time consuming, depending on the combiner's complexity.

- **Wideband and Concurrent-band operation** The reported design methodology (i.e. the input excitation and efficiency profiles) is based entirely on the continuous wave (CW) operation of the combiner at each frequency. However, under wideband and multi-band excitation, the optimal excitation profiles can be significantly different from the CW scenario. For instance, in dual-band operation with wide band separation, the CW driving profiles can be very different at the central frequencies of each band and it is not clear how the look-up tables (LUTs) for multi-band operation can be obtained from the respective CW ones of each band.

2.3 Power Amplifier Performance under Wideband Excitation

Although able to achieve high efficiency under CW excitation, it is known that any of these configurations are strongly nonlinear and suffer performance degradation when excited with wideband or concurrent-band signals [83]. In fact, prior to the start of this PhD research project and even in the context of single-ended PAs, the actual mechanisms that lead to this degradation were still not fully explained.

Several studies have shown that the baseband impedance terminations are an important cause of performance degradation and proposed methods to correct it. In [84], Carvalho and Pedro provide a comprehensive explanation to the intermodulation distortion (IMD) asymmetries often observed in two-tone and multi-tone tests and relate the phenomenon to the impedance at baseband frequencies. In [85], Bunz *et al.* have reported a linearity and efficiency degradation from both the input and output baseband terminations through experimental envelope source and load-pull measurements. In [86], Cabral *et al.* have analyzed the impact of the baseband impedance nature on the the dynamic behaviour of the PA's amplitude modulation to amplitude modulation (AMAM) performance. In [87], Akmal *et al.* have demonstrated the impact of baseband impedance on the PA's performance using an improved method for active intermediate-frequency load pull measurements. In [88], Chen *et al.* have demonstrated through load pull that proper impedance terminations at the intermodulation components are able to improve the linearity and efficiency of PAs operated under concurrent-band scenarios. In subsequent publications [89,90], the same authors report the design of optimized concurrent-band Class-AB and Doherty PAs, using inter-modulation tuned networks.

Other out-of-band frequency terminations have been shown to produce not only a linearity improvement [91, 92], but also an average efficiency variation in [93] under 2-tone excitation using active load pull measurement systems, where the reported efficiency variation can be as high as 10%. In this PhD work, a similar study was performed through simulation in [94]. For passive load terminations, this variation is not as strong when compared with the

degradation generated from the baseband terminations; and considering the conventional matching network design, it would require very high quality factor resonant circuits precisely at IMD3 components to generate high degradation. For this reason, the focus of this work was set on the baseband self-biasing mechanisms.

This PhD research project has provided contributions in the analysis and extension of the instantaneous bandwidth and wideband operation performance [95], [94]. In [94], a comprehensive analysis of the efficiency degradation in wideband PAs due to the output baseband impedance terminations is presented. An analysis of the PA's dynamics has been performed and an approximate model of the underlying degradation mechanism has been derived. It has been demonstrated that improper baseband impedance terminations can induce a high drain voltage modulation at the intrinsic drain of the device, changing the original operation that one would expect from the CW performance, as shown in Fig. 2.10 for several baseband impedance profiles over frequency.

(a)   (b)

Figure 2.10: Output baseband impedance profiles of a single-ended PA (top) and average efficiency performance for a two-tone signal of different tone separations (bottom), reported in [94].

Finally, in [96] we demonstrate that the input baseband impedance is also a source of degradation in concurrent dual-band operation, even with ideal output baseband impedance terminations. A qualitative description of the phenomena and insight on how to design the input bias circuitry to prevent the efficiency and linearity degradation are presented, as shown

in Fig. 2.11. This work was extended further in [97] to include a detailed analysis of the bias impedance nature impact on the gate bias voltage self-modulation and the corresponding output power, consumed power and efficiency variation. The work also demonstrates that the proposed model, derived considering two-tone excitation, also provides efficiency profile predictions consistent with the measured concurrent dual-band operation with realistic Orthogonal Frequency-division Multiplexing (OFDM) modulated signals.

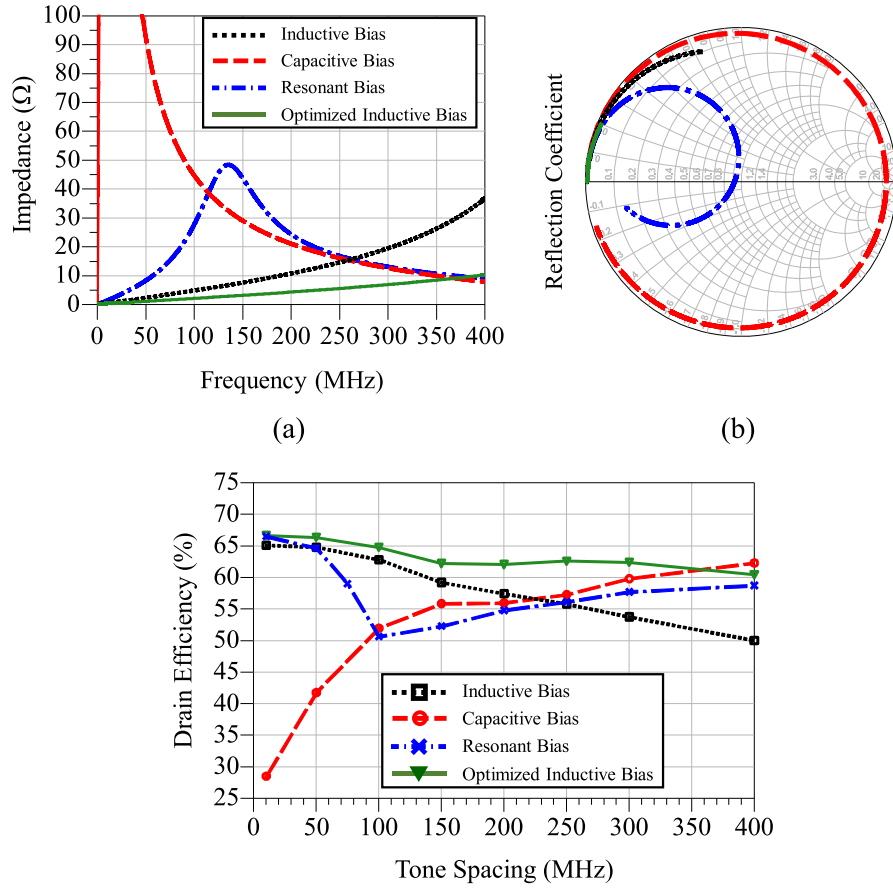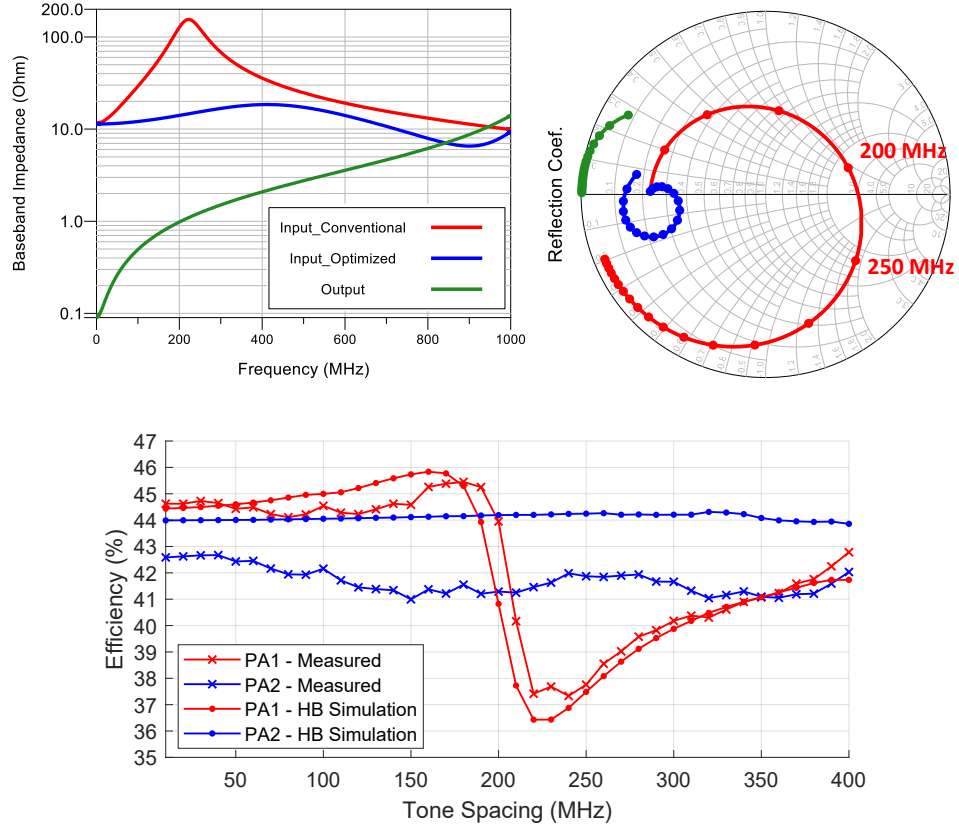Figure 2.11: Input baseband impedance profiles of single-ended PA (top) and the respective average efficiency performance for a two-tone signal of different tone separations (bottom), reported in [96].

Chapter 3

Goals and Innovative Contributions

Given the technical challenges and research achievements expressed in the state-of-art, the main research direction chosen for this PhD work is the study of video-bandwidth mechanisms and their induced performance degradation in high-efficiency PAs. In the past, when the PA operated mainly for single-band and narrow-band scenarios, these mechanisms were still manageable from a PA design perspective. However, the bandwidth of wireless communication signals has been continuously increasing due to carrier aggregation and multi-band operation, instigated mainly by higher data rate demand. As a result, both PA design complexity and overall design duration rised dramatically, and it is increasingly difficult to fully prevent performance degradation induced by the video-bandwidth mechanisms. Hence, it is necessary to deepen the knowledge on this particular problem to enable future wideband and high-efficiency transmitters.

Although research has clearly reported the performance degradation due to the limited video-bandwidth, the underlying mechanisms had not yet been clearly described and modelled. Detailed knowledge and accurate models of these mechanisms are essential to develop proper design or compensation methods that mitigate their impact on the PA's performance. As such, this research topic can be further divided into several sub-objectives.

- **Provide a qualitative description of the device's inner mechanisms that originate the limited video-bandwidth**
  This knowledge allows PA designers to have a full understanding about the non-linear mechanisms and the design parameters and constraints that link the video-bandwidth to the PA's performance under modulated signal excitation.

- **Identify modeling strategies that capture the performance degradation**
  These models are rooted in an theoretical analysis of the non-linear mechanisms and provide a good balance between accuracy and complexity. In this way, PA designers can obtain an accurate prediction of the overall performance and recognize their qualitative understanding of the mechanisms in the model formulation.

- **Propose PA design strategies that mitigate these mechanisms and optimize PA performance**
  The obtained knowledge about the video-bandwidth degradation mechanisms should then be used to improve design techniques and applied to practical PA design to obtain optimized instantaneous bandwidth performance.

Chapter 4

Research Work - Video-Bandwidth Degradation Mechanisms

The study of video bandwidth (VBW) related performance degradation is a necessity in modern RF transmitters as multi-band and carrier aggregation techniques are pushing the boundaries of wideband PA design. However, an accurate evaluation of the VBW requires wideband modulated signal excitation, which adds higher complexity and time consuming simulations to the design process. Although many researchers had clearly identified the connections between the load impedance at envelope frequencies and PA performance, as previously shown throughout the state-of-art, the underlying mechanisms that govern that interaction were still not fully described and modelled up until the work presented in this thesis.

The PA's video-bandwidth, is the maximum bandwidth of the modulated signal that can be fed into a PA without significant performance degradation, with respect to the predicted from CW performance. Typical performance degradation includes strong IMD asymmetry, lower output power at saturation and reduced average efficiency, and is widely attributed to the drain bias voltage modulation at the envelope frequency and its harmonics when its bandwidth is sufficiently wide. Usually, the output power and efficiency requirements are the limiting factor as they cannot be compensated without redesigning the PA, while the adjacent channel power ratio (ACPR) can be corrected to some extent through DPD. However, ACPR degradation due to IMD asymmetry requires higher complexity DPD techniques and, in some cases, can even entirely prevent it from linearizing the performance to the required targets.

Several techniques can be used to estimate or quantify a PA's video-bandwidth. The direct method is to excite the PA with modulated signals of progressively higher bandwidth and keep track of the output power, average efficiency and ACPR until any of them degrades beyond the specifications for the target application. The simplest way to do this is to use a two-tone signal of increasing tone separation, as not only it is very simple to generate it in any vector signal generator, but also its simple envelope waveform simplifies the expected performance estimation if the CW performance is known. The video-bandwidth can also be indirectly estimated through S-parameter measurements of the output network, from a few MHz up to the center frequency of the RF carrier. High quality factor resonances in the impedance profile, as shown in Fig.4.1 create very large drain voltage fluctuations at those particular frequencies if excited by the RF signal's envelope, leading to extreme performance degradation. These two techniques have been extensively used in this work, both in simulation

and in physical PAs, to aid the development of a theoretical model capable of describing the performance degradation.
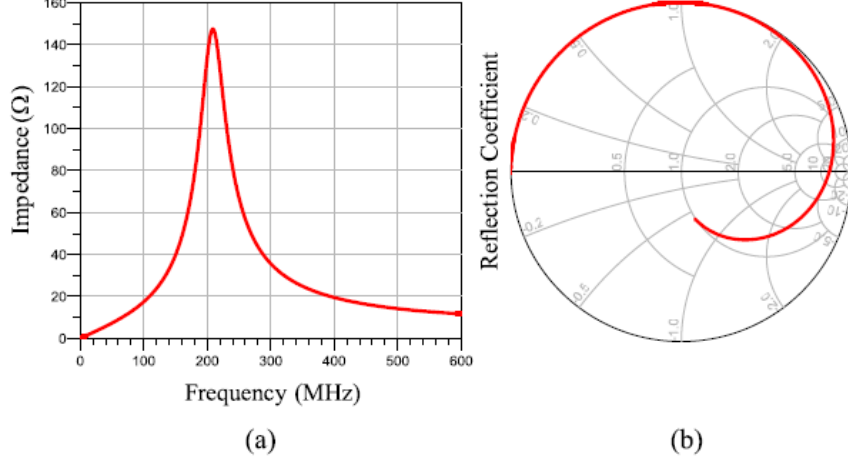
Figure 4.1: Illustration of (a) impedance profile and the respective (b) reflection coefficient presented to the i_{DS} current source in a presence of a resonance at baseband, reported in [94].

4.1 Drain Bias Voltage Self-Modulation

Taking the existing literature on the video-bandwidth induced drain bias voltage modulation as a starting point, the fundamental mechanism was qualitatively explained through nonlinear simulations and the corresponding results were published in the paper transcribed as Annex A.

This work starts by defining the simplified circuit representation of an RFPA presented in Fig.4.2, reproduced here to aid the exposition of the achievements and contributions. The PA is composed by three main blocks: the output matching network (OMN) to provide the required power and efficiency impedance matching at the output; the input matching network (IMN) to impose the matching for gain and stable operation; and, finally, the device itself, composed by the nonlinear internal capacitances and current source.
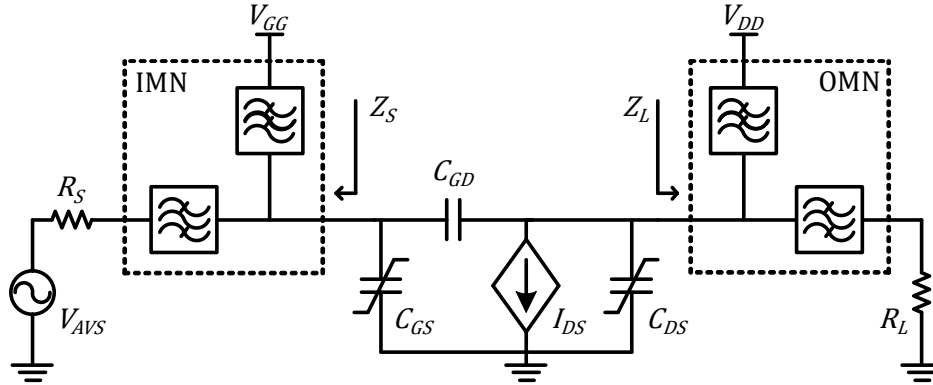
Figure 4.2: Simplified circuit representation of an RFPA.

Each block has the following characteristics:

- **The RF transistor**
  The device model consists of the nonlinear current source and the intrinsic capacitances C_{gs}, C_{ds} and C_{gd}. In a real device, all these three capacitances are nonlinear in nature with respect to the gate-source and drain-source voltages. However, it will be made clear that the nonlinear elements that dominate the video bandwidth performance are the current source in the case of the drain bias voltage modulation, and C_{gs} in the case of the gate bias voltage modulation. So, in the scope of this work, both C_{ds} and C_{gd} are always linear, and C_{gd} is only nonlinear for the gate bias baseband modulation study, which, in turn, provides a simpler model for the degradation mechanisms involved.

- **Input and Output Matching Networks**
  The matching network blocks comprise the RF impedance matching and bias circuitry required to bias the device, provide stable operation conditions and obtain a flat CW performance over the entire RF bandwidth. This last condition is important to ensure there are not additional effects from CW performance variation, which can also create performance variation under modulated excitation. The bias impedance profile is assumed to be decoupled from the RF matching, i.e., several profiles will be considered without changing the RF terminations and the CW performance.

This work focuses a specific output baseband impedance profile that results from traditional bias network design, which makes use of either a large value inductor or a high impedance quarter wavelength transmission line to minimize insertion loss and loading effect on the RF matching at fundamental frequencies. Since the RF matching must include a RF DC block capacitor, the overall nature of the impedance profile is inductive at low frequency, imposed mainly by the bias network.

4.1.1 Mechanism Description

The baseband drain voltage can expressed as

$$v_{d0}(\tau) = V_{DD} - L\frac{di_{d0}(\tau)}{d\tau} \tag{4.1}$$

which simply states that the baseband drain voltage fluctuation, $v_{d0}(\tau)$ around the DC bias point V_{DD} is proportional to the value of the bias inductor, L and to the derivative of the baseband drain current, i_{d0}, i.e. the signal's bandwidth. Equation (4.1) is then used to qualitatively explain the baseband waveforms obtained through nonlinear 2-tone simulations for a simple piece-wise device model, and the implications to the PA performance in terms of efficiency and output power.

In order to maximize the efficiency, single-ended high-efficiency PAs are designed with an RF load that exploits the full drain voltage range available set by V_{DD} and the knee voltage, V_K, forcing the PA to operate as close as possible to the triode region at their peak power capability. Since equation (4.1) includes a first order derivative of the drain current, the baseband drain voltage is shifted towards lower or higher values if the envelope increases or decreases in amplitude, respectively. Therefore, for a fixed RF load, the PA will sometimes operate deeper into the triode region when the available voltage range decreases, i.e. when $v_{d0}(\tau) < V_{DD}$, and deeper into in the saturation region when $v_{d0}(\tau) > V_{DD}$.

These two cases are not symmetric since the PA exhibits strongly nonlinear behaviour when driven towards the triode region, as it saturates due to voltage limitation. In particular, since the DC drain current capability decreases, both the fundamental and baseband currents are lower but, for moderate saturation, their ratio can still be approximated by $2/\pi$. However, the output power is further reduced due to the available fundamental voltage limitation imposed by v_{d0}, while the DC voltage for consumed power calculation remains constant and equal to V_{DD}, imposed by the DC voltage source. Therefore, the efficiency is degraded.

On the other hand, when $v_{d0}(\tau) > V_{DD}$, the PA operates at the saturation region with unrestricted fundamental voltage and current. Since the transconductance is constant, the drain current and voltage waveforms are the same, resulting in the same efficiency and output power performance. The dynamic loadline at the intrinsic drain node and the baseband voltage waveforms are presented in Fig.4.3 for an inductive baseband impedance. The respective evolution of the PA's figures of merit within a period of the envelope waveform is presented in Fig.4.4. As observed, the efficiency is always degraded in some parts of the envelope but never improved on the complementary time frames.
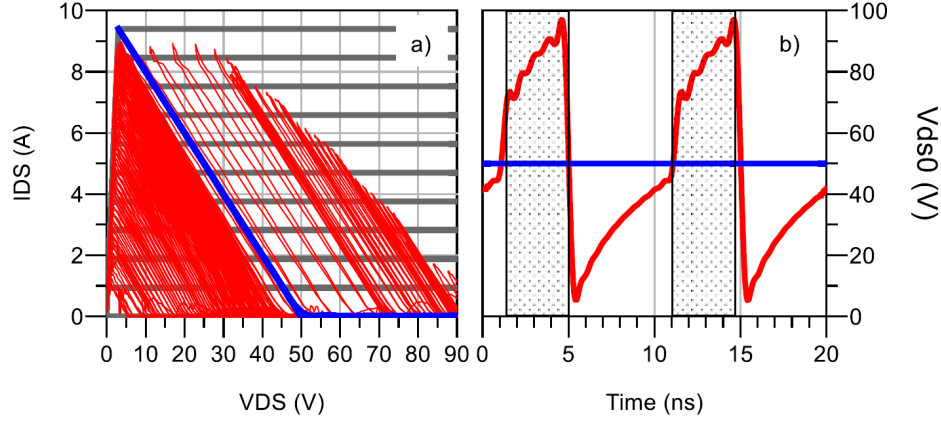
Figure 4.3: (a) Load trajectories and (b) baseband voltage component of the conceptual power amplifier.
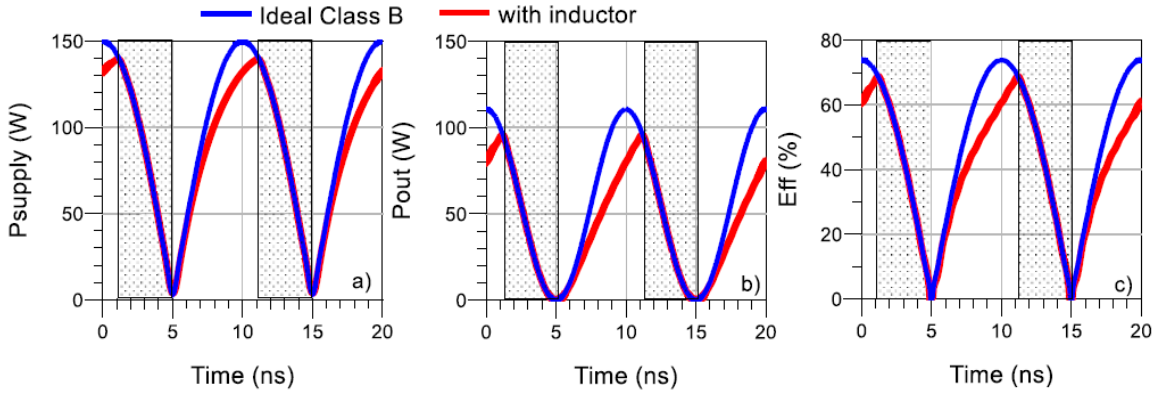
Figure 4.4: Instantaneous waveforms of the PA's (a) absorbed dc power, (b) output power and (c) efficiency for an inductive baseband impedance scenario.

24

Therefore, it is concluded that the average performance is degraded due to the limited voltage operation during time intervals where the derivative of the envelope waveform is positive. This qualitative description of the mechanism constitutes the main innovative contribution to the state-of-the-art by this publication. Although the mechanism is illustrated using 2-Tone simulations, this qualitative behaviour is valid for any envelope waveform since (4.1) is general, as long as the baseband impedance is purely inductive.

4.1.2 Modelling and Validation

The analysis was further expanded in Annex B, including several baseband impedance profiles that can be realistically obtained in practical wideband PA implementations as well as the respective mathematical formulation that describes the mechanism for each profile. The validity of the derived models, and that the baseband drain impedance is the dominant cause of performance degradation, are demonstrated in two distinct wideband PA prototypes presented in Fig. 4.5. One was designed using a conventional quarter wavelength transmission bias line, allowing the RF matching network and the bias circuit to be designed almost independently. The other uses a shorter and wider bias transmission line and is included into the RF matching network design.
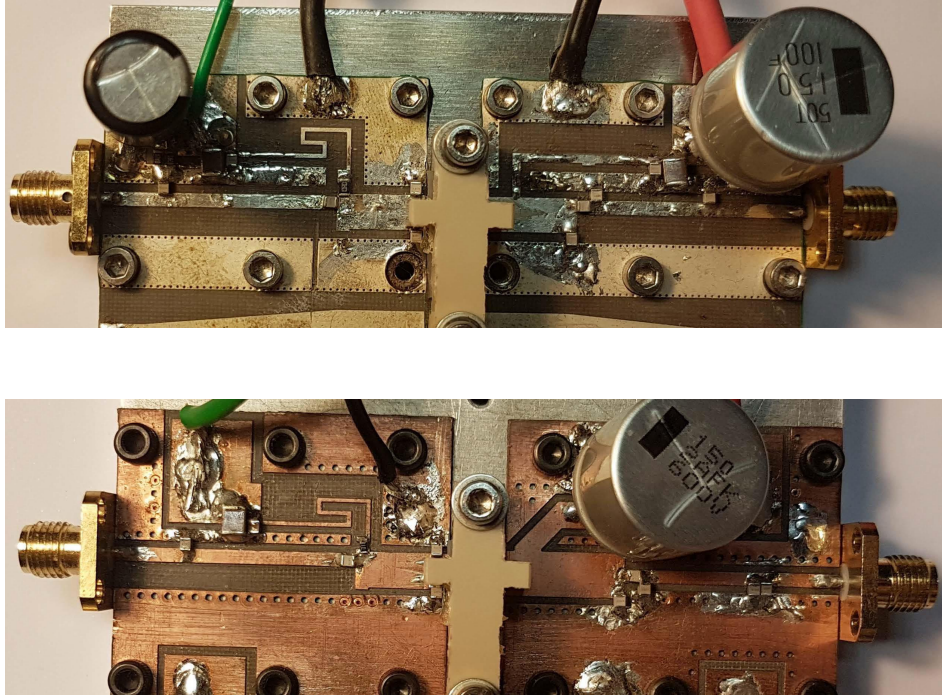
Figure 4.5: Photographs of the implemented PA prototypes, conventional bias network (top) and optimized bias network (bottom).

Both PAs achieve similar CW performance, to the best of our manufacturing capability, but present very distinct baseband impedance profiles. The bias line in the conventional design presents a higher impedance than the second approach, causing a parallel resonance to appear closer to the PA's videobandwidth. By using a shorter bias line in the second prototype, the bias circuit presents a lower inductive impedance at videobandwidth frequen-

cies, which shifts this parallel resonance to higher frequency, decreasing the baseband drain impedance drastically. The magnitude of baseband and the fundamental impedance profiles are reproduced here in Fig. 4.6.

The two-tone average efficiency was measured at several tone separations within 400MHz as shown in Fig. 4.6. The lower baseband impedance in the second prototype almost completely eliminates the efficiency degradation observed in the conventional design, demonstrating that this mechanism is the dominant cause of performance degradation in wideband PAs. Additionally, by using the proposed model formulation fit to the GaN device and the designed matching networks, we obtained a good prediction of the measured efficiency profile in both PAs.
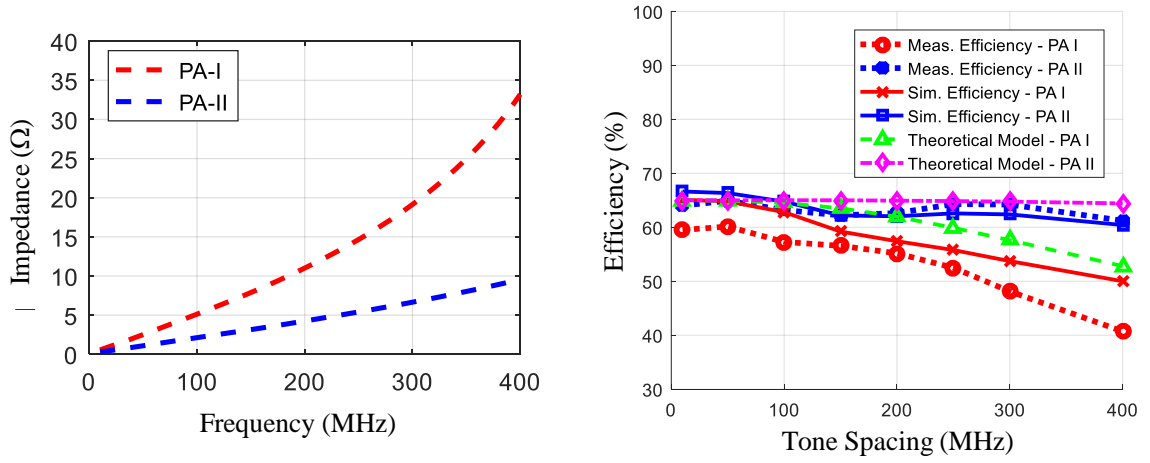
Figure 4.6: Magnitude of the baseband impedance for each implemented PA (left) and average efficiency measurements for 2-tone excitation for several tone spacing values (right).

4.2 Gate Bias Voltage Self-Modulation

While working on this topic, it was observed that the efficiency and output power variation with the bandwidth of the input signal, although small, was not fully eliminated even with an optimized bias impedance. So we speculated that it would also be possible to have a dynamic gate voltage fluctuation at baseband, also referred to as input self-biasing. However, the mechanisms at play are completely different in nature, since the only nonlinear elements in the device that can generate baseband gate current distortion components are the transistor's internal capacitances, C_{gs} and C_{gd}, and the gate-source junction diode.

4.2.1 Mechanism Description and Modelling Approach

This mechanism was studied and demonstrated to occur in practical PA implementations in the International Microwave Symposium (IMS) 2019 publication in Annex C. The main objectives of this work were to provide a qualitative explanation of this mechanism and present a simple model that predicts the two-tone average efficiency, as well as its dependency with the circuit and design parameters. It also demonstrates that the input baseband impedance

is an important design constraint in wideband PAs that is commonly ignored at the design stage.

The work focuses on the C_{gs} capacitance as the main nonlinear distortion generator at the gate of the device since it is present at all input power levels, while the input gate-source diode only enters conduction when the PA is driven deep into compression, which is usually kept low due to linearity and DPD complexity constraints. Additionally, C_{gd} is considered linear and embedded into the matching networks through miller effect. Additionally, it is also imposed that the baseband impedance at the drain terminal is a short-circuit at all frequencies. These assumptions greatly simplify the analysis with minimal impact on accuracy for moderate compression, while retaining the essential mechanism intact and isolated from the output self-biasing process previously explained.

The input self-biasing mechanism can be summarized as follows. Taking the PA circuit presented in Fig.4.2 as reference, the gate current, $i_{GS}(t)$ that flows through the nonlinear C_{GS} capacitance is a function of the C_{GS} variation with the applied instantaneous voltage, $C_{GS}[v_{gs}(t)]$ and the derivative of v_{gs} with respect to time. The function $C_{GS}(V_{GS})$ can be represented to arbitrary precision by a finite order static polynomial. When excited with a two-tone signal of half tone separation ω_m, the odd order terms in the polynomial expansion of $C_{GS}(V_{GS})$ (which originate even order terms in the charge function) generate current components at $2\omega_m$ and its harmonics, i.e. the device generates gate current at baseband frequencies. These components are converted into the voltage baseband components of $v_{gs}(t)$ depending on the baseband terminations presented by the IMN to the gate of the device. It is demonstrated in the publication that if $C_{GS}[v(t)]$ is approximated by the first order polynomial

$$C_{GS}(v(t)) = C_{gs0} + C_{gs1}v(t) \tag{4.2}$$

and the excitation is a two-tone signal of peak amplitude V_p, the baseband voltage component generated at the gate of the device is given by

$$v_{gs}(\tau) = \frac{1}{4}|Z_S(2\omega_m)|V_p^2 C_{gs1} \sin\left[2\omega_m\tau + \angle Z_S(2\omega_m)\right] \tag{4.3}$$

The major contribution of this analysis is a clear understanding of the relationship between the circuit and excitation parameters and the generated self-biasing, allowing PA designers to quickly estimate it and improve their designs accordingly. To demonstrate the self-biasing performance degradation and compensation, two PA prototypes have been built, as shown in Fig. 4.7. The conventional design presents a high quality factor resonance within 400MHz bandwidth, which creates a very high impedance peak at 225MHz. The proposed way to decrease the baseband impedance is to reduce the quality factor by introducing a parallel RC circuit in the input bias line and reducing the length of the bias line to push the resonance to a higher frequency. The baseband impedance profiles for each PA and the corresponding 2-tone average efficiency performance is are presented in Fig. 4.8 and Fig. 4.9.
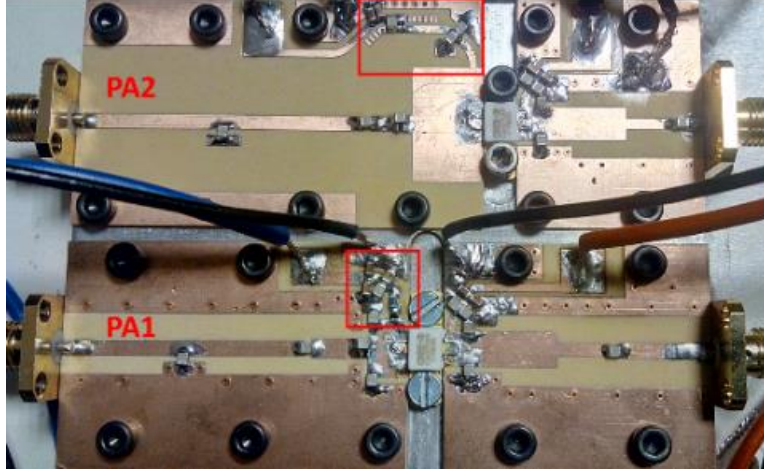
Figure 4.7: Photograph of the implemented PA prototypes, conventional bias network (top) and optimized bias network (bottom).
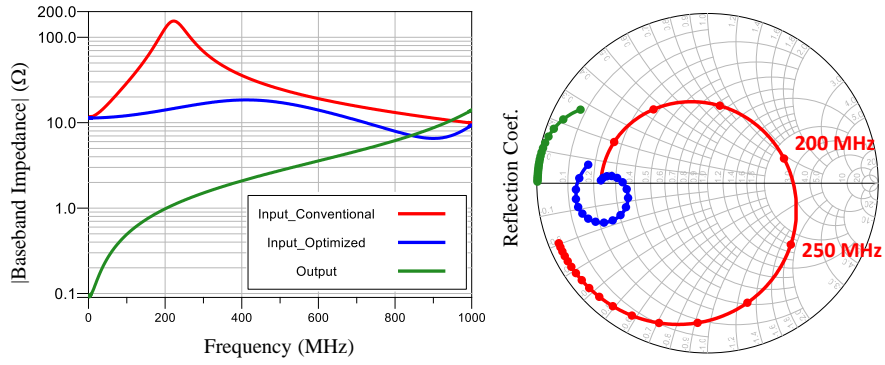

Figure 4.8: Simulated baseband impedance profiles at the intrinsic gate and drain reference planes for the designed input and output networks.
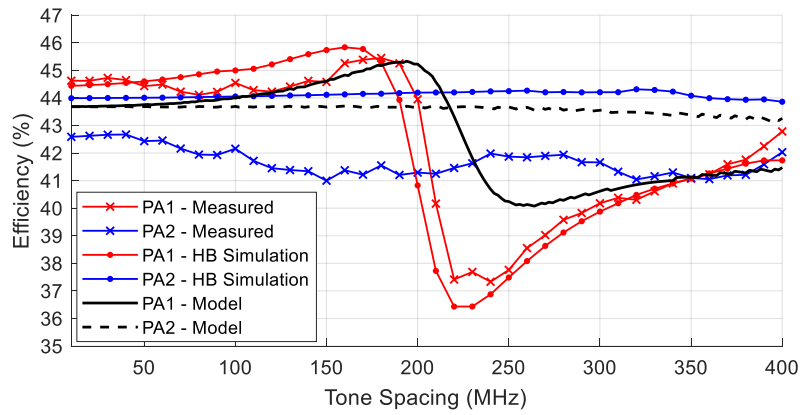

Figure 4.9: Average efficiency measurements for 2-tone excitation for several tone spacing values.

The experimental results depict a clear efficiency decrease when the tone separation matches the frequency region where the baseband impedance is high and is made almost completely flat when using the improved input bias network. It is relevant to note that this work is the first to clearly demonstrate this high efficiency degradation without the impact of the output baseband termination conditions, and the need to consider this mechanism at the design stage.

By applying the proposed modelling technique to this device, terminated with the designed input and output networks, we were able to predict the efficiency degradation profile. Since the model approximates the C_{GS} and I_{DS} relationship with V_{GS} using a low order polynomial and a simple piece-wise function, respectively, and assumes that v_{gs} is a pure two-tone signal, the approximation is only valid for mildly nonlinear excitation of C_{GS} and becomes inaccurate near the frequency where the input baseband impedance is highest due to the extreme nonlinear behaviour that it induces.

Nevertheless, this simple model attains the objectives of providing a clear qualitative explanation of the nonlinear mechanisms and the respective impact in the PA's performance, demonstrating that the input baseband impedance has not only the potential to degrade the linearity, as reported in the existing literature, but also a significant impact on the efficiency of wideband PAs.

This work was further extended for publication in the IEEE Transactions on Microwave Theory and Techniques (TMTT) journal and is presented in Annex D. The new contributions are:

- a more detailed analysis of how the baseband impedance imposes the gate bias point variation as the PA is driven from small signal into large-signal operation, and how we can infer the efficiency variation from independent power sweeps at distinct fixed bias points.

- experimental demonstration that the model's efficiency degradation prediction provides a good indication of the PA's performance for concurrent dual-band operation with realistic wireless communications signals.

The baseband input bias impedance is modelled as a dynamic change of the DC bias point of the device. Thus, knowing how the device performance changes with both the DC gate bias and the amplitude of the RF CW signal, and an estimation of the dynamic bias point change as a function of the amplitude, we can infer the consumed and output power as the two-tone envelope progresses in time and, therefore, calculate the average efficiency.

The quality of the efficiency estimate is a trade-off with the model complexity used for the nonlinear device elements. Since the baseband components of $i_{gs}(t)$ are primarily composed of even order intermodulation products, the C_{GS} charge model must be described, at least, by a second order polynomial, which implies a linear $C_{GS}(V_{GS})$ relationship. In addition, it should be noted that, in this work, we assume that the baseband generation is obtained by exciting C_{GS} with a pure 2-tone signal, in order to obtain an explicit formulation and simplifies the analysis. This approach leads to simple mathematical expressions relating the generated baseband components and the device's characteristics, at the expense of lower accuracy when large baseband components are generated, i.e. with baseband impedance terminations of large magnitude. In practice these do not occur with proper IMN design.

Since the gate bias point of the device may be increased to high values, the DC drain current model must be able to capture the current saturation of the device for high V_{GS}. In

this work we used a simple piecewise linear function to model the $I_{DS}(V_{GS})$ DC characteristic due to the simple mapping of its parameters to the device characteristics and the existence of closed form expressions for the fundamental and DC current. As CW simulations and measurements are simple to perform, and the proposed model to estimate the baseband V_{GS} is also based on simple approximations of the devices non-linear elements, we are able to both qualitatively explain and calculate the estimated 2-tone performance.

The absolute value and nature of the baseband impedance determine the amplitude and phase of the generated baseband voltage components. The phase is particularly important since it determines if the bias point is shifted to class-C or class-AB at key regions of the two-tone envelope. In this work we considered three baseband impedance scenarios, corresponding to predominantly inductive, capacitive or resistive natures.

By analyzing the change in class of operation as the RF envelope amplitude evolves in time and the expected CW change in output power and dc power, we are able to explain the device operation and predict the efficiency variation over a period of the envelope. The dynamic bias point can also be plotted over the CW efficiency and output power contours with swept V_{GS} and RF amplitude for fixed optimal RF load terminations, as shown in Fig. 4.10, Fig. 4.11 and Fig. 4.12 and thoroughly explained in the publication.

The performance change observed in the plots is predominantly determined by the high RF amplitude region of the RF envelope due to the low PAPR of a two-tone signal. However, realistic concurrent dual-band ODFM signals have higher PAPR, adding more relevance to intermediate power regions of the envelope.
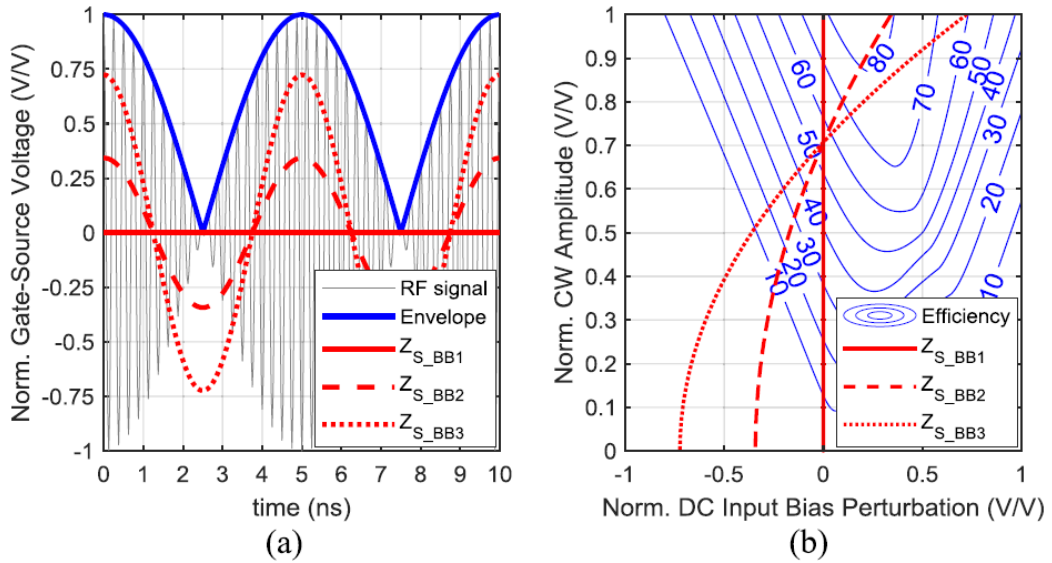
Figure 4.10: Model predicted (a) envelope of the two-tone signal and (b) efficiency contours, for three different purely inductive baseband impedance values.
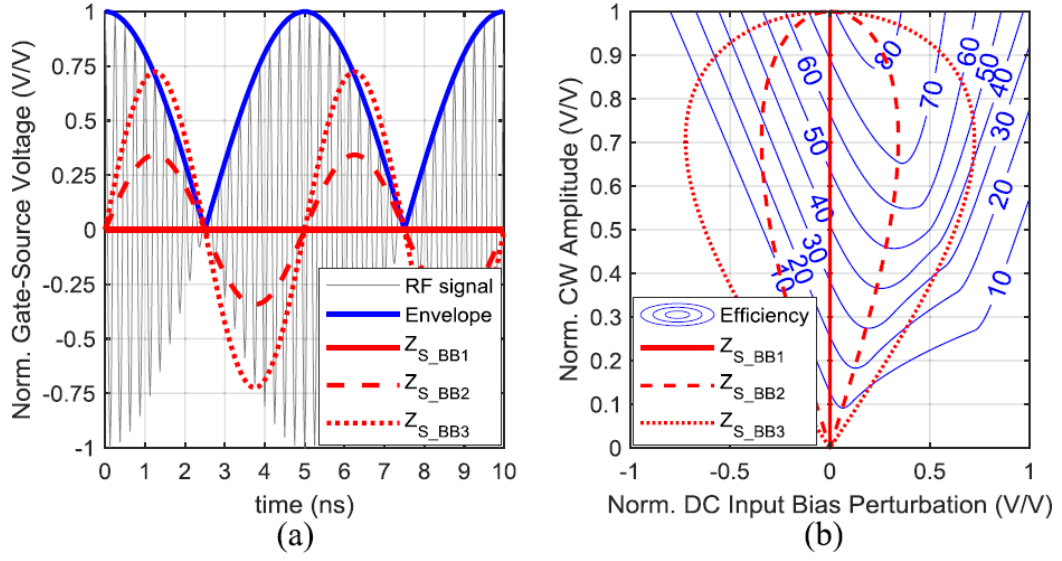
Figure 4.11: Model predicted (a) envelope of the two-tone signal and (b) efficiency contours, for three different purely resistive baseband impedance values.
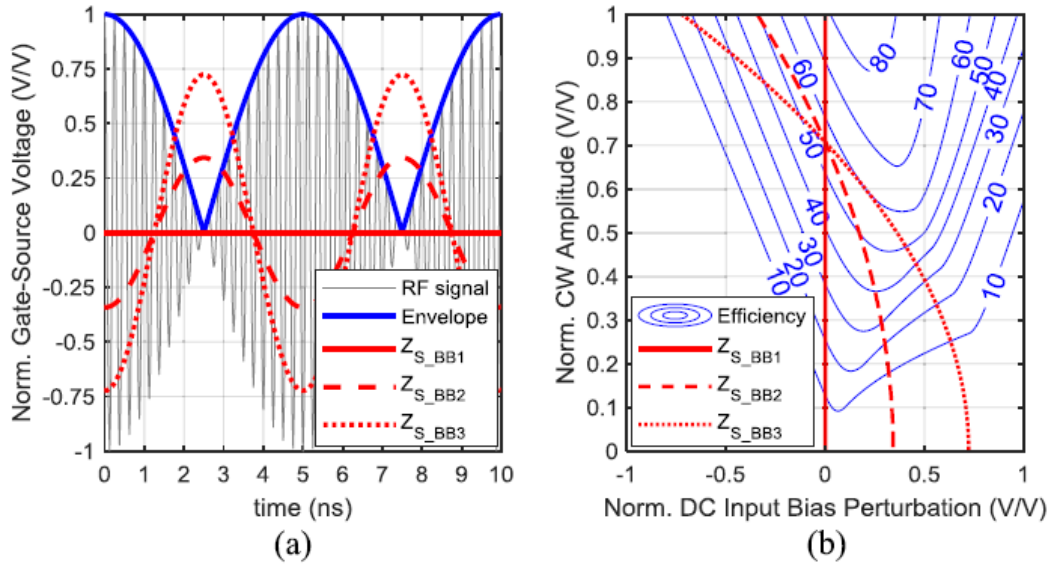
Figure 4.12: Model predicted (a) envelope of the two-tone signal and (b) efficiency contours, for three different purely capacitive baseband impedance values.

4.2.2 Experimental Validation

The second objective of the work is to demonstrate that the efficiency and linearity degradation profile estimated through the proposed method is also indicative of the PA's performance under concurrent dual-band excitation with realistic signals. To demonstrate this, the two implemented PAs were excited with dual-band 5 MHz OFDM signals, 9.7dB PAPR, at several band separations between 50 MHz and 400 MHz. The measured efficiency in each PA is presented in Fig.4.13, which exhibits the same efficiency variation profile that if observed in the two-tone measurement.
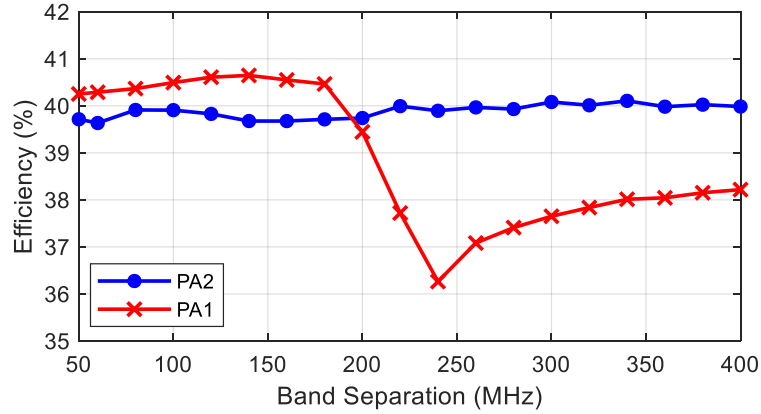
Figure 4.13: Measured average efficiency of each implemented PA under concurrent dual-band LTE signals, with 5 MHz bandwidth, for several band separations.

The ACPR at each band was also measured and is presented in Fig. 4.14, showing a clear linearity degradation in the same frequencies where the baseband impedance is highest. Both the efficiency and linearity degradations are minimized in the PA with optimized input baseband impedance. An additional test was made where the power of the two-tone signal was swept to evaluate the ACPR as a function of power. The result is presented in Fig. 4.15.
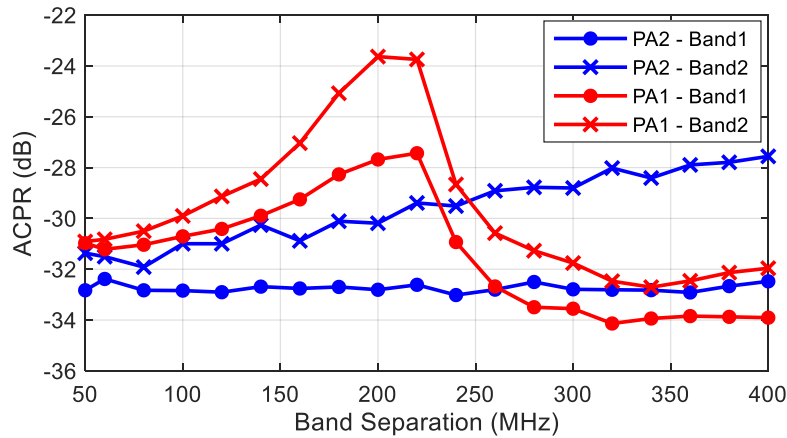
Figure 4.14: Measured ACPR of each implemented PA under concurrent dualband LTE signals, with 5 MHz bandwidth, for several band separations.
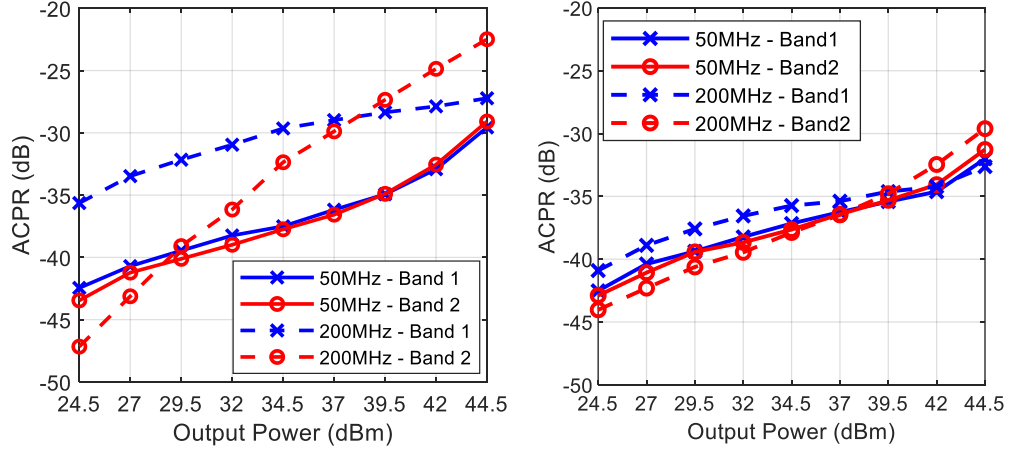
Figure 4.15: ACPR of a) PA1 and b) PA2 when operated in concurrent dual-band excitation, measured for several output peak power levels at each band calibrated in single-band operation using DPD.

The ACPR is significantly degraded even at a large back-off, which is consistent with the theoretical approach since the increased distortion originates from a change of class of operation at all power levels of the envelope, and not strictly from large-signal compression.

This concludes the study of the input baseband impedance and its implications on the PA's performance under concurrent band scenarios. The aforementioned contributions represent an important step in understanding concurrent dual-band PA operation and the development of improved design methodologies for high-efficiency operation. Naturally, these mechanisms occur not only in single-ended PAs but also in all high efficiency PA configurations, such as the Doherty, Chireix and LMBA, with the additional wideband load modulation design constraints.

Chapter 5

Conclusions and Achievements

The work developed in this PhD project was focused on RF PA's efficiency when driven with large bandwidth dual-band modulated signals, in order to identify and model the main video-bandwidth mechanisms that limit the performance.

The main source of efficiency variation was found to be the gate and drain self-biasing mechanisms due to the device's internal nonlinear capacitances and the nonlinear transconductance, which are both able to generate baseband current components under modulated signal excitation. Both mechanisms were thoroughly explained through nonlinear analysis, demonstrating that the baseband impedance imposed by the matching network determines how the bias voltages evolve in time for a given input envelope waveform. It was demonstrated that the drain and gate bias self-modulations have different origins and limit the performance is distinct ways.

The output baseband drain voltage modulation imposes a limit to the available output voltage swing depending on the envelope's waveform derivative, causing an asymmetric triode saturation profile, which is the origin of both efficiency degradation and side-band asymmetry previously reported in the literature. This mechanism causes both efficiency and linearity degradation under large-signal operation if the baseband impedance is not kept low enough during the design stage, making this determinant for optimal wideband operation.

The input baseband gate voltage modulation creates a time varying change of the operation class between class-AB, class-B and class-C as the envelope waveform evolves in time, which is shown to depend on the baseband impedance and the nonlinear C_{GS} profile. In particular, it is demonstrated that, for 2-tone and dual-band excitation, the nature of the baseband impedance determines the change in the class of operation in small and large signal, causing distinct efficiency performance profiles as the amplitude and bandwidth of the input signal increase. Contrary to the drain self-biasing mechanism, the performance degradation can occur not only at small but also at large signal since it is caused by C_{GS} variation with the envelope, causing linearity degradation and side-band asymmetry at low power levels and efficiency degradation at large signal as the bandwidth of the input signal increases.

New modelling strategies were developed for all the identified mechanisms through nonlinear analysis and polynomial approximations of the nonlinear elements responsible for baseband component generation. The modeling approach is rooted in physical device parameters, bias and loading conditions, facilitating the model utility in PA design while preserving an intuitive prediction of the change in the device's inner operation conditions. All models were experimentally validated by predicting the performance variation of several PA prototypes

designed with distinct baseband terminations.

It is also shown and experimentally demonstrated that the performance degradation can be prevented in wideband excitation through appropriate design of the matching networks for each type of video-bandwidth mechanism. Although the theoretical analysis is based on simplified 2-Tone excitation, it was observed that the measured efficiency using wideband dual-band OFDM signals follow the same profiles as predicted by the models at the same frequency band separations as the two-tone frequency separations. As such, the simplified analysis is suitable for estimating the instantaneous bandwidth of the PA at the design stage for usual wideband multi-band scenarios in wireless communications.

Several contributions of this research work to the state-of-the-art have been published and are summarized below, closely following the objectives for this PhD research project.

Journal Publications

- L. C. Nunes, **Diogo R. Barros**, P. M. Cabral, and J. C. Pedro, "Efficiency Degradation Analysis in Wideband Power Amplifiers", IEEE Tran. Microw. Theory Techn., vol. 66, no. 12, pp. 5640-5651, Dec. 2018

- **Diogo R. Barros**, L. C. Nunes, P. M. Cabral, and J. C. Pedro, "Impact of the Input Baseband Terminations on the Efficiency of Wideband Power Amplifiers under Concurrent Band Operation", IEEE Tran. Microw. Theory Techn., vol. 67, no. 12, pp. 5127-5138, Dec. 2019

- J. Louro, C. Belchior, **D. R. Barros**, F. M. Barradas, L. C. Nunes, P. M. Cabral, J. C. Pedro, "New Transistor Behavioral Model Formulation Suitable for Doherty PA Design," in IEEE Tran. on Microw. Theory Techn., vol. 69, no. 4, pp. 2138-2147, April 2021, doi: 10.1109/TMTT.2021.3054645.

Conference Publications

- L. C. Nunes, **Diogo R. Barros**, P. M. Cabral, and J. C. Pedro, "Efficiency Degradation in Wideband Power Amplifiers," IEEE MTT-S Int. Microw. Symp. Dig., Philadelphia, PA, 2018, pp. 636-639.

- **Diogo R. Barros**, L. C. Nunes, P. M. Cabral, and J. C. Pedro, "Impact of the Input Baseband Impedance on the Instantaneous Bandwidth of Wideband Power Amplifiers," IEEE MTT-S Int. Microw. Symp. Dig., Boston, MA, 2019, pp. 1171-1174

- L. C. Nunes, F. Barradas, **Diogo R. Barros**, P. M. Cabral, and J. C. Pedro, "Current Mode Outphasing Power Amplifier," IEEE MTT-S Int. Microw. Symp. Dig., Boston, MA, 2019, pp. 1160-1163

5.1 Future Work

Due to the permanent drive for high data-rate and bandwidth, the study of video bandwidth degradation mechanisms is determinant for enabling high-efficiency performance in future wireless communication systems. The results of this work consolidate the understanding of each of these mechanisms in isolation and their impact on the efficiency of single-ended PA, and could be extended further in the following aspects:

- **Extension to Wideband Operation Scenarios**
  The proposed analysis and models have targeted concurrent dual-band operation and could be extended to scenarios where the band separation is so large that the baseband and fundamental components start to become close, or even mixed. In this case, the baseband can no longer be considered as a slow change of the bias point, and therefore, a new modelling approach is necessary. This idea could even be taken to the extreme scenario of considering a true wideband signal instead of a multi-band excitation, whose bandwidth would generate a continuous baseband spectra that overlaps with the signal itself.

- **Modelling of the Non-linear Distortion Generation**
  Although efficiency is often the most desired figure of merit to optimize, there are other applications that cannot fully rely on DPD techniques for linearization. A model that could make basic predictions of the distortion generated on each fundamental band due to the video bandwidth mechanisms could provide valuable information to guide the development of optimized circuits and systems for compensation of these particular long-term memory effects.

- **Video Bandwidth Mechanisms' Impact on Load Modulated PAs**
  Single-ended PA are a good starting point to study, understand and model the basic mechanisms and their impact on PAs' performance. However, in order to achieve high efficiency for the high PAPR of modern communication signals, the output stage of base-station transmitters' are composed of several devices connected in specific high-efficiency architectures, most notably Doherty PAs. Research has focused on extending the bandwidth limitations of Doherty PAs and on the development of other wideband architectures, such as the Doherty-Outphasing Continuum design space and the LMBA. Therefore, the analysis of video bandwidth degradation mechanisms applied to these advanced architectures would be of high interest to the industry with immediate application in current products.

- **Baseband Waveform Engineering and Optimal Baseband Terminations**
  In this work, the analysis is made for the several mechanisms in isolation and is restricted to the first baseband component. Therefore, it corresponds to a simple sinusoidal bias point variation with a specified phase with respect to the envelope, given by the nature of the baseband impedance. However, in general, all baseband components are present at the same time, both at the gate and drain of the device and can create different waveforms depending on all baseband terminations. Hence, it would be interesting to investigate if there are other baseband impedance profiles that could provide optimal performance, in alternative to the usual approach, i.e. to minimize their magnitude which becomes very difficult at high fractional bandwith.

References and Bibliography

[1] Ericsson, "Ericsson Mobility Report - June 2021," Ericsson Group, Tech. Rep. June, 2021. [Online]. Available: https://www.ericsson.com/49e50d/assets/local/mobility-report/documents/2021/june-2021-ericsson-mobility-report.pdf

[2] J. Wu, Y. Zhang, M. Zukerman, and E. K. N. Yung, "Energy-efficient base-stations sleep-mode techniques in green cellular networks: A survey," *IEEE Commun. Surv. Tutorials*, vol. 17, no. 2, pp. 803–826, 2015.

[3] G. Auer, V. Giannini, C. Desset, I. Gódor, P. Skillermark, M. Olsson, M. A. Imran, D. Sabella, M. J. Gonzalez, O. Blume, and A. Fehske, "How much energy is needed to run a wireless network?" *IEEE Wirel. Commun.*, vol. 18, no. 5, pp. 40–49, 2011.

[4] A. Fehske, J. Malmodin, G. Biczok, and G. Fettweis, "The Global Carbon Footprint of Mobile Communications - The Ecological and Economic Perspective," *IEEE Commun. Mag.*, vol. 49, no. 8, pp. 55–62, 2011.

[5] C. Liu, B. Natarajan, and H. Xia, "Small cell base station sleep strategies for energy efficiency," *IEEE Transactions on Vehicular Technology*, vol. 65, no. 3, pp. 1652–1661, 2016.

[6] F. Han, S. Zhao, L. Zhang, and J. Wu, "Survey of strategies for switching off base stations in heterogeneous networks for greener 5g systems," *IEEE Access*, vol. 4, pp. 4959–4973, 2016.

[7] J. Wu, Y. Zhang, M. Zukerman, and E. K.-N. Yung, "Energy-efficient base-stations sleep-mode techniques in green cellular networks: A survey," *IEEE Communications Surveys Tutorials*, vol. 17, no. 2, pp. 803–826, 2015.

[8] H. Holtkamp, G. Auer, S. Bazzi, and H. Haas, "Minimizing base station power consumption," *IEEE Journal on Selected Areas in Communications*, vol. 32, no. 2, pp. 297–306, 2014.

[9] D. Liu and C. Yang, "Energy efficiency of downlink networks with caching at base stations," *IEEE Journal on Selected Areas in Communications*, vol. 34, no. 4, pp. 907–922, 2016.

[10] Y. Liu, Y. Wang, R. Sun, S. Meng, and R. Su, "Energy efficient downlink resource allocation for d2d-assisted cellular networks with mobile edge caching," *IEEE Access*, vol. 7, pp. 2053–2067, 2019.

[11] Nokia, "Anual Report," 2012. [Online]. Available: https://www.nokia.com/about-us/investors/results-reports/

[12] P. Wright, J. Lees, P. J. Tasker, J. Benedikt, and S. C. Cripps, "An efficient, linear, broadband class-J-mode PA realised using RF waveform engineering," *IEEE MTT-S Int. Microw. Symp. Dig.*, pp. 653–656, 2009.

[13] P. Wright, J. Lees, J. Benedikt, P. J. Tasker, and S. C. Cripps, "A methodology for realizing high efficiency class-J in a Linear and Broadband PA," *IEEE Trans. Microw. Theory Tech.*, vol. 57, no. 12, pp. 3196–3204, 2009.

[14] T. Canning, P. J. Tasker, and S. C. Cripps, "Continuous mode power amplifier design using harmonic clipping contours: Theory and practice," *IEEE Trans. Microw. Theory Tech.*, vol. 62, no. 1, pp. 100–110, 2014.

[15] R. Quaglia, J. J. Bell, and S. Cripps, "New General Formulation and Experimental Verification of Harmonic Clipping Contours in High-Frequency Power Devices," *IEEE Trans. Microw. Theory Tech.*, vol. 65, no. 10, pp. 3903–3909, 2017.

[16] S. C. Cripps, P. J. Tasker, A. L. Clarke, J. Lees, and J. Benedikt, "On the continuity of high efficiency modes in linear RF power amplifiers," *IEEE Microw. Wirel. Components Lett.*, vol. 19, no. 10, pp. 665–667, 2009.

[17] V. Carrubba, a. L. Clarke, M. Akmal, J. Lees, J. Benedikt, P. J. Tasker, and S. C. Cripps, "The Continuous Class-F Mode Power Amplifier," *Microw. Conf. (EuMC), 2010 Eur.*, no. September, pp. 24–27, 2010.

[18] V. Carrubba, A. L. Clarke, M. Akmal, J. Lees, J. Benedikt, P. J. Tasker, and S. C. Cripps, "On the extension of the continuous class-F mode power amplifier," *IEEE Trans. Microw. Theory Tech.*, vol. 59, no. 5, pp. 1294–1303, 2011.

[19] C. Friesicke and A. F. Jacob, "Mode continua for Inverse Class-F RF power amplifiers," *Microw. Conf. (GeMIC), 2011 Ger.*, no. March, pp. 1–4, 2011.

[20] V. Carrubba, M. Akmal, R. Quay, J. Lees, J. Benedikt, S. C. Cripps, and P. J. Tasker, "The continuous inverse class-F mode with resistive second-harmonic impedance," *IEEE Trans. Microw. Theory Tech.*, vol. 60, no. 6 PART 2, pp. 1928–1936, 2012.

[21] K. Chen and D. Peroulis, "Design of broadband high-efficiency power amplifier using in-band Class-F 1/F mode-transferring technique," *IEEE MTT-S Int. Microw. Symp. Dig.*, pp. 1–3, 2012.

[22] ——, "Design of broadband highly efficient harmonic-tuned power amplifier using in-band continuous class-F-1F mode transferring," *IEEE Trans. Microw. Theory Tech.*, vol. 60, no. 12, pp. 4107–4116, dec 2012.

[23] M. Ozen, R. Jos, and C. Fager, "Continuous class-e power amplifier modes," *IEEE Trans. Circuits Syst. II Express Briefs*, vol. 59, no. 11, pp. 731–735, 2012.

[24] J. Chen, S. He, F. You, R. Tong, and R. Peng, "Design of broadband high-efficiency power amplifiers based on a series of continuous modes," *IEEE Microw. Wirel. Components Lett.*, vol. 24, no. 9, pp. 631–633, 2014.

[25] W. Shi, S. He, and Q. Li, "A Series of Inverse Continuous Modes for Designing Broadband Power Amplifiers," *IEEE Microw. Wirel. Components Lett.*, vol. 26, no. 7, pp. 525–527, 2016.

[26] S. Rezaei, L. Belostotski, M. Helaoui, and F. M. Ghannouchi, "Harmonically tuned continuous class-c operation mode for power amplifier applications," *IEEE Trans. Microw. Theory Tech.*, vol. 62, no. 12, pp. 3017–3027, 2014.

[27] X. Li, M. Helaoui, and X. Du, "Class-X - Harmonically Tuned Power Amplifiers with Maximally Flat Waveforms Suitable for over One-Octave Bandwidth Designs," *IEEE Trans. Microw. Theory Tech.*, vol. 66, no. 4, pp. 1939–1950, 2018.

[28] N. Tuffy, L. Guan, A. Zhu, and T. J. Brazil, "A simplified broadband design methodology for linearized high-efficiency continuous class-F power amplifiers," *IEEE Trans. Microw. Theory Tech.*, vol. 60, no. 6 PART 2, pp. 1952–1963, 2012.

[29] Z. Lu and W. Chen, "Resistive second-harmonic impedance continuous class-F power amplifier with over one octave bandwidth for cognitive radios," *IEEE J. Emerg. Sel. Top. Circuits Syst.*, vol. 3, no. 4, pp. 489–497, 2013.

[30] T. Sharma, R. Darraji, and F. Ghannouchi, "Design methodology of high efficiency continuous mode transfer power amplifiers with one octave bandwidth," in *2014 21st IEEE Int. Conf. Electron. Circuits Syst. ICECS 2014*, 2014, pp. 674–677.

[31] M. Yang, J. Xia, Y. Guo, and A. Zhu, "Highly Efficient Broadband Continuous Inverse Class-F Power Amplifier Design Using Modified Elliptic Low-Pass Filtering Matching Network," *IEEE Trans. Microw. Theory Tech.*, vol. 64, no. 5, pp. 1515–1525, 2016.

[32] Q. Li, S. He, Z. Dai, and W. Shi, "A Method for Designing Generalized Continuous Power Amplifier," in *2016 IEEE MTT-S Int. Microw. Work. Ser. Adv. Mater. Process. RF THz Appl.*, vol. 91, 2016, pp. 399–404.

[33] Q. Li, S. He, W. Shi, Z. Dai, and T. Qi, "Extend the Class-B to Class-J Continuum Mode by Adding Arbitrary Harmonic Voltage Elements," *IEEE Microw. Wirel. Components Lett.*, vol. 26, no. 7, pp. 522–524, 2016.

[34] Y. Dong, L. Mao, and S. Xie, "Extended Continuous Inverse Class-F Power Amplifiers with Class-AB Bias Conditions," *IEEE Microw. Wirel. Components Lett.*, vol. 27, no. 4, pp. 368–370, 2017.

[35] Q. H. Tang, Y. H. Li, and W. G. Li, "Over second octave power amplifier design based on resistive-resistive series of continuous class-F/F-1 Modes," *IEEE Microw. Wirel. Components Lett.*, vol. 27, no. 5, pp. 494–496, 2017.

[36] C. Huang, S. He, W. Shi, and B. Song, "Design of Broadband High-Efficiency Power Amplifiers Based on the Hybrid Continuous Modes with Phase Shift Parameter," *IEEE Microw. Wirel. Components Lett.*, vol. 28, no. 2, pp. 159–161, 2018.

[37] J. Wang, S. He, F. You, W. Shi, J. Peng, and C. Li, "Codesign of High-Efficiency Power Amplifier and Ring-Resonator Filter Based on a Series of Continuous Modes and Even-Odd-Mode Analysis," *IEEE Trans. Microw. Theory Tech.*, vol. 66, no. 6, pp. 2867–2878, 2018.

[38] F. You, C. Li, W. Shi, and S. He, "Design of a 1.4 - 3.6 GHz High-Efficiency Broadband Power Amplifiers with Mixed Operation Modes," in *2018 Asia-Pacific Microw. Conf.*, 2018, pp. 944–946.

[39] N. Poluri and M. M. De Souza, "High-efficiency modes contiguous with class b/j and continuous class f -1 amplifiers," *IEEE Microw. Wirel. Components Lett.*, vol. 29, no. 2, pp. 137–139, 2019.

[40] F. Raab, P. Asbeck, S. Cripps, P. Kenington, Z. Popovic, N. Pothecary, J. Sevic, and N. Sokal, "Power amplifiers and transmitters for RF and microwave," *IEEE Trans. Microw. Theory Tech.*, vol. 50, no. 3, pp. 814–826, mar 2002.

[41] Wan-Jong Kim, S. Stapleton, Kyoung Joon Cho, and Jong Heon Kim, "Digital predistortion of a doherty amplifier with a weak memory within a connected solution," in *IEEE 60th Veh. Technol. Conf. 2004. VTC2004-Fall. 2004*, vol. 3. IEEE, 2004, pp. 2020–2023.

[42] S. Hong, Y. Y. Woo, J. Kim, J. Cha, I. Kim, J. Moon, J. Yi, and B. Kim, "Weighted polynomial digital predistortion for low memory effect doherty power amplifier," *IEEE Trans. Microw. Theory Tech.*, vol. 55, no. 5, pp. 925–930, 2007.

[43] J. Wood, *Behavioral Modeling and Linearization of RF Power Amplifiers.* Norwood, MA: Artech House, Inc., 2014.

[44] W. Doherty, "A New High Efficiency Power Amplifier for Modulated Waves," *Proc. IRE*, vol. 24, no. 9, pp. 1163–1182, sep 1936.

[45] K. Bathich, A. Z. Markos, and G. Boeck, "Frequency response analysis and bandwidth extension of the Doherty amplifier," *IEEE Trans. Microw. Theory Tech.*, vol. 59, no. 4 PART 1, pp. 934–944, 2011.

[46] M. Sarkeshi, O. B. Leong, and A. Van Roermund, "A novel doherty amplifier for enhanced load modulation and higher bandwidth," in *IEEE MTT-S Int. Microw. Symp. Dig.*, no. 1. IEEE, jun 2008, pp. 763–766.

[47] D. Y. T. Wu and S. Boumaiza, "A modified doherty configuration for broadband amplification using symmetrical devices," *IEEE Trans. Microw. Theory Tech.*, vol. 60, no. 10, pp. 3201–3213, 2012.

[48] E. Bertran and M. Yahyavi, "A Wideband Doherty-Like Architecture Using a Klopfenstein Taper for Load Modulation," *IEEE Microw. Wirel. Components Lett.*, vol. 25, no. 11, pp. 760–762, 2015.

[49] K. Bathich, A. Markos, and G. Boeck, "A wideband GaN Doherty amplifier with 35 % fractional bandwidth," *Microw. Conf. (EuMC), 2010 Eur.*, no. September, pp. 1006–1009, 2010.

[50] B. Kim, J. Kim, I. Kim, and J. Cha, "The Doherty Power Amplifer," *IEEE Microw. Mag.*, vol. 7, no. October, pp. 42–50, oct 2006.

[51] R. Darraji and F. M. Ghannouchi, "Digital doherty amplifier with enhanced efficiency and extended range," *IEEE Trans. Microw. Theory Tech.*, vol. 59, no. 11, pp. 2898–2909, 2011.

[52] R. Giofre, P. Colantonio, F. Giannini, and L. Piazzon, "New output combiner for doherty amplifiers," *IEEE Microw. Wirel. Components Lett.*, vol. 23, no. 1, pp. 31–33, 2013.

[53] L. Piazzon, R. Giofre, R. Quaglia, V. Camarchia, M. Pirola, P. Colantonio, F. Giannini, and G. Ghione, "Effect of load modulation on phase distortion in doherty power amplifiers," *IEEE Microw. Wirel. Components Lett.*, vol. 24, no. 7, pp. 505–507, 2014.

[54] L. Piazzon, R. Giofre, P. Colantonio, and F. Giannini, "A wideband doherty architecture with 36% of fractional bandwidth," *IEEE Microw. Wirel. Components Lett.*, vol. 23, no. 11, pp. 626–628, nov 2013.

[55] R. Giofr??, L. Piazzon, P. Colantonio, and F. Giannini, "An ultra-broadband GaN Doherty amplifier with 83% of fractional bandwidth," *IEEE Microw. Wirel. Components Lett.*, vol. 24, no. 11, pp. 775–777, 2014.

[56] X. H. Fang and K. K. M. Cheng, "Improving Power Utilization Factor of Broadband Doherty Amplifier by Using Bandpass Auxiliary Transformer," *IEEE Trans. Microw. Theory Tech.*, vol. 63, no. 9, pp. 2811–2820, 2015.

[57] J. Pang, S. He, C. Huang, Z. Dai, J. Peng, and F. You, "A Post-Matching Doherty Power Amplifier Employing Low-Order Impedance Inverters for Broadband Applications," *IEEE Trans. Microw. Theory Tech.*, vol. 63, no. 12, pp. 4061–4071, 2015.

[58] X. Y. Zhou, S. Y. Zheng, W. S. Chan, and D. Ho, "Efficiency enhanced post-matching Doherty power amplifier based on modified phase compensation network," in *2017 IEEE MTT-S Int. Microw. Symp.* IEEE, jun 2017, pp. 785–788.

[59] X. Y. Zhou, S. Y. Zheng, W. S. Chan, S. Chen, and D. Ho, "Broadband Efficiency-Enhanced Mutually Coupled Harmonic Postmatching Doherty Power Amplifier," *IEEE Trans. Circuits Syst. I Regul. Pap.*, vol. 64, no. 7, pp. 1758–1771, jul 2017.

[60] X. Chen, W. Chen, F. M. Ghannouchi, and Z. Feng, "A 1.1GHz bandwidth, 46%-62% efficiency Continuous Mode Doherty Power Amplifier," in *IEEE MTT-S Int. Microw. Symp. Dig.*, vol. 2016-Augus. IEEE, 2016, pp. 1–4.

[61] X. Chen, W. Chen, Q. Zhang, F. M. Ghannouchi, and Z. Feng, "A 200 watt broadband continuous-mode doherty power amplifier for base-station applications," in *IEEE MTT-S Int. Microw. Symp. Dig.* IEEE, jun 2017, pp. 1110–1113.

[62] X. Y. Zhou, W. S. Chan, S. Y. Zheng, W. J. Feng, and D. Ho, "Broadband High Efficiency Post-matching Doherty Power Amplifier Based on Mixed-Topology," in *2018 IEEE/MTT-S Int. Microw. Symp. - IMS*, vol. 2018-June. IEEE, jun 2018, pp. 450–453.

[63] Z. Yang, M. Li, Y. Yao, Z. Dai, T. Li, and Y. Jin, "Design of Concurrent Dual-Band Continuous Class-J Mode Doherty Power Amplifier with Precise Impedance Terminations," *IEEE Microw. Wirel. Components Lett.*, vol. 29, no. 5, pp. 348–350, may 2019.

[64] D. Kang, D. Kim, J. Moon, and B. Kim, "Broadband HBT doherty power amplifiers for handset applications," in *IEEE Trans. Microw. Theory Tech.*, vol. 58, no. 12 PART 2. IEEE, dec 2010, pp. 4031–4039.

[65] J. H. Qureshi, N. Li, W. C. Neo, F. Van Rijs, I. Blednov, and L. C. De Vreede, "A wide-band 20W LMOS Doherty power amplifier," in *IEEE MTT-S Int. Microw. Symp. Dig.*, vol. 2, no. 1, 2010, pp. 1504–1507.

[66] G. Sun and R. H. Jansen, "Broadband Doherty power amplifier via real frequency technique," *IEEE Trans. Microw. Theory Tech.*, vol. 60, no. 1, pp. 99–111, 2012.

[67] A. Cidronali, S. Maddio, N. Giovannelli, and G. Collodi, "Frequency Analysis and Multiline Implementation of Compensated Impedance Inverter for Wideband Doherty High-Power Amplifier Design," *IEEE Trans. Microw. Theory Tech.*, vol. 64, no. 5, pp. 1359–1372, 2016.

[68] R. Darraji, F. M. Ghannouchi, and M. Helaoui, "Mitigation of bandwidth limitation in wireless doherty amplifiers with substantial bandwidth enhancement using digital techniques," *IEEE Trans. Microw. Theory Tech.*, vol. 60, no. 9, pp. 2875–2885, 2012.

[69] A. Piacibello, M. Pirola, V. Camarchia, C. Ramella, R. Quaglia, X. Zhou, and W. S. Chan, "Comparison of S-Band Analog and Dual-Input Digital Doherty Power Amplifiers," in *2018 48th Eur. Microw. Conf.* IEEE, sep 2018, pp. 1237–1240.

[70] H. Chireix, "High Power Outphasing Modulation," *Proc. Inst. Radio Eng.*, vol. 23, no. 11, pp. 1370–1392, nov 1935.

[71] L. Nunes, F. Barradas, D. Barros, P. Cabral, and J. Pedro, "Current Mode Outphasing Power Amplifier," in *IEEE MTT-S Int. Microw. Symp.*, 2019.

[72] T. W. Barton and D. J. Perreault, "An RF-input outphasing power amplifier with RF signal decomposition network," *2015 IEEE MTT-S Int. Microw. Symp. IMS 2015*, pp. 1–4, 2015.

[73] T. Barton and D. Perreault, "Theory and Implementation of RF-Input Outphasing Power Amplification," *IEEE Trans. Microw. Theory Tech.*, vol. 63, no. 12, pp. 4273–4283, 2015.

[74] A. Piacibello, R. Quaglia, M. Pirolaf, and S. Cripps, "Design of an S-Band Chireix Outphasing Power Amplifier Based on a Systematic Bandwidth Limitation Analysis," in *2018 13th Eur. Microw. Integr. Circuits Conf.*, 2018, pp. 186–189.

[75] P. Roblin, F. J. Martinez-Rodriguez, H. C. Chang, C. Xie, and J. I. Martinez-Lopez, "Transistor characterization and modeling and the use of embedding device models for the design of microwave power amplifiers," *Int. Work. Integr. Nonlinear Microw. Millimetre-wave Circuits, INMMiC 2015*, pp. 1–6, 2015.

[76] P. Roblin, H.-C. Chang, C. Liang, R. Alsulami, F. Martinez-Rodriguez, and J. A. Galaviz Aguilar, "Direct design of Doherty and Chireix PAs using a nonlinear embedding device model," *2017 IEEE Top. Conf. RF/Microwave Power Amplifiers Radio Wirel. Appl.*, pp. 44–47, 2017.

[77] J. H. Qureshi, M. J. Pelk, M. Marchetti, W. C. Neo, J. R. Gajadharsing, M. P. Van Der Heijden, and L. C. De Vreede, "A 90-W peak power GaN outphasing amplifier with optimum input signal conditioning," *IEEE Trans. Microw. Theory Tech.*, vol. 57, no. 8, pp. 1925–1935, 2009.

[78] D. A. Calvillo-Cortes and L. C. N. De Vreede, "Analysis of pure- and mixed-mode class-B outphasing amplifiers," *2014 IEEE 5th Lat. Am. Symp. Circuits Syst. LASCAS 2014 - Conf. Proc.*, pp. 0–3, 2014.

[79] A. R. Qureshi, M. Acar, J. Qureshi, R. Wesson, and L. C. De Vreede, "A 112W GaN dual input Doherty-Outphasing Power Amplifier," *IEEE MTT-S Int. Microw. Symp. Dig.*, vol. 2016-Augus, pp. 1–4, 2016.

[80] C. M. Andersson, D. Gustafsson, J. Chani Cahuana, R. Hellberg, and C. Fager, "A 1-3-GHz Digitally Controlled Dual-RF Input Power-Amplifier Design Based on a Doherty-Outphasing Continuum Analysis," *IEEE Trans. Microw. Theory Tech.*, vol. 61, no. 10, pp. 3743–3752, 2013.

[81] D. Gustafsson, C. M. Andersson, R. Hellberg, and C. Fager, "A 44 dBm 1.0-3.0 GHz GaN power amplifier with over 45% PAE at 6 dB back-off," *IEEE MTT-S Int. Microw. Symp. Dig.*, pp. 1–4, 2013.

[82] D. Gustafsson, *Extending the bandwidth of the doherty power amplifier.*, ser. Doktorsavhandlingar vid Chalmers tekniska högskola Ny serie: 3748. Chalmers University of Technology, 2014. [Online]. Available: https://search.ebscohost.com/login.aspx?direct=true{&}db=cat07470a{&}AN=clc. 0934a081.576c.427c.ac95.d2f1043a3c10{&}site=eds-live{&}scope=site{&}authtype= guest{&}custid=s3911979{&}groupid=main{&}profile=eds

[83] S. Chung, R. Ma, S. Shinjo, H. Nakamizo, K. Parsons, and K. H. Teo, "Concurrent multi-band digital outphasing transmitter architecture using multidimensional power coding," *IEEE Trans. Microw. Theory Tech.*, vol. 63, no. 2, pp. 598–613, 2015.

[84] N. B. De Carvalho and J. C. Pedro, "A comprehensive explanation of distortion sideband asymmetries," *IEEE Trans. Microw. Theory Tech.*, vol. 50, no. 9, pp. 2090–2101, 2002.

[85] B. Bunz, A. Ahmed, and G. Kompa, "Influence of envelope impedance termination on RF behaviour of GaN HEMT power devices," *35th Eur. Microw. Conf. 2005 - Conf. Proc.*, vol. 3, pp. 1595–1598, 2005.

[86] P. M. Cabral, J. C. Pedro, and N. B. Carvalho, "Bias networks impact on the dynamic AM/AM contours in microwave power amplifiers," in *2006 Int. Work. Integr. Nonlinear Microw. Millimeter-Wave Circuits, INMMIC 2006 - Proc.* IEEE, jan 2007, pp. 38–41.

[87] M. Akmal, J. Lees, S. Bensmida, S. Woodington, V. Carrubba, S. Cripps, J. Benedikt, K. Morris, M. Beach, J. McGeehan, and P. Tasker, "The effect of baseband impedance termination on the linearity of GaN HEMTs," *Microw. Conf. (EuMC), 2010 Eur.*, no. September, pp. 1046–1049, 2010.

[88] X. Chen, W. Chen, F. M. Ghannouchi, and Z. Feng, "A novel design method of concurrent dual-band power amplifiers including impedance tuning at inter-band modulation frequencies," in *IEEE MTT-S Int. Microw. Symp. Dig.*, no. 1. IEEE, 2013, pp. 1–4.

[89] X. Chen, W. Chen, F. M. Ghannouchi, Z. Feng, and Y. Liu, "Enhanced analysis and design method of concurrent dual-band power amplifiers with intermodulation impedance tuning," *IEEE Trans. Microw. Theory Tech.*, vol. 61, no. 12, pp. 4544–4558, 2013.

[90] X. Chen, W. Chen, G. Su, F. M. Ghannouchi, and Z. Feng, "A concurrent dual-band 1.9-2.6-GHz Doherty power amplifier with Intermodulation impedance tuning," in *IEEE MTT-S Int. Microw. Symp. Dig.*, 2014, pp. 6–9.

[91] M. Akmal, J. Lees, S. Jiangtao, V. Carrubba, Z. Yusoff, S. Woodington, J. Benedikt, P. J. Tasker, S. Bensmida, K. Morris, M. Beach, and J. McGeehan, "An enhanced modulated waveform measurement system for the robust characterization of microwave devices under modulated excitation," in *2011 6th Eur. Microw. Integr. Circuit Conf.*, 2011, pp. 180–183.

[92] W. Sear and T. W. Barton, "A baseband feedback approach to linearization of a uhf power amplifier," in *2019 IEEE MTT-S International Microwave Symposium (IMS)*, 2019, pp. 75–78.

[93] E. Kuwata, Y. Alimohammadi, X. Liu, J. Bell, P. Tasker, S. Shinjo, and J. Benedikt, "Effects of Load Impedances at Third Order Intermodulation Tones," in *2020 15th Eur. Microw. Integr. Circuits Conf.*, 2021, pp. 201–204.

[94] L. Nunes, D. Barros, P. Cabral, and J. Pedro, "Efficiency Degradation Analysis in Wideband Power Amplifiers," *IEEE Trans. Microw. Theory Tech.*, vol. 66, no. 12, pp. 5640–5651, dec 2018.

[95] L. C. Nunes, D. R. Barros, P. M. Cabral, and J. C. Pedro, "Efficiency Degradation in Wideband Power Amplifiers," in *2018 IEEE/MTT-S Int. Microw. Symp. - IMS*, vol. 66, no. 12.   IEEE, jun 2018, pp. 636–639.

[96] D. Barros, L. Nunes, P. Cabral, and J. Pedro, "Impact of the Input Baseband Impedance on the Instantaneous Bandwidth of Wideband Power Amplifiers," in *IEEE MTT-S Int. Microw. Symp.*, 2019, pp. 2–4.

[97] D. R. Barros, L. C. Nunes, P. M. Cabral, and J. C. Pedro, "Impact of the Input Baseband Terminations on the Efficiency of Wideband Power Amplifiers Under Concurrent Band Operation," *IEEE Trans. Microw. Theory Tech.*, vol. 67, no. 12, pp. 5127–5138, 2019.

Appendix A

IMS 2018 Publication

Efficiency Degradation in Wideband Power Amplifiers

Luís C. Nunes, Diogo R. Barros, Pedro M. Cabral and José C. Pedro

DETI, Instituto de Telecomunicações, Universidade de Aveiro

Campus Universitário de Santiago, 3810-193 Aveiro, Portugal

Abstract—**This paper addresses the efficiency degradation observed in wideband power amplifiers. It starts by presenting a detailed explanation that relates this observed performance degradation with the terminations at baseband. Then, a comparison between two implemented power amplifiers with the same fundamental and harmonic terminations, but with different baseband networks is presented, showing that an optimized bias network design can improve the observed efficiency degradation.**

Index Terms— **Baseband Terminations, Instantaneous Bandwidth, Power amplifiers, Video Bandwidth, Wideband.**

I. INTRODUCTION

The constant increase of data rates has consistently pushed the boundaries of radiofrequency (RF) power amplifiers' (PAs) bandwidth requirements. Besides that, PAs must be able to operate in a wideband multicarrier/concurrent bands scenario, while maintaining the high efficiency values throughout the complete frequency range.

It is known that the average efficiency of a PA excited with an amplitude modulated signal is lower than the maximum efficiency observed under CW excitation and depends on the signal's probability density function. For instance, for a class B PA, excited with a two-tone signal, it can be theoretically demonstrated that the average efficiency decreases by a factor of π/4, when compared with the CW excitation maximum efficiency, which is, itself, also π/4.

However, although the PA output matching network (OMN) can be designed and optimized to present the required intrinsic impedances to the device over a determined bandwidth (thus showing a flat CW response on both output power and efficiency), real multiband/concurrent bands PA implementations present efficiencies further degraded beyond the theoretical difference between the modulated and CW signals [1]-[3]. Indeed, [4] reported a significant efficiency degradation under distinct baseband conditions, obtained with an envelope load-pull measurement system, and [5] mentioned that resonances at the baseband should be avoided in order to increase PA performance. Unfortunately, the underlying efficiency degradation mechanism is yet to be explained.

The aim of this work is to provide a detailed and comprehensive description of the mechanism that is behind such efficiency degradation in PAs under wideband excitations. Analytical (only outlined in this manuscript summary) and simulated studies showed that this efficiency degradation can be traced back to the baseband terminations presented to the active device, a theory then validated with measurements taken from two 100 W GaN PAs.

II. IMPACT OF THE BASEBAND IMPEDANCE ON EFFICIENCY

The explanation is based on the conceptual PA presented in Fig. 1, composed by a piece-wise current source, terminated with the optimum fundamental and harmonic loads. The bias network is only composed by an inductor, L, and two ideal filters, H_0 and H_1, were used so that the bias network does not affect the fundamental and harmonic impedances.
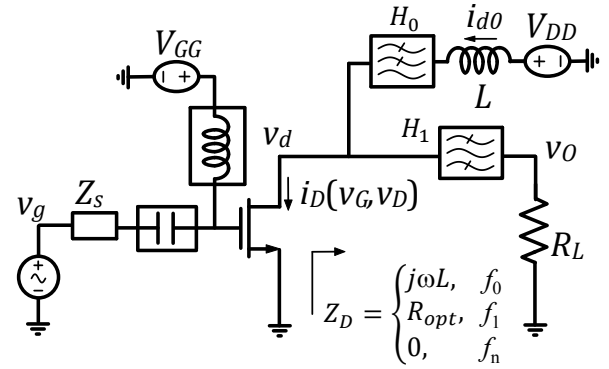

Fig. 1. Schematic of the conceptual PA used to explain the efficiency degradation observed due to the baseband terminations.

The harmonic-balance simulated load trajectories and baseband drain voltage component (v_{d0}) are shown in Fig. 2, for two different cases: ideal bias-tee (i.e 0 nH inductor) and 45 nH inductor, when the PA is excited with a two-tone signal (100 MHz frequency separation).
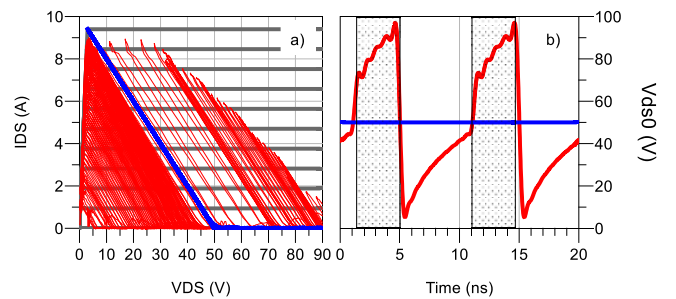

Fig. 2. (a) Load trajectories and (b) baseband voltage component of the conceptual power amplifier.

As it is possible to see, there is a modulation of v_{d0} caused by the inductor, which can be described by (1), where i_{d0} is the baseband drain current.

$$v_{d0}(\tau) = V_{DD} - L\frac{di_{d0}(\tau)}{d\tau} \qquad (1)$$

Since the drain voltage cannot decrease below zero, the device operates, in some RF cycles, limited in voltage while, in others, as a normal current source but with a higher drain voltage than it would be expected. In Fig. 2(b) and in the following figures, the zones where the device operates in current mode are represented with dark rectangles, while the others correspond to the limited voltage operation mode.

When i_{d0} decreases, its derivative is negative, consequently, v_{d0} increases and the device operates in current mode. In this case, the current only depends on the gate-to-source voltage, and so, the fundamental and the baseband current waveforms are equal to the ones obtained when $L = 0$ nH, as shown in Fig. 3. This being the case, the output and supply powers are also the same as is, consequently, the instantaneous efficiency. The power and efficiency waveforms, for this case (current mode operation), are shown in the shaded part of Fig. 4.
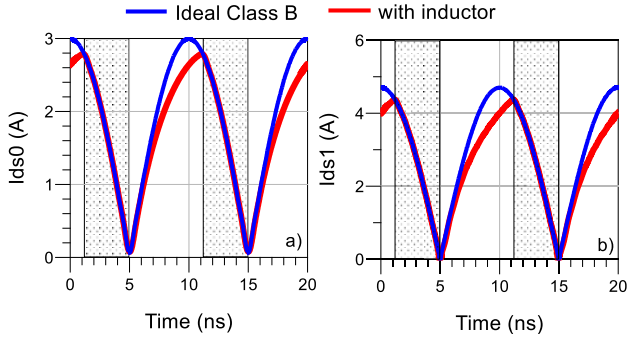

Fig. 3. (a) Baseband and (b) fundamental drain current waveforms.

The problem arises when the device operates in the limited voltage-mode, i.e. when the i_{d0} derivative is positive, v_{d0} decreases and the dynamic load-line reaches the triode region. In this case, since i_{d0} is limited by the voltage excursion, it will be lower than in the current operation mode without any inductor, as shown in Fig. 3(a). Consequently, the absorbed dc power is also lower than the one obtained when the PA does not have any inductor (Fig. 4(a)).

This could lead us to think that the efficiency increases due to the absorbed power reduction. However, since the fundamental current, i_{d1}, also decreases (in the same proportion as i_{d0}, only scaled by a $2/\pi$ factor, as shown in Fig. 3(b)) and, since the output power depends quadratically on the fundamental current, the reduction of the fundamental output power will be higher than the one in the absorbed power (Fig. 4(b)), imposing an efficiency degradation in this zone, as shown in Fig. 4(c).

Please note that the observed efficiency degradation can increase either for higher baseband impedances or for higher baseband current derivative. This means that whenever the envelope current amplitude or frequency separation increase, we should expect higher performance degradation.
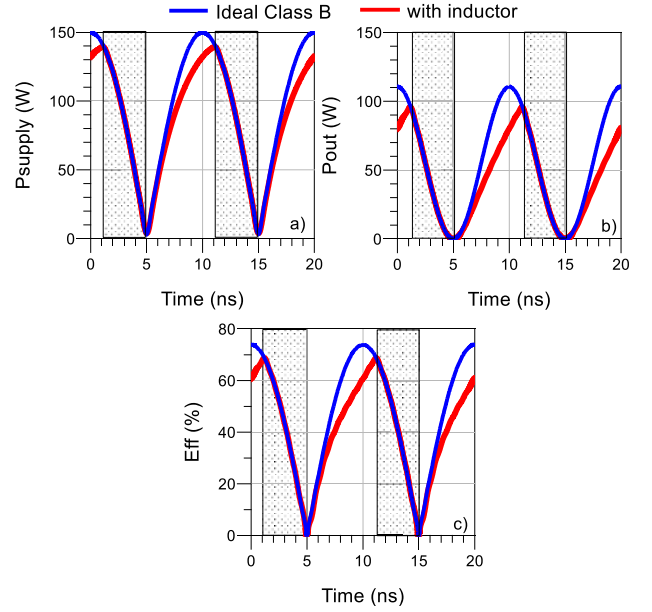

Fig. 4. Instantaneous waveforms of the (a) absorbed dc power, (b) output power and (c) efficiency waveforms.

III. EXPERIMENTAL RESULTS

In a conventional power amplifier design, to avoid interaction between the bias and output matching networks, a very high inductance or a quarter-wavelength line with a high characteristic impedance, are normally used, making PA design easier. Unfortunately, in a scenario where wider instantaneous bandwidths are required, this approach imposes a very high baseband impedance and, as explained in the previous section, this will lead to an average efficiency degradation.
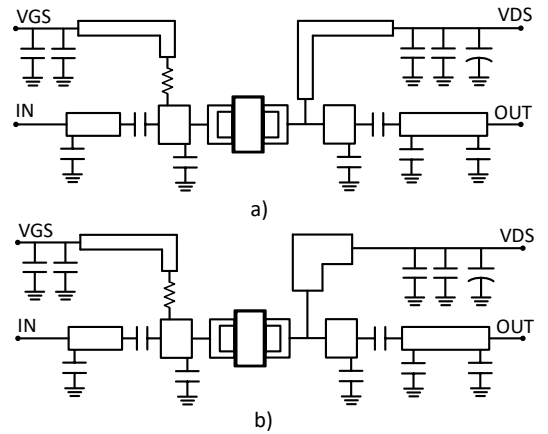

Fig. 5. Block diagram of the implemented PAs: a) where the bias network was implemented with the conventional quarter-wave length transmission line (PA-I) and b) where the bias network was optimized (PA-II).

In order to experimentally observe this bias termination impact on the PA efficiency performance, we designed and implemented two power amplifiers based on 100 W GaN devic-

es, shown in Fig. 5, where their input and output matching networks were designed to present the optimum fundamental and harmonic impedances between 1.8 GHz and 2.2 GHz.

On what the bias networks are concerned, in one amplifier (which, from now on, we will call PA-I) a conventional quarter-wavelength line was used. For the other amplifier (PA-II) the bias network was optimized so that the baseband impedance absolute value is lower than the fundamental one over a 400 MHz bandwidth. Please note that, since PA-II bias and output matching networks are not completely separated, they had to be optimized at the same time. A comparison between the simulated absolute values of these impedances is shown in Fig. 6.
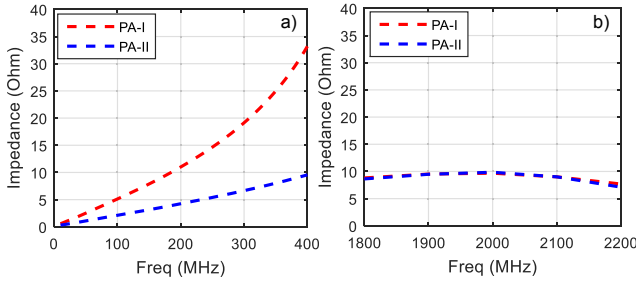

Fig. 6. Amplitude of the simulated intrinsic a) baseband and b) fundamental load termination for the implemented PAs with and without an optimized bias network.

The measured and simulated CW efficiency and output power are reasonably flat within the desired bandwidth, as it is possible to see in Fig. 7, only a variation at 1800 MHz is observed in the implemented PA-I. The slightly lower efficiency observed in PA-I can be due to the difficulty of having exactly the same harmonic terminations in both implemented PAs. However, this does not affect our analysis since we are looking for the efficiency degradation profile and not for its absolute value.

Finally, Fig. 8 shows the measured and simulated average efficiency of the two PAs when excited with two-tone signals for different frequency separations, Δf, centered at 2 GHz. These measurements and simulations of both PAs were obtained with a pre-equalization, so that the output tones have the same transmitted power, a procedure normally used in real operation. As expected, when Δf is small, neither PA presents any efficiency degradation but, when Δf increases the PA with an optimized bias network presents much less degradation than the other, proving that the baseband termination is, indeed, the main reason for the observed efficiency degradation.

The higher efficiency degradation observed in PA-I measurements, for the 400 MHz frequency separation, in comparison with the simulation results, can be attributed to the non-flat CW characteristic observed at 1.8 GHz (Fig. 7).
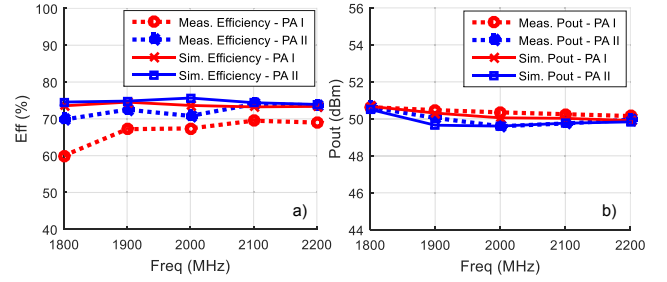

Fig. 7. Measured and simulated CW a) efficiency and b) output power at the 3dB gain compression point over the bandwidth for the implemented PAs.
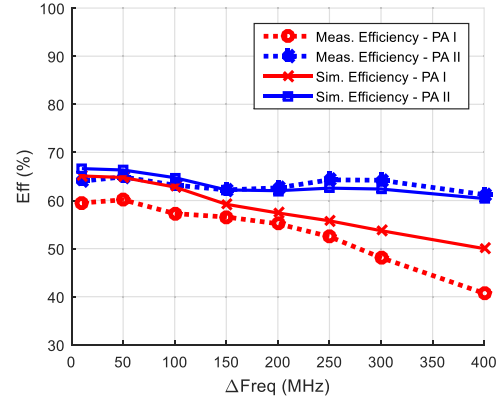

Fig. 8. Measured and simulated average efficiency versus two-tone frequency separation, Δf, for the implemented PAs excited with two-tone signals of 2 GHz center frequency.

IV. CONCLUSION

This work provided a theoretical explanation for the observed efficiency degradation observed in wideband PAs. The baseband terminations along with the baseband drain voltage modulation were found to be the main mechanisms responsible for this efficiency degradation. This was experimentally validated, showing that a PA with an optimized bias network presents less efficiency degradation than a PA without an optimized bias network.

REFERENCES

[1] J. Xia, X. Zhu, L. Zhang, J. Zhai and Y. Sun, "High-Efficiency GaN Doherty Power Amplifier for 100-MHz LTE-Advanced Application Based on Modified Load Modulation Network," *IEEE Trans. Microw. Theory Techn.*, vol. 61, no. 8, pp. 2911-2921, Aug. 2013.

[2] Q. Cheng, H. Fu, S. Zhu and J. Ma, "Two-Stage High-Efficiency Concurrent Dual-Band Harmonic-Tuned Power Amplifier," *IEEE Tran. Microw. Theory Techn.*, vol. 64, no. 10, pp. 3232-3243, Oct. 2016.

[3] P. Saad, P. Colantonio, L. Piazzon, K. Andersson and C. Fager, "Design of a Concurrent Dual-Band 1.8-2.4-GHz GaN HEMT Doherty Power Amplifier," *IEEE Trans. Microw. Theory Techn.*, vol. 60, no. 6, pp. 1840-1849, June 2012.

[4] B. Bunz, A. Ahmed and G. Kompa, "Influence of envelope impedance termination on RF behaviour of GaN HEMT power devices," *European Gallium Arsenide and Other Semiconductor Application Symposium*, GAAS 2005, Paris, 2005, pp. 649-652.

[5] C. Ma, W. Pan, S. Shao, C. Qing and Y. Tang, "A Wideband Doherty Power Amplifier with 100 MHz Instantaneous Bandwidth for LTE-Advanced Applications," *IEEE Microw. Wireless Compon. Lett.*, vol. 23, no. 11, pp. 614-616, Nov. 2013.

Appendix B

TMTT 2018 Publication

Efficiency Degradation Analysis in Wideband Power Amplifiers

Luís Cótimos Nunes, *Member, IEEE*, Diogo R. Barros, *Student Member, IEEE*,
Pedro M. Cabral, *Senior Member, IEEE*, and José C. Pedro, *Fellow, IEEE*

Abstract— This paper addresses the mechanisms of wideband power amplifiers' efficiency degradation in comparison with their narrowband operation. It starts by identifying some possible causes for this performance degradation, showing that the baseband terminations are dominant. A detailed explanation for the efficiency degradation is then presented, considering the scenarios where the most important baseband components fall before or after the resonance imposed by the bias and matching networks. A theoretical model that is able to describe this performance degradation is also presented. Finally, the proposed theory is validated through two implemented power amplifiers with the same fundamental and harmonic terminations, but with different baseband networks, showing that an optimized bias network design can improve the efficiency performance of a PA.

Index Terms— Baseband terminations, instantaneous bandwidth, power amplifiers (PA), video bandwidth (VBW), wideband.

I. INTRODUCTION

IN WIRELESS communications, the constant increase of data rates has consistently pushed the boundaries of radio frequency (RF) power amplifiers' (PAs) bandwidth requirements. Besides that, PAs must be able to operate in a wideband multicarrier/concurrent band scenario, while maintaining the high efficiency values throughout the complete frequency range.

It is known that the average efficiency of a PA, excited with an amplitude modulated signal, is lower than the maximum efficiency observed under continuous wave (CW) excitation and depends on the signal's probability density function (PDF) [1], [2]. However, although the PA output matching network (OMN) can be designed and optimized to present the required intrinsic impedances to the device over a determined bandwidth (showing a flat CW response on both output power and efficiency characteristics) [3]–[7], concurrent band PA implementations present efficiencies further degraded

The authors are with the Departamento de Electrónica, Telecomunicações e Informática, Instituto de Telecomunicações, Universidade de Aveiro, Campus Universitário de Santiago, 3810-193 Aveiro, Portugal (e-mail: cotimos@ua.pt; diogo.rafael@ua.pt; pcabral@ua.pt; jcpedro@ua.pt).

beyond the theoretical difference between the modulated and CW signals [8]–[10].

In the PA design realm, it is known that one possible cause for this performance degradation is the baseband termination presented to the active device, which is responsible for imposing the so-called PA video bandwidth (VBW) [11]–[15]. Indeed, Bunz *et al.* [16] reported a significant efficiency degradation under distinct baseband conditions, obtained with an envelope load-pull measurement system and Ma *et al.* [17] mentioned that resonances at the baseband should be avoided in order to increase the PA performance. Actually, this issue is so important that manufacturers are also improving the VBW of their devices by using integrated bias networks [12], [13], [18]. Other works have also related the baseband terminations with linearity degradation observed when the PA is excited with two-tone signals [19]–[21]. Unfortunately, the underlying efficiency degradation mechanisms are yet to be explained.

In a wideband multicarrier/concurrent band scenario, the matching and bias networks can impose resonances at these frequencies, being possible to obtain both inductive and capacitive impedances at the baseband frequency components. Recently, Nunes *et al.* [22] presented a qualitative explanation that relates this efficiency degradation with the baseband terminations restricted to the case where the baseband impedances are inductive.

Thus, the aim of this paper is to provide a detailed description of the mechanism that is behind such efficiency degradation in PAs under wideband excitations, considering both scenarios (before and after the resonance) and presenting an analytical model able to describe and predict this performance degradation.

For that, this paper is organized as follows. Section II is devoted to the identification of the main efficiency degradation mechanisms in wideband PAs, showing that the baseband impedance has a preponderant role in that degradation. Section III explains the impact of the baseband impedances on the efficiency degradation, for both the inductive and capacitive cases, i.e., before and after the resonance, presenting a theoretical model that is useful to further understand the performance degradation due to the bias impedance terminations. Section IV validates the presented theory through a comparison between measurements and simulations of the efficiency for different two-tone frequency separations. Finally, Section V closes this paper by summarizing its most relevant conclusions.

II. EFFICIENCY DEGRADATION MECHANISMS

The theoretical maximum drain efficiency under a CW excitation for an ideal class B PA is given by

$$\eta = \frac{P_{o,\max}}{P_{DC,\max}} = \frac{\pi}{4}\frac{(V_{DD} - V_k)}{V_{DD}} \tag{1}$$

in which V_{DD} is the supply voltage and V_k is the knee voltage of the drain-to-source current. However, when the PA is excited with a modulated signal, the theoretical average efficiency will be lower due to the signal's PDF.

To illustrate this, let us consider a class B PA, excited with a two-tone signal whose amplitude is capable to fully excite the PA, i.e., producing a maximum voltage and current excursions of $V_{DD} - V_k$ and $I_{\max}/2$, respectively. In this scenario, the output and dc average powers can be obtained according to the following equations, respectively,

$$P_{out,av} = \frac{1}{T}\int_{-\frac{T}{2}}^{\frac{T}{2}}\frac{1}{2}v_{d1}(\tau)i_{d1}(\tau)d\tau = \frac{(V_{DD} - V_k)I_{\max}}{8} \tag{2}$$

$$P_{dc,av} = \frac{1}{T}\int_{-\frac{T}{2}}^{\frac{T}{2}}v_{d0}(\tau)i_{d0}(\tau)d\tau = \frac{2}{\pi^2}V_{DD}I_{\max} \tag{3}$$

where v_{d1} and i_{d1} are the fundamental voltage and current envelopes and v_{d0} and i_{d0} are the baseband envelope components. This leads to an average efficiency given by (4). Thus, the theoretical average efficiency of an ideal class B PA excited with a two-tone signal decreases by a factor of $\pi/4$, when compared with the maximum efficiency obtained under CW excitation, which is also $\pi/4$ as shown in (1)

$$\eta_{av} = \frac{P_{o,av}}{P_{dc,av}} = \frac{\pi^2}{16}\frac{(V_{DD} - V_k)}{V_{DD}}. \tag{4}$$

Unfortunately, despite the PA designers' efforts to guarantee a flat CW response on both efficiency and output power, practical wideband PA implementations present further efficiency degradations beyond this theoretical difference [8]–[10].

Several possible causes for the efficiency degradation beyond the expected theoretical difference can be advanced. The most obvious reason is the nonflatness of the CW characteristics. This can be caused either by nonoptimum fundamental impedances or due to variation of the harmonic terminations within the considered bandwidth. For instance, when the PA is excited with a dual-band signal and the frequency separation of the bands is increasing, if the PA presents a maximum average efficiency at the center frequency, it is normal to observe an efficiency degradation when the bandwidth increases. However, since the PA design methodologies are based on CW optimization, this issue can be observed during the design phase, and so can be corrected by appropriate matching networks design.

The problem addressed in this paper is the observed efficiency degradation even if the CW responses on both efficiency and output power are flat over the desired bandwidth. For this efficiency degradation problem, we can highlight two possible causes: 1) the nonoptimal impedances at the intermodulation distortion (IMD) components and 2) the baseband terminations imposed by the bias network (which defines the so-called VBW).
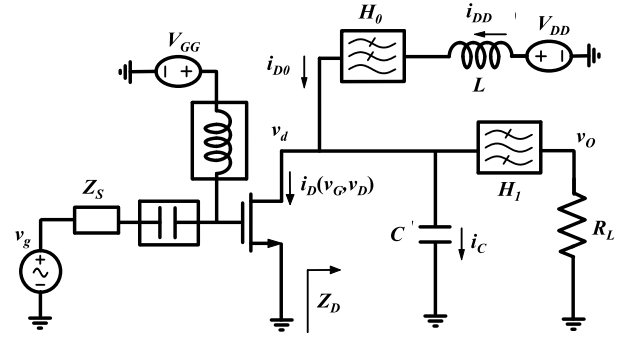

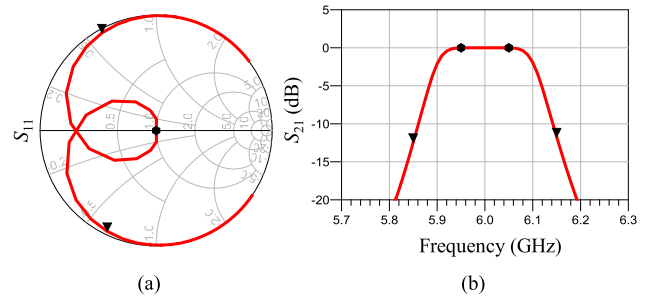Fig. 1. Schematic of the conceptual PA used to explain the efficiency degradation mechanisms.

Fig. 2. Filter response used to analyze the impact of the nonoptimal impedances at IMD frequencies. (a) Reflection coefficient (S_{11}) and (b) transmission coefficient (S_{21}). The triangle markers are the IMD3 distortion bands, and the circle markers are the fundamental bands.

To observe the impact of these efficiency-degradation mechanisms, let us consider the conceptual PA presented in Fig. 1, whose active device is described by a piecewise linear current source. Two ideal filters H_0 and H_1 were used to guarantee that the bias network does not affect the fundamental and harmonic impedances, so that we could independently analyze these two efficiency degradation mechanisms. The bias network is only composed by an inductor L that is used to control the impedance presented to the active device at the baseband, and capacitor C that represents the total capacitance seen from the drain terminal to ground. This is typically composed by the transistor's drain-to-source capacitance C_{ds} and the output series dc blocking capacitor. In this section, capacitor C is considered equal to zero.

A. Impact of the IMD Terminations

Since the PA is normally designed considering only the signal bandwidth, the out-of-band impedances presented to the active device, and imposed by the matching networks, can be far away from the optimal ones. Thus, when the PA is excited with a wideband signal and the input power is sufficiently high to generate out-of-band components, some efficiency variation is expected due to the nonoptimal impedances at these frequency regions.

To observe the impact of the IMD components' terminations on efficiency, we excited the PA with a two-tone signal of 100-MHz frequency separation and, instead of using a constant optimal class B impedance R_L as represented in Fig. 1, we added an output filter with the frequency response shown in Fig. 2. At fundamental bands, the impedance is kept
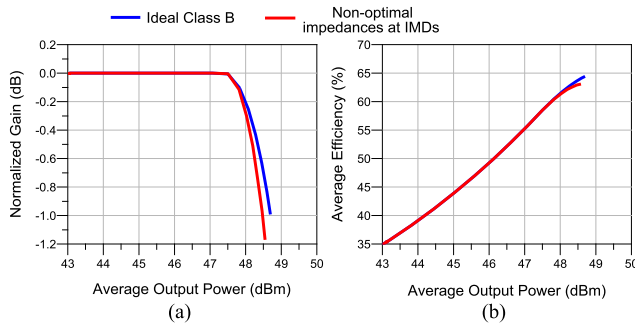
Fig. 3.   Simulated (a) normalized gain and (b) average efficiency versus average output power profiles for the ideal class B PA and for the PA with a filter that imposes nonoptimal impedances at IMD components.
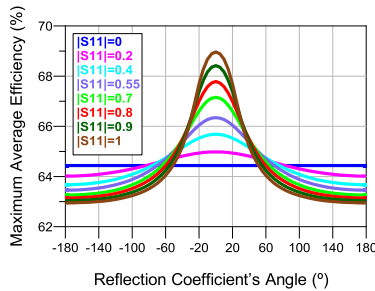

Fig. 4.   Average efficiency at the 1-dB compression point for different reflection coefficients at IMD3 components.

constant and equal to the optimal one but at the out-of-band frequencies, the impedances presented to the active device change according to Fig. 2(a). The bias network inductor and capacitor were set to zero so that the baseband impedance presented to the active device is also zero.

Fig. 3 shows the obtained simulation results of the normalized gain and average efficiency profiles for an ideal class B PA and for the one modified with the filter shown in Fig. 2. For low-input power levels, no out-of-band components are generated and, since the impedances presented to the active devices (of both PAs) at the fundamental frequency region are the same, their gain and average efficiency profiles are coincident. However, when the input power is high enough to force the active device to operate in the triode region, the PAs will compress and out-of-band components will be generated, producing small efficiency and output power degradations of 1.5% and 0.2 dB, respectively. Please note that both PAs are excited up to the same input power level that we would use to obtain the 1-dB compression point in an ideal class B PA (i.e., PA terminated with the ideal class B impedances).

To generalize the study of the IMD3 termination impact on efficiency, we performed a load-pull analysis at this frequency, in which the impedances at the fundamental bands are fixed and equal to the optimum ones. In order to make this study more reasonable, we considered that the upper IMD3 termination is always the complex conjugate of the lower IMD3 termination. Although some of the tested impedances are very complicated to achieve with the common OMNs, this test illustrates the efficiency sensitivity to the IMD3 terminations. The obtained average efficiencies at the 1-dB compression point for different IMD3 terminations are shown in Fig. 4.
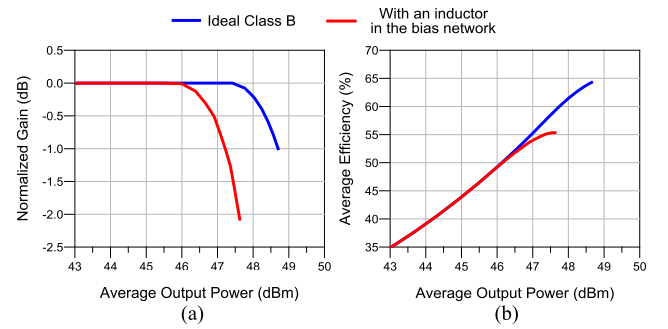

Fig. 5.   Simulated (a) normalized gain and (b) average efficiency versus average output power profiles for the ideal class B PA and for the PA with a 35-nH inductor in the bias network.

Naturally, when the reflection coefficient amplitude is very small (i.e., closer to the optimum class B impedance), the obtained efficiency tends to the one achieved with an ideal class B PA. However, when $|S_{11}|$ tends to unity (i.e., closer to the edge of the Smith chart), an efficiency variation is observed for different S_{11} phases. For small impedances (S_{11} phases close to $-180°$), we observe a maximum efficiency degradation of 1.5% with respect to the value obtained in an ideal Class B and, for higher impedances, an efficiency improvement about 5% is observed.

Therefore, not only the efficiency degradation that we can obtain with nonoptimal class B terminations is small, as we can also observe an improvement with respect to the conventional class B PA. Thus, this mechanism cannot be used to justify the significant efficiency degradations that have been observed in common wideband/concurrent band PA implementations.

B. Impact of the Baseband Terminations

To analyze the impact of the baseband terminations, the optimum class B load R_L was restored, obtaining the desired CW flat response over the entire bandwidth (including the most important IMD products). On what the bias network is concerned, an inductor was selected so that the active device could see inductive impedance at the first baseband component (100 MHz) equal to the double of the fundamental load magnitude. The capacitor was kept equal to zero.

The PA was driven with the same input power level as considered in the IMD termination study previously presented. The obtained normalized gain and average efficiency predictions versus output power are shown in Fig. 5. The PA with the bias inductor compresses earlier, resulting in an average efficiency and output power degradation of 10% and 1 dB, respectively.

Similar to what was performed before for the IMD terminations' impact, we also performed a load-pull analysis, but now at the first baseband component, considering the optimum class B impedances for the other frequencies. During this test, the input power level was fixed to the one that we would use to obtain the 1-dB compression point in an ideal class B PA.

The obtained average efficiencies for different baseband terminations are shown in Fig. 6. As expected, the average efficiency is maximum (and equal to the one obtained
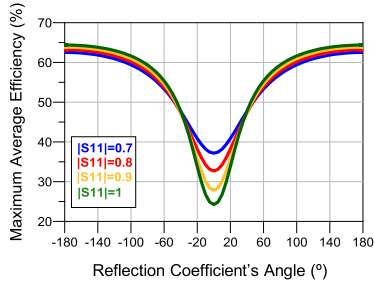
Fig. 6. Average efficiency at the 1-dB compression point for different reflection coefficients at the first baseband component.

(a)   (b)

Fig. 7. Illustration of (a) impedance profile and the respective (b) reflection coefficient presented to the i_{DS} current source in a presence of a resonance at baseband.

(a)   (b)

Fig. 8. Simulated (a) impedance profile and the respective (b) reflection coefficient presented to the i_{DS} current source when $L = 45$ nH.

(a)   (b)

Fig. 9. Simulated (a) dynamic load-line and (b) baseband voltage component of the conceptual PA presented in Fig. 1 when $L = 0$ and 45 nH.

in a class B PA) when short circuit is presented to the active device at the baseband. For higher impedances, we can observe a severe efficiency degradation that can be as high as 40%. Another interesting point worth mentioning is that, after the highest impedance value, i.e., when the active device already sees a capacitive impedance, the efficiency starts to recover from this severe degradation.

Looking into Figs. 3 and 5 or into Figs. 4 and 6, we can conclude that nonoptimal baseband terminations can impose an efficiency degradation much higher than the ones obtained for nonoptimal IMD terminations. Moreover, the efficiency degradation due to nonoptimal IMD terminations is only observed when the PA is overdriven, whereas the PA with nonoptimal baseband terminations presents an earlier compression with its inherent efficiency degradation. Thus, we can conclude that the main contributor to the efficiency degradation observed in a PA under wideband excitation is the baseband termination.

III. EFFICIENCY DEGRADATION DUE TO THE BASEBAND IMPEDANCES

In order to avoid any interaction between baseband and RF frequency regions, in conventional PA designs, a very high inductance, or a quarter-wavelength line with a high characteristic impedance (terminated with an RF decoupling capacitor), is normally used to feed the transistor drain with the necessary dc voltage. Then, an OMN, with the necessary dc block capacitor, is added, so that the device can see the desired impedances at fundamental and harmonic frequencies. Unfortunately, with this approach, some resonances can appear at baseband (as the one illustrated in Fig. 7), especially in a scenario where wider instantaneous bandwidth is required.

Looking into the impedance profile illustrated in Fig. 7, we can highlight three distinct scenarios that can occur when the PA is excited with a wideband signal. When the most important baseband components fall before the resonance, the impedances presented to the device at these frequencies will be inductive. Another possible scenario is when the most important baseband component falls at the resonance, where a very high real impedance is presented to the device. Finally, another scenario is faced whenever the most important baseband components fall above the resonance. This means that the impedances presented to the device at these frequencies become capacitive. These three scenarios can produce distinct behaviors and, therefore, need to be analyzed separately.
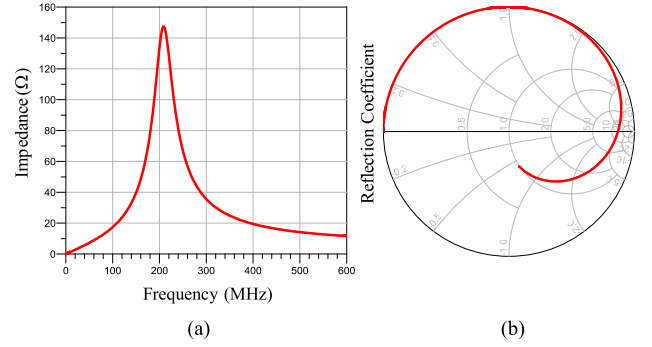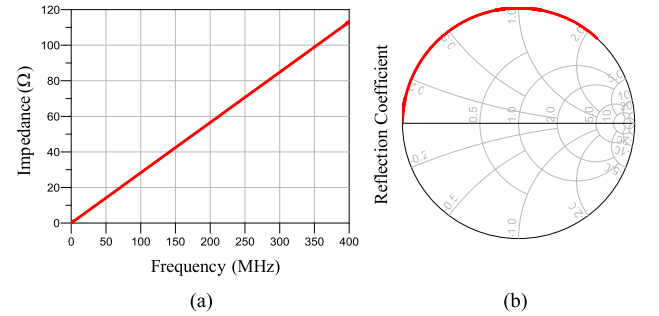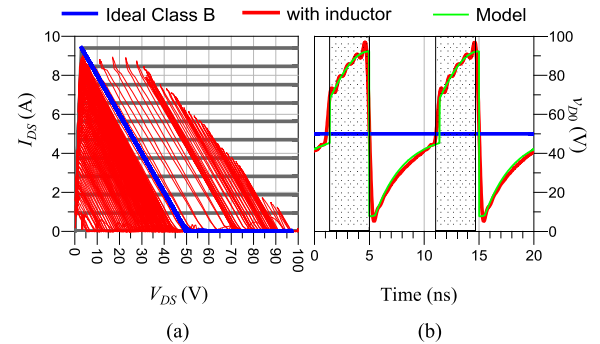
A. Inductive Baseband Impedances

For this analysis, we considered the conceptual PA presented in Fig. 1, where the bias network is only composed by inductor L and so, no resonance is observed in this conceptual PA. Two ideal filters (H_0 and H_1) were used to guarantee that this inductor does not affect the CW flat response.

For illustration purposes, two different cases will be considered throughout this analysis: ideal bias-tee (i.e., 0-nH inductor) and 45-nH inductor. Fig. 8 represents the baseband impedance profile obtained for this last inductor case. The simulated dynamic load-line trajectories and baseband drain voltage component (v_{d0}) for the two cases are shown in Fig. 9, when the PA is excited with a two-tone signal (100-MHz frequency separation).

As it is possible to see, there is a modulation of v_{d0} caused by the inductor, which can be described by the following

equation, where i_{d0} is the baseband drain current:

$$v_{d0}(\tau) = V_{DD} - L\frac{di_{d0}(\tau)}{d\tau}. \tag{5}$$

Since the drain voltage cannot decrease below zero, the device operates, in some RF cycles, limited in voltage, while in others, as a normal current source but with a higher drain voltage than it would be expected. In Fig. 9(b) and in the following ones, the light gray shaded zones correspond to current mode device operation.

The RF cycles in the envelope period in which the device operates as a normal current source occur whenever the following condition is verified:

$$|i_{d1}(\tau)| \leq \frac{v_{d0}(\tau)}{R_L + 2R_{on}} \tag{6}$$

where $R_L = R_{opt}$ is the fundamental optimum impedance and R_{on} is the triode region ON-resistance. In other words, the device operates in a current mode if the voltage excursion is lower than $v_{d0}(\tau)$. In this case, the baseband and fundamental currents are given by

$$i_{d0}(\tau) = \frac{I_p}{\pi}|\cos(\omega_s\tau)| \tag{7}$$

$$i_{d1}(\tau) = -\frac{I_p}{2}\cos(\omega_s\tau) \tag{8}$$

in which I_p is equal to $g_m v_{gs}$, being g_m the device transconductance. The correspondent envelope-varying output and dc absorbed powers will be given by

$$P_{out}(\tau) = \frac{1}{2}R_L i_{d1}^2(\tau) \tag{9}$$

$$P_{supply}(\tau) = V_{DD}i_{d0}(\tau) \tag{10}$$

which results in the following instantaneous efficiency:

$$\eta(\tau) = \frac{\pi}{4}\frac{V_{DD} - R_{on}I_p}{V_{DD}}|\cos(\tau)|. \tag{11}$$

Although it is not necessary to compute $v_{d0}(\tau)$ to obtain the instantaneous efficiency (since the device operates as a current source), we can calculate it by substituting (7) into (5)

$$v_{d0}(\tau) = V_{DD} + L\omega_s\frac{I_p}{\pi}\sin(\omega_s\tau)\text{sign}(\tau) \tag{12}$$

in which sign (τ) is the sign of the function $\cos(\omega_s\tau)$.

From a qualitative point of view, when i_{d0} decreases, its derivative is negative; consequently, v_{d0} increases and the device operates in current mode. In this case, the current depends only on the gate-to-source voltage v_{GS} and so, the fundamental and the baseband current waveforms are equal to the ones obtained when $L = 0$ nH, as shown in Fig. 10. Therefore, the output and supply powers are also the same, as is, consequently, the instantaneous efficiency (Fig. 11).

Due to the reduction of $v_{d0}(\tau)$, in some other RF cycles of the envelope period, condition (6) is no longer verified, and so the device starts to operate in a limited voltage mode. Under this condition, the baseband and fundamental current components can be approximated by

$$i_{d0}(\tau_v) = \frac{2}{\pi}\frac{v_{d0}(\tau_v)}{R_L + 2R_{on}} \tag{13}$$

$$i_{d1}(\tau_v) = \frac{v_{d0}(\tau_v)}{R_L + 2R_{on}} \tag{14}$$
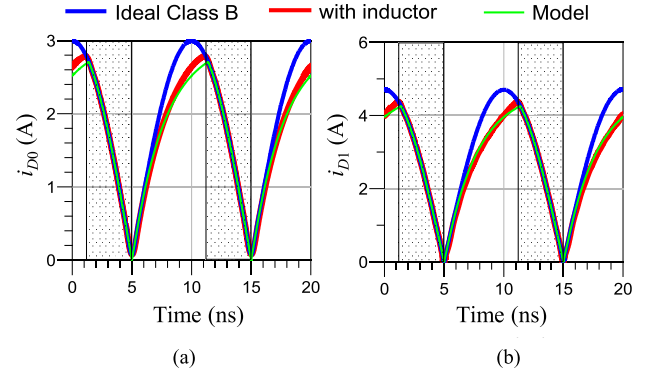

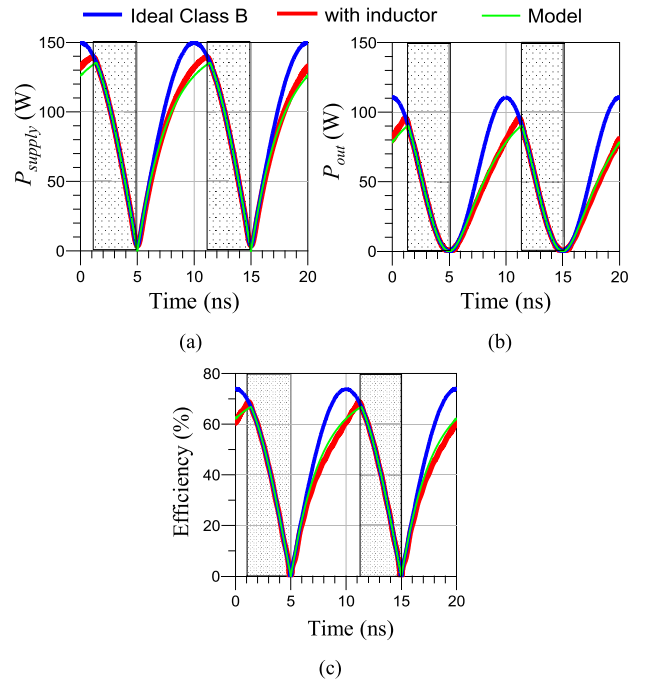Fig. 10. Simulated (a) baseband and (b) fundamental drain current waveforms.

Fig. 11. Instantaneous waveforms of the (a) absorbed dc power, (b) output power, and (c) efficiency waveforms.

where τ_v corresponds to the envelope time in which the device operates in a limited voltage mode.

Now, since the device operates in voltage mode, to compute the instantaneous efficiency we need to determine first $v_{d0}(\tau)$. For that, we can substitute (13) into (5), obtaining the following differential equation:

$$v_{d0}(\tau_v) = V_{DD} - L\frac{d}{d\tau_v}\frac{2}{\pi}\frac{v_{d0}(\tau_v)}{R_L + 2R_{on}} \tag{15}$$

which has the following solution:

$$v_{d0}(\tau_v) = V_{DD} - (V_{DD} - v_{d0}(\tau_{v0}))e^{-\frac{\pi(R_L + 2R_{on})}{2L}\tau_v}. \tag{16}$$

Please note that this transient behavior happens every time the device reaches the triode region (i.e., becomes limited in voltage). Substituting (16) into (13) and (14), the output and absorbed dc powers for the limited voltage operation mode can be derived, resulting in the instantaneous efficiency given

by the following equation:

$$\eta(\tau_v) = \frac{\pi}{4} \frac{R_L}{V_{\mathrm{DD}}} \frac{V_{\mathrm{DD}} - (V_{\mathrm{DD}} - v_{d0}(\tau_{v0}))e^{-\frac{\pi(R_L + 2R_{\mathrm{on}})}{2L}\tau_v}}{R_L + 2R_{\mathrm{on}}}. \quad (17)$$

Finally, we only need to determine when the device starts to operate in a limited voltage mode τ_0 and the respective drain bias voltage at this instant $v_{d0}(\tau_0)$. For that, we can substitute (8) and (16) into condition (6) and solve it, i.e., find the instant where the fundamental voltage excursion is equal to $v_{d0}(\tau)$. The obtained solution for τ_0 is given by

$$\tau_{v0} = \frac{2}{\omega_s} \tan^{-1}\left(\frac{\pi}{2\omega_s L}(R_L + 2R_{\mathrm{on}})\right). \quad (18)$$

Once again, from a qualitative point of view, when the device operates in the limited voltage mode, i.e., when the i_{d0} derivative is positive, v_{d0} decreases and the dynamic load-line reaches the triode region. In this case, since i_{d0} is limited by the voltage excursion, it will be lower than in the current operation mode without any inductor, as shown in Fig. 10(a). Consequently, the absorbed dc power is also lower than the one obtained when the PA does not have any inductor [Fig. 11(a)].

This could lead us to think that the efficiency increases due to the absorbed power reduction. However, since the fundamental current i_{d1} also decreases [in the same proportion as i_{d0}, only scaled by a $2/\pi$ factor, as shown in Fig. 10(b)], and since the output power depends quadratically on the fundamental current, the reduction of the fundamental output power will be higher than the one in the absorbed power [Fig. 11(b)], imposing an efficiency degradation in this zone, as shown in Fig. 11(c).

Please note that the observed efficiency degradation can increase either for higher baseband impedances or for higher baseband current derivative. This means that whenever the envelope current amplitude or frequency separation increases, we should expect higher performance degradation.

Figs. 10 and 11 show that the calculated waveforms agree with the ones obtained by simulations, proving that the derived model indeed explains the observed efficiency degradation when the impedance presented to the active device at the most important baseband components is inductive.

B. Resonance

Naturally, the worst performance degradation occurs when the resonance coincides with the most important baseband components. In this case, a dramatic efficiency degradation of around 40% can be easily observed, as shown in Fig. 6. Moreover, the PA is so much compressed that no digital predistortion system would be capable of restoring the linearity, so that the wireless communication standards spectral masks could be met. In this critical situation, PA designers must redesign the bias and the OMNs to relocate the resonance so that the most important baseband components fall either before or after it, therefore presenting an inductive or capacitive impedance behavior, respectively.

A possible mitigation of this problem consists in reducing the resonance quality factor. In this case, the most important baseband component falls in the resonance, and thus the impedance presented to the device will be lower (and real).
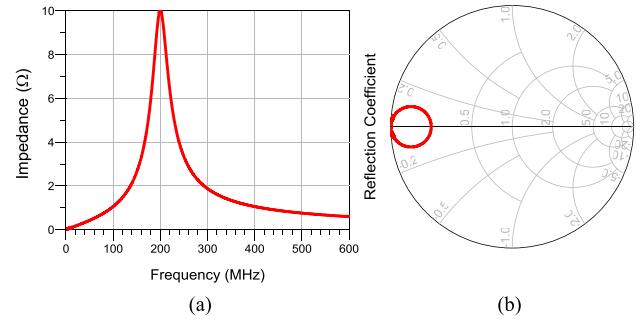

Fig. 12. Simulated (a) impedance profile and the respective (b) reflection coefficient presented to the i_{DS} current source when $L = 1.5$ nH with a parallel $R_b = 10$ Ω and $C = 0.5$ nF.
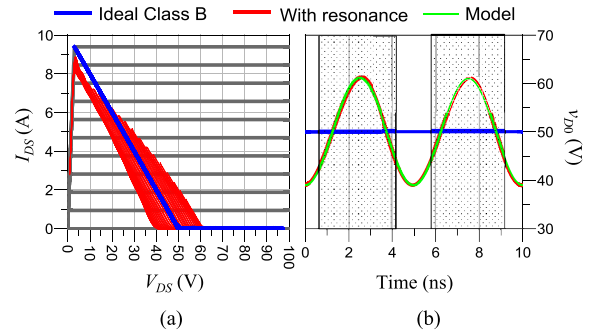

Fig. 13. Simulated (a) dynamic load line and (b) baseband voltage component.

To replicate this scenario in a simulated environment, a resistor (R_b) was added in parallel with the drain bias feed inductor shown in Fig. 1. In practice, the baseband and fundamental response would have to be consistently designed. However, in our simulated case, they can be set in an independent way. Thus, by choosing the correct capacitor value, the *RLC* circuit resonance was set exactly to the separation frequency ($\Delta f = 200$ MHz). To reduce the resonant quality factor, the resistor was set equal to the fundamental impedance (10 Ω). Fig. 12 shows the corresponding impedance profile.

Although the impedance at Δf is real and equal to 10 Ω, it is very low for the other baseband components, which results in the dynamic load-line trajectories and baseband drain voltage component (v_{d0}) presented in Fig. 13.

A load modulation of the v_{d0} can also be observed in this scenario and can be described as

$$v_{d0}(\tau) = V_{\mathrm{DD}} - R_b I_{\mathrm{BB1}} \quad (19)$$

where I_{BB1} is Δf baseband component that falls at the resonance. Similar to the inductive case, the device will operate limited in voltage during some RF cycles. However, contrary to that former case in which there was no v_{d0} voltage shift at the envelope peak (since, there, time derivative of i_{d0} is zero), in resonance, the amplifier will be further compressed and so, the approximations made in (13) and (14) are no longer valid. Instead, to mimic the compression observed in the waveforms presented in Fig. 14, we updated the fundamental and baseband current components, previously given by (7) and (8) for purely current mode operation, resulting in the following
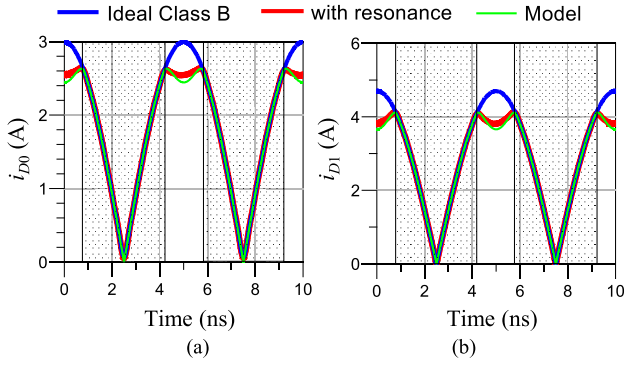
Fig. 14.   Simulated (a) baseband and (b) fundamental drain current waveforms.
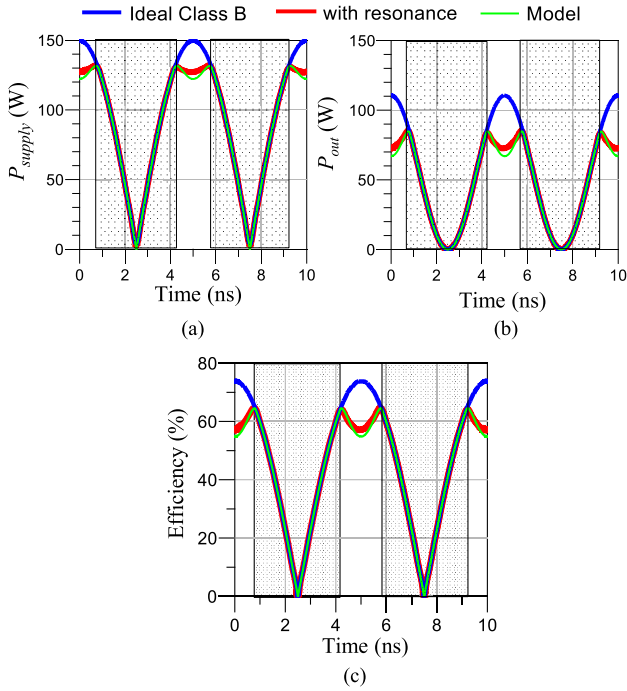

Fig. 15.   Instantaneous waveforms of the (a) absorbed dc power, (b) output power, and (c) efficiency waveforms.

equations:

$$i_{d0}(\tau) = i_{d0}\left(1 - K_0 \frac{\sin(\theta_c) - \theta_c \cos(\theta_c)}{\pi}\right) \qquad (20)$$

$$i_{d1}(\tau) = i_{d1}\left(1 - K_1 \frac{2\theta_c - \sin(2\theta_c)}{2\pi}\right) \qquad (21)$$

where $2\theta_c$ is the clipping angle (i.e., the conduction angle where the device is operated in its triode region) calculated as

$$\theta_c = \text{Re}\left\{\text{acos}\left(\frac{v_{d0}}{|i_{d1}|(R_L + 2R_{on})}\right)\right\} \qquad (22)$$

and K_0 and K_1 are amplitude factors needed to guarantee the best fit between the theoretical model and the simulations for different R_b resistances.

Similar drops in the fundamental and baseband current components are observed. However, since the output power is a quadratic function of i_{d1}, its associated reduction is higher than the one observed in the absorbed dc power, as shown in Fig. 15(a) and (b). This results in the efficiency degradation
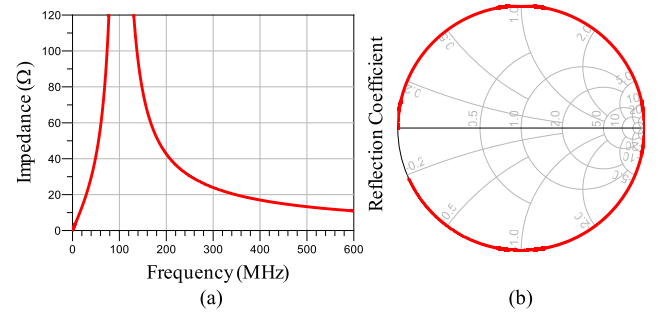

Fig. 16.   Simulated (a) impedance profile and the respective (b) reflection coefficient presented to the i_{DS} current source when $L = 100$ nH and $C = 25$ pF.
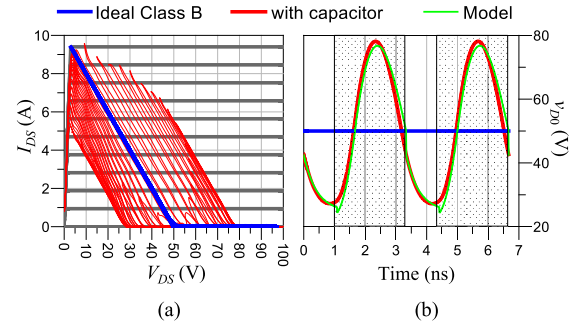

Fig. 17.   Simulated (a) dynamic load line and (b) baseband voltage component.

presented in Fig. 15(c) and described by the following equation:

$$\eta(\tau) = \frac{\pi}{4} \frac{R_L}{R_L + 2R_{on}} \frac{\left(1 - K_1 \frac{2\theta_c - \sin(2\theta_c)}{2\pi}\right)^2}{\left(1 - K_0 \frac{\sin(\theta_c) - \theta_c \cos(\theta_c)}{\pi}\right)} |\cos(\omega_s \tau)|. \quad (23)$$

Again, the good agreement between the calculated and simulated waveforms, presented in Fig. 15, shows that this simple model can indeed describe and explain this extreme case.

C. Capacitive Baseband Impedance

To analyze the case when the impedance at the baseband is capacitive, i.e., when the most important baseband components are after the resonance, let us assume that the bias network of the conceptual PA (Fig. 1) is now composed by a very large inductor (100 nH) and a shunt capacitor C (25 pF). Again, the ideal filters were used to guarantee that the bias network does not affect the CW flat response. Fig. 16 represents the baseband impedance profile obtained for this case.

Similar to what was performed in the case of inductive baseband impedances, this conceptual PA was excited with a two-tone signal (but now with a 300-MHz frequency separation). The obtained dynamic load-line trajectories and baseband drain voltage component (v_{d0}), having as reference the ones obtained for the ideal class B PA, are shown in Fig. 17. Once again, in Fig. 17(b) and in the following ones, the light gray shaded zones correspond to the current mode device operation.
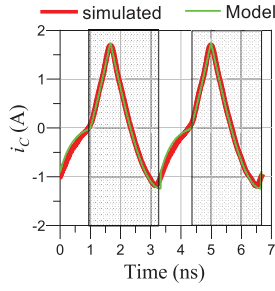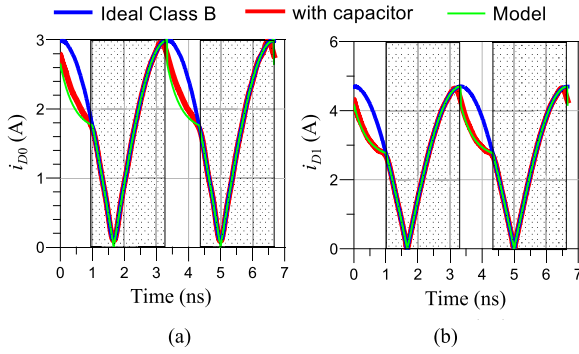
Fig. 18. Simulated waveform of the current in capacitor C.

Fig. 19. Simulated (a) baseband and (b) fundamental drain current waveforms.

Fig. 20. Instantaneous waveforms of the (a) absorbed dc power, (b) output power, and (c) efficiency waveforms.

A modulation of v_{d0} can also be observed, but now it is caused by the capacitor, which can be described as

$$v_{d0}(\tau) = \frac{1}{C} \int i_C(\tau) d\tau + K_1 \quad (24)$$

where $i_C(\tau)$ is the capacitor current and K_1 is the necessary constant to obtain V_{DD} when v_{d0} is averaged in an envelope period.

Please note that since the baseband components are well above the resonant frequency, the inductor current I_{DD} is only the dc component required by the transistor. Hence, the capacitor current is defined by the following equation, which is shown in Fig. 18:

$$i_C(\tau) = I_{\text{DD}} - i_{d0}(\tau). \quad (25)$$

Thus, at low input envelope level, i_{d0} is minimum, which leads to the maximum level of the i_C current. Then, when the i_C current is decreasing from this level, v_{d0} is always higher than V_{DD}, and the device operates in current mode.

From a qualitative point of view, when condition (6) is verified, the device operates in current mode, and so, the baseband and fundamental currents are equal to the ones obtain in a class B PA, and given by (7) and (8), respectively, as shown in Fig. 19. Thus, the powers and efficiency waveforms are also equal, and no efficiency degradation is observed in these zones, as shown in Fig. 20.

When i_C reaches its minimum, i.e., when i_{d0} reaches its maximum, v_{d0} is equal to V_{DD} and the dynamic load-line reaches the triode region. Then, when i_C changes its derivative and starts to increase, v_{d0} becomes lower and the device starts to operate limited in voltage. The device only recovers from this operation mode when the input envelope level decreases
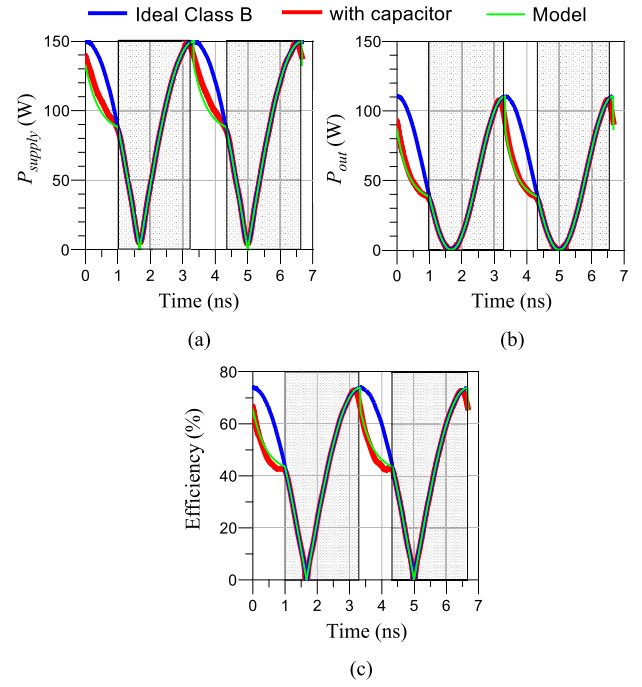
to a level in which the dynamic load line is no longer in the triode region. Therefore, contrary to what was observed for the inductive baseband impedance case, the device now operates limited in voltage when i_{d0} envelope waveform is decreasing.

In these zones, since the device operates limited in voltage, the fundamental and baseband currents are lower than the ones obtained for the ideal class B PA (Fig. 19), leading to lower output and absorbed dc powers, as shown in Fig. 20. However, since the output power depends quadratically on the fundamental current, the degradation observed in the output power is higher than the one in the absorbed dc power, producing an efficiency degradation, as shown in Fig. 20(c).

As previously mentioned, since we considered a very large inductor, $i_{\text{DD}}(\tau)$ current is only the dc component of $i_{d0}(\tau)$ required by the transistor. To calculate this dc component, we need to integrate $i_{d0}(\tau)$ over an envelope period, and for that we assume that the device operates always in the current mode

$$I_{\text{DD}} = \frac{1}{T} \int_0^T i_{d0}(\tau) d\tau = \frac{2}{\pi^2} I_p. \quad (26)$$

Please note that the error introduced by this assumption is not very significant, since this will be used only to calculate the baseband voltage when the device operates in current mode.

Consequently, substituting (26) and (7) into (25), the current in the capacitor $i_C(\tau)$ can be expressed by the following equation:

$$i_C(\tau) = \frac{2}{\pi^2} I_p - \frac{I_p}{\pi} |\cos(\omega_s \tau)|. \quad (27)$$

Using this in (24), we can calculate the voltage at the capacitor terminals (which is equal to the baseband voltage, v_{d0})

according to

$$v_{d0}(\tau) = \frac{1}{C}\left(\frac{2}{\pi^2}I_p\tau - \frac{I_p}{\pi}\frac{\sin(\omega_s\tau)}{\omega_s}\text{sign}(\tau)\right) + K_1. \quad (28)$$

To obtain constant K_1, we can use the knowledge that the average of $v_{d0}(\tau)$ over an envelope period must equal V_{DD}, which results in

$$v_{d0}(\tau) = V_{\text{DD}} + \frac{I_p}{\pi C}\left(\frac{2}{\pi}\tau - \frac{1}{\omega_s} - \frac{\sin(\omega_s\tau)}{\omega_s}\text{sign}(\tau)\right). \quad (29)$$

This is another approximation since in some RF cycles the device operates in a limited voltage mode, and so v_{d0} is not always given by (28).

For the zones where the FET operates in a limited voltage mode, the baseband and fundamental currents can also be approximated by (13) and (14), respectively. Consequently, the $i_{\text{DD}}(\tau_v)$ current becomes equal to

$$i_{\text{DD}}(\tau_v) = \frac{2}{\pi}\frac{v_{d0}(\tau_v)}{R_L + 2R_{\text{on}}} + C\frac{dv_{d0}(\tau_v)}{d\tau_v} \quad (30)$$

where τ_v again corresponds to the envelope time where the device operates in a limited voltage mode. Substituting this into (25) and (5), we can obtain the complete differential equation to determine $v_{d0}(\tau_v)$ in presence of two energy storage elements (the capacitor and the inductor)

$$v_{d0}(\tau_v) = V_{\text{DD}} - L\frac{2}{\pi}\frac{1}{R_L + 2R_{\text{on}}}\frac{dv_{d0}(\tau_v)}{d\tau_v} - LC\frac{d^2 v_{d0}(\tau_v)}{d\tau_v^2}. \quad (31)$$

However, if we consider a very large inductor, terms $v_{d0}(\tau_v)$ and V_{DD} are much lower than the other terms, and so the above differential equation can be approximated by

$$\frac{d^2 v_{d0}(\tau_v)}{d\tau_v^2} + \frac{1}{C}\frac{2}{\pi}\frac{1}{R_L + 2R_{\text{on}}}\frac{dv_{d0}(\tau_v)}{d\tau_v} = 0 \quad (32)$$

in which the solution for $v_{d0}(\tau_v)$ can be derived according to

$$v_{d0}(\tau_v) = v_{d0}(\tau_{v0}) + \frac{v_{d0}'(\tau_{v0})}{K_x}(1 - e^{-K_x\tau_v}) \quad (33)$$

where K_x is given by the following equation:

$$K_x = \frac{1}{C}\frac{2}{\pi}\frac{1}{R_L + 2R_{\text{on}}}. \quad (34)$$

As explained before, we can use condition (6) to determine the instant where the device starts to operate in a limited voltage mode τ_{v0} and the initial state variables $v_{d0}(\tau_0)$ and $v_{d0}'(\tau_0)$. To simplify the theoretical analysis, we numerically determined τ_0. $v_{d0}(\tau_0)$ and $v_{d0}'(\tau_0)$ were obtained from HB simulations.

Finally, by substituting (33) into (13) and (14), we can get the expressions for the output and absorbed dc powers during the limited voltage operation mode, resulting in the instantaneous efficiency given by

$$\eta(\tau_v) = \frac{\pi}{4}\frac{R_L}{V_{\text{DD}}}\frac{v_{d0}(\tau_{v0}) + \frac{v_{d0}'(\tau_{v0})}{K_x}(1 - e^{-K_x\tau_v})}{R_L + 2R_{\text{on}}}. \quad (35)$$

Again, the good agreement observed between the calculated waveforms and the ones obtained by simulations shown in Figs. 19 and 20 prove that the derived model
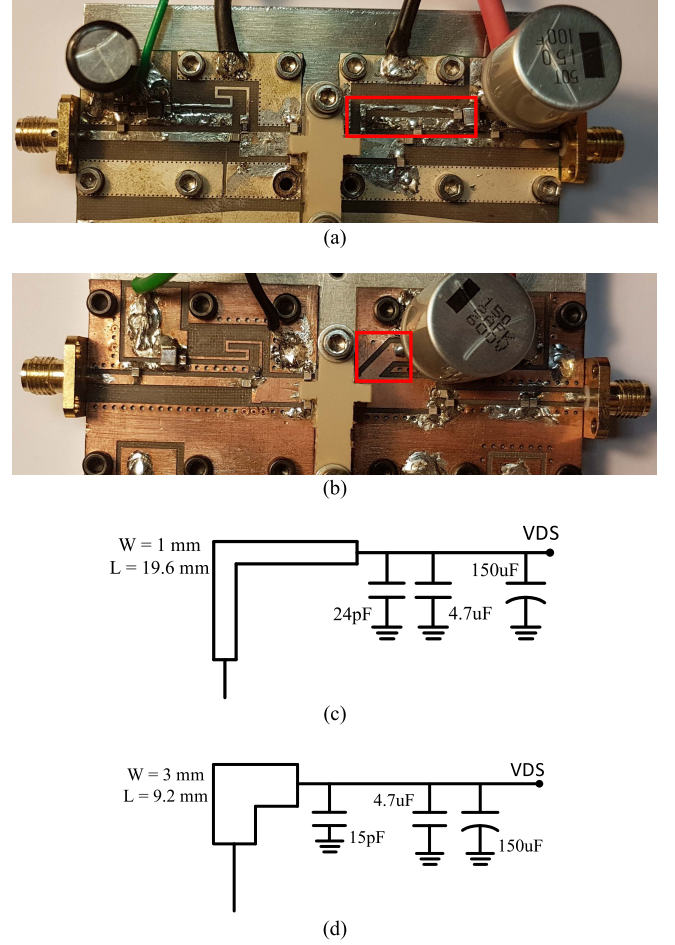

(a)

(b)

(c)

(d)

Fig. 21. Photograph of the implemented PAs: (a) where the bias network was implemented with the conventional quarter-wave length transmission line (PA-I) and (b) where the bias network was optimized (PA-II). The square in the pictures highlights the difference in the transmission line used in the bias of both PAs. Bias network schematics of (c) PA-I and (d) PA-II, implemented with Taconic TLY-5 substrate.

is indeed enough to represent and to explain the observed efficiency degradation, when the impedance presented to the active device at the most important baseband components is capacitive.

IV. EXPERIMENTAL RESULTS

In order to experimentally validate the above presented theoretical study, we designed and implemented two PAs based on 100-W GaN devices (see Fig. 21). Their input matching network and OMN were designed so that they terminate the transistor with optimum fundamental and harmonic impedances between 1.8 and 2.2 GHz.

On what the bias networks are concerned, in one amplifier (which, from now on, we will call PA-I) a conventional quarter-wavelength line was used. For the other one (PA-II), the bias network was optimized so that the absolute value of the baseband impedance is lower than the fundamental one over a 400-MHz bandwidth. Please note that since PA-II bias and OMNs are not completely separated, they had to be simultaneously optimized. Fig. 22 presents a comparison between the magnitude of these impedances obtained through simulation.
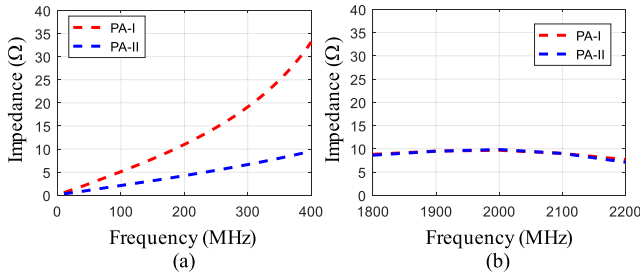
Fig. 22. Amplitude of the simulated intrinsic (a) baseband and (b) fundamental load terminations for the implemented PAs with and without an optimized bias network.
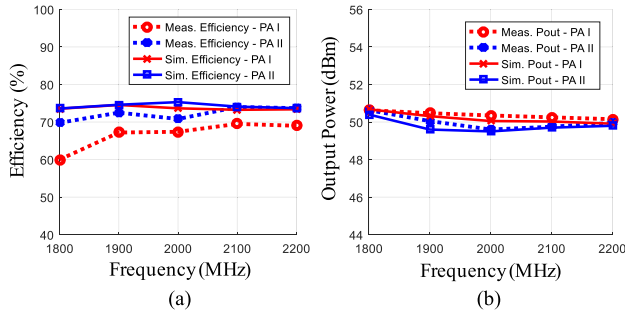

Fig. 23. Measured and simulated CW (a) efficiency and (b) output power at the 3-dB gain compression point over the bandwidth for the implemented PAs.
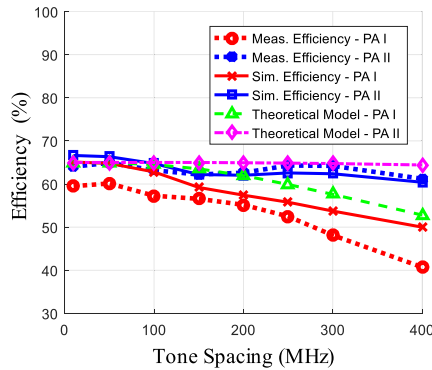

Fig. 24. Measured and simulated average efficiency versus two-tone frequency separation Δf for the implemented PAs excited with two-tone signals of 2-GHz center frequency. For comparison, the average efficiency profile predicted by our theoretical model is also shown.

The measured and simulated CW efficiency and output power are reasonably flat within the desired bandwidth. As it is possible to see in Fig. 23, only a variation at 1800 MHz is observed in PA-I implementation which latter on will be addressed. Please note that the slightly lower efficiency observed in the implemented PA-I does not affect our analysis since we are looking for the efficiency degradation profile and not for its absolute value.

Finally, Fig. 24 shows the measured and simulated average efficiencies obtained for both PAs when excited with several two-tone signals (all centered at 2 GHz, but with different separation frequencies Δf). A pre-equalization procedure was performed on both measurements and simulations in order to guarantee that, at the PA's output, both tones had the same
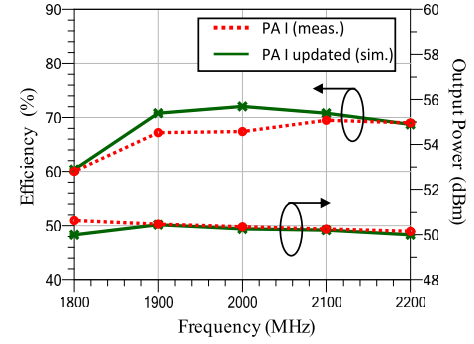

Fig. 25. Measured CW efficiency and output power at the 3-dB gain compression point over the bandwidth for the implemented PA-I in comparison with the predictions obtained with the updated version of PA-I.

power, as it is normally done in real life implementations. As expected, for small Δf, neither PA presents any efficiency degradation. But, as Δf increases, the PA with an optimized bias network (PA-II) presents far less degradation than the one with the conventional bias network design (PA-I).

To validate the theory developed in Section III, we used the derived theoretical formulation to calculate the average efficiency of both PAs, assuming that they are terminated with the optimum fundamental impedance, the 10 Ω of Fig. 22(b), and the respective harmonics to produce a flat CW response. This harmonic selection increases the theoretical class B efficiency by a factor of 1.12. Then, the baseband impedances of Fig. 22(a) were modeled by a bias inductance of 15 and 4 nH for the PA-I and PA-II, respectively. The obtained results are presented in Fig. 24, showing that the efficiency degradation obtained from the theoretical model is in agreement with the one observed in the implemented PAs.

The higher efficiency degradation observed in PA-I measurements, for the 400-MHz frequency separation, in comparison with the simulation results, can be attributed to the nonflat CW characteristic observed at 1.8 GHz (Fig. 23). In order to verify that this CW nonflat characteristic was not masking our results, we reoptimized the simulated OMN (namely, the capacitor values and their position) so that we could reproduce, in simulation environment, the measured behavior. Fig. 25 shows the comparison between the measured CW efficiency and output power profiles and the simulations of the updated PA-I.

After this modification, a better agreement between the measured and simulated efficiency degradation with the two-tone frequency separation increase was obtained, as it is possible to see in Fig. 26.

To prove that the efficiency degradation is mostly caused by the baseband nonoptimum impedances, we picked-up this updated version of PA-I and, in the simulation environment, used an ideal bias-tee (low impedance at baseband and high impedance at the fundamental). With this, we were able to remove the baseband impedance effects and leave only the residual ones that in this case, were due to the non-flat CW characteristic. The obtained results, shown in Fig. 26, show that the nonflatness is responsible for only 5% of the total 18% efficiency degradation observed before. Consequently, we can
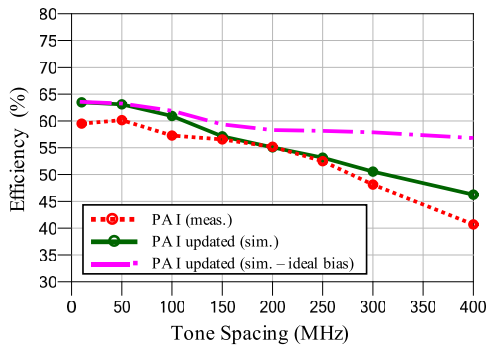
Fig. 26. Measured and simulated average efficiency versus two-tone frequency separation Δf for the implemented PA-I excited with two-tone signals of 2-GHz center frequency.
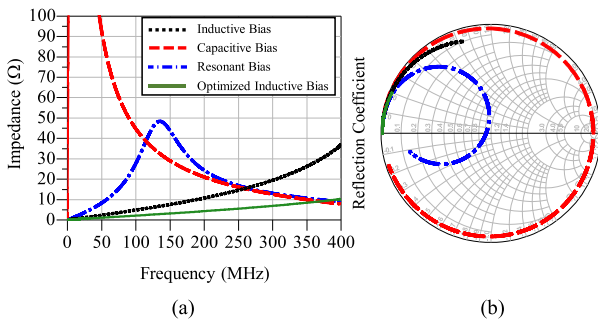

Fig. 27. Simulated intrinsic (a) magnitude of bias impedance profiles for all considered scenarios and (b) respective reflection coefficients of PA-II with different bias networks.
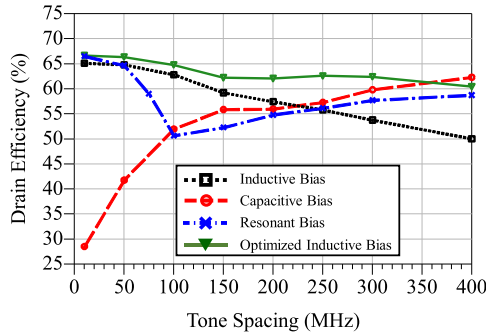

Fig. 28. Simulated average efficiency, for two-tone signals centered at 2 GHz, versus two-tone frequency separation Δf for the three bias network profiles under study.

conclude that the baseband termination is, indeed, the main reason for the observed efficiency degradation.

The capacitive bias impedance terminations' impact on the PA's efficiency was tested in the simulation environment. By returning back to the original bias network of PA-II and removing all capacitors above 20 pF, we created a resonance at very low frequency and obtained the capacitive impedance profile presented in Fig. 27. We have also ensured that the fundamental and harmonic terminations remained unchanged. We performed the two-tone simulations with the same tone separation sweep and obtained the efficiency profile presented in Fig. 28. At the lower tone separation, the efficiency degradation is high due to a very high capacitive bias impedance near the resonance. Then, as the tone separation increases and

moves away from the resonant frequency, the magnitude of the capacitive bias impedance decreases and the efficiency progressively recovers back to its ideal value, as predicted.

Finally, we retuned the bias network to have a resonance in the bias impedance profile as presented in Fig. 27, and performed the same test in the simulation environment. The obtained results are also presented in Fig. 28 to allow a direct comparison with the previous results for other bias impedance profiles. In the inductive impedance region (before the resonance), the efficiency decreases as the tone separation approaches the resonance, reaching its minimum value. Then, as it enters the capacitive region, it starts to increase again up to the ideal value.

Please note that at the resonance, the impedance presented to the device is of the same order of magnitude as the one we have with the inductive bias scenario (at 400 MHz) and we obtain the same efficiency degradation in the respective frequency separations. Another point that we would like to mention is the fact that, at 400-MHz separation, where the capacitive, resonance, and optimized bias network cases have the same order of impedance magnitude, the obtained efficiency performance is similar for all cases. Thus, these results support the conclusion that it is enough to minimize the magnitude of the bias impedance to prevent the efficiency degradation.

V. CONCLUSION

This paper provided a theoretical explanation for the observed efficiency degradation observed in wideband PAs subjected to concurrent band operation. The baseband terminations along with the baseband drain voltage modulation were found to be the dominant mechanisms responsible for this efficiency degradation. This was experimentally validated, showing that a PA with an optimized bias network presents far less efficiency degradation than a PA without an optimized bias network.

REFERENCES

[1] P. Colantonio, F. Giannini, and E. Limiti, *High Efficiency RF and Microwave Solid State Power Amplifiers*. London, U.K.: Wiley, 2009.

[2] F. H. Raab *et al.*, "Power amplifiers and transmitters for RF and microwave," *IEEE Trans. Microw. Theory Techn.*, vol. 50, no. 3, pp. 814–826, Mar. 2002.

[3] V. Carrubba *et al.*, "The continuous inverse class-F mode with resistive second-harmonic impedance," *IEEE Trans. Microw. Theory Techn.*, vol. 60, no. 6, pp. 1928–1936, Sep. 2012.

[4] X. Li, M. Helaoui, and X. Du, "Class-X—Harmonically tuned power amplifiers with maximally flat waveforms suitable for over one-octave bandwidth designs," *IEEE Trans. Microw. Theory Techn.*, vol. 66, no. 4, pp. 1939–1950, Apr. 2018.

[5] N. Tuffy, L. Guan, A. Zhu, and T. J. Brazil, "A simplified broadband design methodology for linearized high-efficiency continuous class-F power amplifiers," *IEEE Trans. Microw. Theory Techn.*, vol. 60, no. 6, pp. 1952–1963, Jun. 2012.

[6] P. Saad, C. Fager, H. Cao, H. Zirath, and K. Andersson, "Design of a highly efficient 2–4-GHz octave bandwidth GaN-HEMT power amplifier," *IEEE Trans. Microw. Theory Techn.*, vol. 58, no. 7, pp. 1677–1685, Jul. 2010.
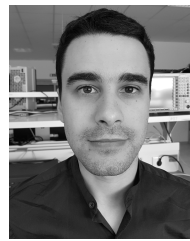
[7] L. Piazzon, R. Giofrè, P. Colantonio, and F. Giannini, "A wideband Doherty architecture with 36% of fractional bandwidth," *IEEE Microw. Wireless Compon. Lett.*, vol. 23, no. 11, pp. 626–628, Nov. 2013.

[8] J. Xia, X. Zhu, L. Zhang, J. Zhai, and Y. Sun, "High-efficiency GaN Doherty power amplifier for 100-MHz LTE-Advanced application based on modified load modulation network," *IEEE Trans. Microw. Theory Techn.*, vol. 61, no. 8, pp. 2911–2921, Aug. 2013.

[9] Q.-F. Cheng, H.-P. Fu, S.-K. Zhu, and J.-G. Ma, "Two-stage high-efficiency concurrent dual-band harmonic-tuned power amplifier," *IEEE Trans. Microw. Theory Techn.*, vol. 64, no. 10, pp. 3232–3243, Oct. 2016.

[10] P. Saad, P. Colantonio, L. Piazzon, K. Andersson, and C. Fager, "Design of a concurrent dual-band 1.8–2.4-GHz GaN-HEMT Doherty power amplifier," *IEEE Trans. Microw. Theory Techn.*, vol. 60, no. 6, pp. 1840–1849, Jun. 2012.

[11] S. Rumery and B. Noori, "A new technique for measuring the resonant behavior of power amplifier bias circuits," in *Proc. IEEE 69th ARFTG Conf.*, Honolulu, HI, USA, Jun. 2007, pp. 1–9.

[12] N. Zhu, R. McLaren, D. G. Holmes, J. L. Holt, P. Rashev, and J. K. Jones, "An integrated RF match and baseband termination supporting 395 MHz instantaneous bandwidth for high power amplifier applications," in *IEEE MTT-S Int. Microw. Symp. Dig.*, Honolulu, HI, USA, Jun. 2017, pp. 1114–1117.

[13] H. H. Ladhani, J. K. Jones, and G. Bouisse, "Improvements in the instantaneous-bandwidth capability of RF power transistors using in-package high-*k* capacitors," in *IEEE MTT-S Int. Microw. Symp. Dig.*, Baltimore, MD, USA, Jun. 2011, pp. 1–4.

[14] M. Franco, A. Guida, A. Katz, and P. Herczfeld, "Minimization of bias-induced memory effects in UHF radio frequency high power amplifiers with broadband signals," in *Proc. IEEE Radio Wireless Symp.*, Long Beach, CA, USA, Jan. 2007, pp. 369–372.

[15] D. Jeong *et al.*, "Linear CMOS power amplifier at Ka-band with ultra-wide video bandwidth," in *Proc. IEEE Radio Freq. Integr. Circuits Symp. (RFIC)*, Honolulu, HI, USA, Jun. 2017, pp. 220–223.

[16] B. Bunz, A. Ahmed, and G. Kompa, "Influence of envelope impedance termination on RF behaviour of GaN HEMT power devices," in *Proc. Eur. Microw. Conf.*, Oct. 2005, pp. 649–652.

[17] C. Ma, W. Pan, S. Shao, C. Qing, and Y. Tang, "A wideband Doherty power amplifier with 100 MHz instantaneous bandwidth for LTE-advanced applications," *IEEE Microw. Wireless Compon. Lett.*, vol. 23, no. 11, pp. 614–616, Nov. 2013.

[18] I. Takenaka, K. Ishikura, H. Takahashi, K. Hasegawa, K. Asano, and N. Iwata, "Improvement of intermodulation distortion asymmetry characteristics with wideband microwave signals in high power amplifiers," *IEEE Trans. Microw. Theory Techn.*, vol. 56, no. 6, pp. 1355–1363, Jun. 2008.

[19] N. B. D. Carvalho and J. C. Pedro, "A comprehensive explanation of distortion sideband asymmetries," *IEEE Trans. Microw. Theory Techn.*, vol. 50, no. 9, pp. 2090–2101, Sep. 2002.

[20] P. M. Cabral, J. C. Pedro, and N. B. Carvalho, "Bias networks impact on the dynamic AM/AM contours in microwave power amplifiers," in *Proc. Int. Workshop Integr. Nonlinear Microw. Millim.-Wave Circuits*, Aveiro, Portugal, Jan. 2006, pp. 38–41.

[21] M. Akmall *et al.*, "The effect of baseband impedance termination on the linearity of GaN HEMTs," in *Proc. IEEE 40th Eur. Microw. Conf.*, Paris, France, Sep. 2010, pp. 1046–1049.

[22] L. C. Nunes, D. R. Barros, P. M. Cabral, and J. C. Pedro, "Efficiency degradation in wideband power amplifiers," in *IEEE MTT-S Int. Microw. Symp. Dig.*, Philadelphia, PA, USA, Jun. 2018, pp. 1–4.

Diogo R. Barros (S'14) was born in Penalva do Castelo, Portugal, in 1990. He received the M.Sc. degree in electronic and telecommunications engineering from the University of Aveiro, Aveiro, Portugal, in 2015, where he is currently pursuing the Ph.D. degree in electrical engineering.

He has been a Research Assistant with the Institute of Telecommunications, Aveiro, since 2016. His current research interests include nonlinear distortion analysis, wideband high-efficiency power amplifier (PA) design and advanced MISO Doherty-outphasing PA architectures.

Pedro M. Cabral (S'04–M'07–SM'16) was born in Aveiro, Portugal, in 1979. He received the electrical engineering and Ph.D. degrees from the Universidade de Aveiro, Aveiro, Portugal, in 2002 and 2006, respectively.

He is currently a Senior Researcher with the Instituto de Telecomunicações, Aveiro, and an Assistant Professor with the Universidade de Aveiro. His current research interests include active device nonlinear modeling, design of microwave circuits, high-efficiency power amplifiers, and wireless transmitter architectures.

Dr. Cabral has been a Reviewer for several publications, including the IEEE TRANSACTIONS ON MICROWAVE THEORY AND TECHNIQUES, the IEEE TRANSACTIONS ON COMPUTER-AIDED DESIGN OF INTEGRATED CIRCUITS AND SYSTEMS, the IEEE TRANSACTIONS ON INSTRUMENTATION AND MEASUREMENT, and the IEEE TRANSACTIONS ON CIRCUITS AND SYSTEMS—I: REGULAR PAPERS. He was a recipient of the 2002 Best Electrical Engineering Student Prize of the University of Aveiro. In 2004, he was a Finalist in the Student Paper Competition of the IEEE Microwave Theory and Techniques Society International Microwave Symposium.

Luís Cótimos Nunes (S'13–M'17) was born in Guarda, Portugal, in 1986. He received the M.Sc. and Ph.D. degrees in electrical engineering from the Universidade de Aveiro, Aveiro, Portugal, in 2010 and 2015, respectively.

From 2016 to 2017, he was an RF Design Engineer with Huawei Technologies, Stockholm, Sweden. He is currently a Researcher Assistant with the Institute of Telecommunications, Aveiro. His current research interests include active device modeling, nonlinear distortion analysis, and the design of microwave circuits, especially high-efficiency and linear power amplifiers.

Dr. Nunes is a member of the IEEE Microwave Theory and Techniques Society and the IEEE Electron Devices Society.

José C. Pedro (S'90–M'95–SM'99–F'07) received the diploma, doctoral, and habilitation degrees in electronics and telecommunications engineering from the University of Aveiro, Aveiro, Portugal, in 1985, 1993, and 2002, respectively.

He is currently a Full Professor with the University of Aveiro. He has authored 2 books and authored or coauthored over 200 papers in international journals and symposia. His current research interests include active device modeling and the analysis and design of various nonlinear microwave circuits.

Mr. Pedro was the recipient of various prizes including the Marconi Young Scientist Award in 1993, the 2000 Institution of Electrical Engineers Measurement Prize, the 2015 EuMC Best Paper Microwave Prize, and the Microwave Distinguished Educator Award. He has served the scientific community as a Reviewer and an Editor of several conferences and journals, namely, the IEEE TRANSACTIONS ON MICROWAVE THEORY AND TECHNIQUES, of which he is currently the Editor-in-Chief.

Appendix C

IMS 2019 Publication

Impact of the Input Baseband Impedance on the Instantaneous Bandwidth of Wideband Power Amplifiers

Diogo R. Barros, Luís C. Nunes, Pedro M. Cabral and José C. Pedro

DETI, Instituto de Telecomunicações, Universidade de Aveiro

Campus Universitário de Santiago, 3810-193 Aveiro, Portugal

Abstract—**This paper addresses the instantaneous bandwidth degradation of radiofrequency power amplifiers (RFPAs) still visible after eliminating all known causes related with the output matching network (OMN). First, the origin of this degradation, identified by the reduction of the PAs efficiency and linearity, is traced to the input baseband impedance terminations and a qualitative description of the phenomenon is presented. Then, an instantaneous bandwidth comparison is performed between two 30W GaN RFPAs, in which all impedance matching conditions are the same except for the input video-bandwidth impedance terminations. This work shows that, in addition to the adequate conception of the OMN, an optimally designed input impedance profile is also an important design consideration to retain the efficiency and linearity performance of RFPAs, for scenarios that require a wide instantaneous bandwidth.**

Keywords—**baseband impedance, instantaneous bandwidth, power amplifiers, video bandwidth, wideband.**

I. INTRODUCTION

The bandwidth and energy efficiency are two of the most important factors that shape the evolution of wireless communications systems. On the one hand, wide bandwidth is required to cope with the progressively higher data rate demand, as in wideband multicarrier/concurrent band scenarios. On the other hand, there is a widespread interest to minimize the energy consumption of these systems, not only for operational cost reduction but also for environmental awareness. Therefore, an extensive research effort is being made to fully understand the phenomena that leads to performance degradation when a PA is no longer excited with a CW signal but with one of considerable instantaneous bandwidth [1-3].

Several studies have shown that the baseband impedance terminations are an important cause of performance degradation and proposed methods to correct it. In [4], Bunz *et al.* have reported a linearity and efficiency degradation from both the input and output baseband terminations through experimental envelope source and load-pull measurements. In [5], Hu *et al.* showed that an appropriate injection of the 2nd order intermodulation component at the input, through feedback, can reduce the 3rd order intermodulation distortion by 12dB. In [6], Kwon et. al have reported that the 5th order IMD could also be improved by optimal control of the amplitude and phase of the injected 2nd order baseband intermodulation.

Recently, Nunes *et al.* [7], reported a thorough theoretical study of the efficiency degradation induced by the output baseband impedance terminations. The input baseband impedance impact on the efficiency of wideband PAs is still largely unexplored and commonly ignored during the design stage.

Therefore, the aim of this work is to discuss the input baseband terminations' impact on the instantaneous bandwidth of wideband RFPAs, and how to properly correct it. Moreover, it is shown that it can produce a severe linearity and efficiency degradation in scenarios that require high instantaneous bandwidth, if not properly addressed.

II. INPUT BASEBAND TERMINATIONS' EFFECT ON THE INSTANTANEOUS BANDWIDTH

Let us consider the simplified circuit representation of a RFPA presented in Fig. 1. The PA is composed of three main blocks: the output matching network (OMN) to provide the required power and efficiency impedance matching at the output; the input matching network (IMN) to impose the matching for gain and stable operation; and finally, the device itself, whose nonlinear internal capacitances are determinant for this analysis. Please note that, since the device's extrinsic components are linear, they can be integrated in the matching networks.
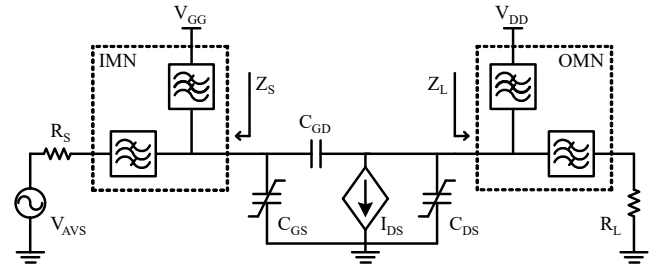

Fig. 1. Simplified circuit representation of a RFPA.

As shown in [4], the OMN needs to provide nearly ideal baseband termination conditions, i.e., a very low impedance, to the intrinsic drain of the device, to prevent the output dependent efficiency and linearity degradation under modulated signal excitation.

The profile of the input baseband impedance, Z_{S_BB}, is commonly imposed by the input bias circuitry. As a result, Z_{S_BB} is connected in parallel with both the C_{GS} and the input Miller reflected C_{GD}. From this point on, this C_{GD} Miller component is assumed to always be integrated into C_{GS} and will no longer be directly referred to in the remainder of this analysis.

In a conventional IMN design, a large inductor or a high impedance transmission line are commonly used in series with a resistor to simultaneously decouple the RF path from the bias circuit and ensure stable operation. This type of bias network is depicted in Fig. 2a). While this method greatly simplifies the design, Z_{S_BB} is commonly inductive in nature at low
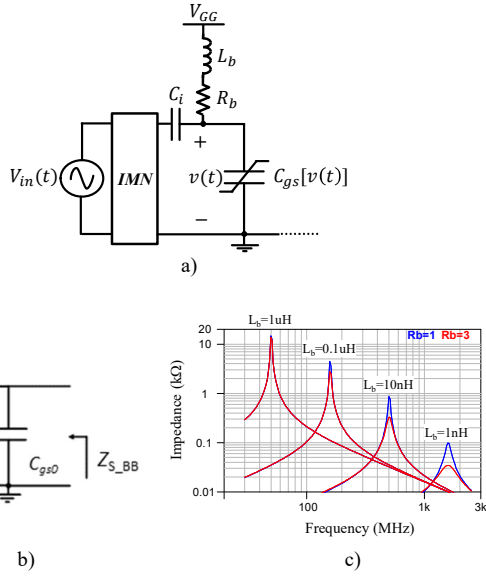
Fig. 2. a) Conventional input bias circuit with stabilization resistor, b) respective small-signal equivalent circuit and c) impedance profiles for several inductor and resistor values.

frequencies and, therefore, forms a parallel resonant circuit together with C_{GS}, as shown in Fig. 2b). Depending on the quality factor, the baseband impedance at the resonant frequency can be very high, as presented in Fig. 2c).

The reason why most PA designers ignore the input baseband impedance is because they assume that there is no current at the input device at these frequencies. However, these components are generated due to the nonlinearity introduced by the C_{GS} variation, when the input is a wideband modulated signal. Since C_{GS} is a nonlinear capacitance, its current, i_C, is given by

$$i_C(t) = \frac{dQ[v(t)]}{dt} = \frac{dQ(v)}{dv}\frac{dv(t)}{dt} = C_{GS}[v(t)]\frac{dv(t)}{dt}, \quad (1)$$

where $C_{GS}[v(t)]$, describes the variation of the capacitance with the intrinsic gate voltage. For instance, if the input excitation is a two-tone signal and the nonlinear C_{GS} variation is modelled by the first order polynomial

$$C_{GS}(v(t)) = C_{gs0} + C_{gs1}v(t), \quad (2)$$

typical for a common class-AB PA, then the baseband current component is

$$i_{BB}(t) = \frac{1}{4}V_P^2 C_{gs1}\omega_m \sin(2\omega_m t), \quad (3)$$

where V_P is the peak voltage and ω_m is the half separation of the two-tone signal. Since this current is supplied by the bias network circuit presented in Fig. 2b), the baseband voltage developed at the intrinsic gate is given by

$$v_{BB}(t) = \frac{1}{4}|Z_{BB\_S}|V_P^2 C_{gs1}\omega_m \sin(2\omega_m t + \angle(Z_{BB\_S})), \quad (4)$$

which, for a typical inductive Z_{BB_S} rises with the square of ω_m. Therefore, if the parallel resonance frequency of the input circuit coincides with this baseband frequency, a large V_{GS}

fluctuation is generated at the intrinsic gate node, disturbing the normal quiescent point of the PA. In particular, the conduction angle of the PA is changed between class-AB, B and C within the period of the envelope, leading to a variation of its linearity and efficiency as shown in the following section.

Please note that v_{BB} is proportional not only to the magnitude of Z_{BB_S} but also to the amplitude and bandwidth of the input signal and the variation of C_{gs}. Therefore, wideband, high power PAs which normally present higher C_{gs} variation are expected to be more susceptible to the described phenomena.

III. EXPERIMENTAL RESULTS

In order to quantitatively evaluate the efficiency and linearity degradation expected in a real device, two PAs with different input bias networks were designed using Wolfspeed's CGH27030F GaN HEMT and implemented on a 0.76 mm Isola Astra substrate. A photograph of the implemented PAs is presented in Fig. 3.
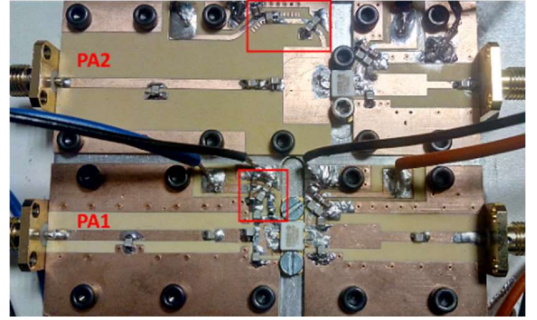

Fig. 3. Photo of the implemented PAs.

The input matching network (IMN) and output matching network (OMN) were designed to minimize the variation of the efficiency, output power and gain profiles over a 650 MHz bandwidth span. The simulated and measured efficiency, PAE and output power of each PA, at the 2.5 dB compression level, are presented in Fig. 4 and Fig. 5 respectively.

While the OMN was optimally designed to obtain a very low baseband impedance up to 1 GHz, the IMN of each PA was designed to present two distinct Z_{BB} profiles to evaluate the efficiency and linearity degradation: one corresponding to the conventional structure previously presented on Fig. 2a) (PA-I); and a second one with an appropriately designed baseband
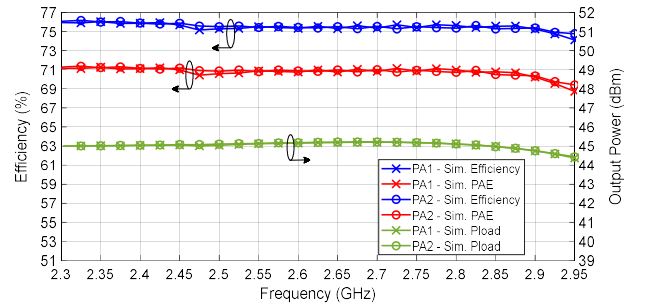

Fig. 4. Simulated efficiency, PAE and output power under CW excitation, at the 2.5dB gain compression point.
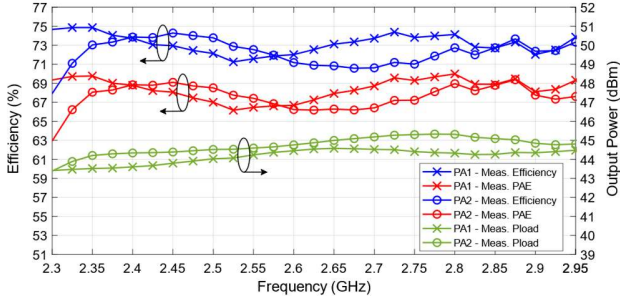
Fig. 5. Measured efficiency, PAE and output power under CW excitation, at the 2.5dB gain compression point.

impedance to avoid a parallel resonance with the device's input impedance (PA-II). This was achieved by adding a capacitor in parallel with the low frequency stabilization resistor and by replacing the inductor by a short transmission line. In practice, this is the same as reducing the quality factor of the parallel resonant circuit and increasing the resonance frequency. With these changes, the input matching for the fundamental and the bias circuit must be designed together since, without the large inductor, they will load one another. Both impedance profiles are presented in Fig. 6.
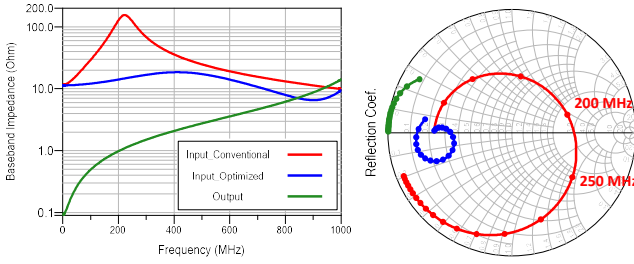
Fig. 6. Baseband impedance profiles at the intrinsic gate plane for the designed input and output networks.

The dynamic behavior of the PA was assessed under a two-tone excitation, centered at 2.55GHz, with a constant average available power of 26dBm. The separation between the tones was swept between 10MHz and 400MHz. The simulated and measured average efficiency are presented in Fig. 7 and third-order IMD powers are presented in Fig. 8.
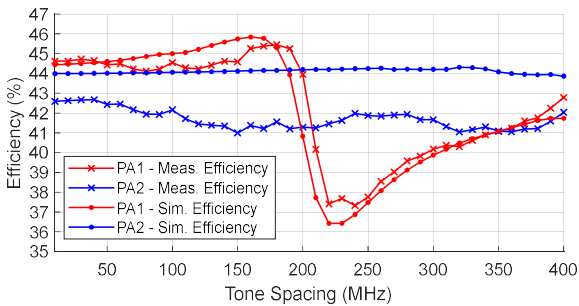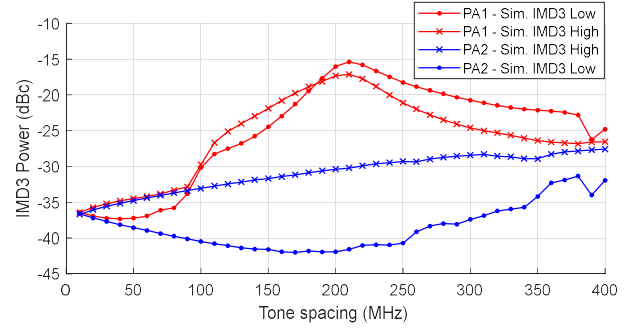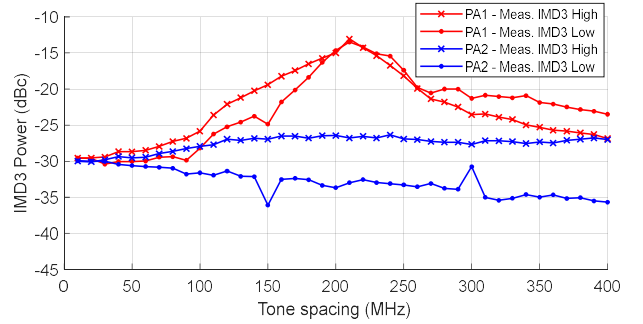

Fig. 7. Simulated and measured average efficiency of both implemented PAs, under two-tone excitation.

a)

b)

Fig. 8. Comparison between a) the simulated and b) measured third-order IMD powers of both implemented PAs, under two-tone excitation.

For PA1, both the simulated and measured average efficiencies have a sharp degradation of nearly 8% immediately above 200 MHz, where the impedance presented by the IMN at the baseband is closer to the parallel resonance. This is also the frequency region where the linearity of the PA is most degraded with an increase in the 3rd order IMD power of 15dB, with respect to the initial tone separation of 10 MHz.

Conversely, for the optimized network of PA2, both the efficiency and linearity remain nearly unchanged over the entire video bandwidth. The measured average efficiency is 2 % lower at the lower tone separations and has higher variation over the instantaneous bandwidth than the one predicted by the simulation, which is attributed to the small differences on the CW figures of merit of each PA.

IV. CONCLUSION

This work provided a description of the mechanism that relates the limited instantaneous bandwidth with the baseband terminations of the input network. The source of this limitation lies on the parallel resonance between the IMN baseband impedance terminations with the input capacitance of the device, producing a large intrinsic gate voltage modulation at the baseband frequencies. The corresponding modulation of the conduction angle of the PA leads to the degradation of its linearity and efficiency. The mechanism was experimentally demonstrated, along with a design method to correct it, this way extending the instantaneous bandwidth of wideband PAs, via an optimal design of their input bias networks.

REFERENCES

[1] X. Chen, W. Chen, Gongzhe Su, F. M. Ghannouchi and Z. Feng, "A concurrent dual-band 1.9–2.6-GHz Doherty power amplifier with Intermodulation impedance tuning," 2014 *IEEE MTT-S International Microwave Symposium (IMS2014)*, Tampa, FL, 2014, pp. 1-4.

[2] X. Chen, W. Chen, F. M. Ghannouchi, Z. Feng and Y. Liu, "Enhanced Analysis and Design Method of Concurrent Dual-Band Power Amplifiers With Intermodulation Impedance Tuning," in *IEEE Transactions on Microwave Theory and Techniques*, vol. 61, no. 12, pp. 4544-4558, Dec. 2013.

[3] J. Li, W. Chen, F. Huang and Z. Feng, "Multiband and Multimode Concurrent PA With Novel Intermodulation Tuning Network for Linearity Improvement," in *IEEE Microwave and Wireless Components Letters*, vol. 28, no. 3, pp. 248-250, March 2018.

[4] B. Bunz, A. Ahmed and G. Kompa, "Influence of envelope impedance termination on RF behaviour of GaN HEMT power devices," *European Gallium Arsenide and Other Semiconductor Application Symposium*, GAAS 2005, Paris, 2005, pp. 649-652.

[5] Yongcai Hu, Jean C. Mollier and Juan Obregon, "A Nevv Method of Third-Order Intermodulation Reduction in Nonlinear Microwave Systems," in *IEEE Transactions on Microwave Theory and Techniques,* vol. 34, no. 2, pp. 245-250, Feb 1986.

[6] Y. Kwon, Y. Jeong, Y. Kim and C. Kim, "A Design of Predistortion Linearizer using 2nd Order Low Frequency Intermodulation Signal Injection," 2003 *33rd European Microwave Conference*, Munich, Germany, 2003, pp. 249-252.

[7] L. C. Nunes, D. R. Barros, P. M. Cabral and J. C. Pedro, "Efficiency Degradation Analysis in Wideband Power Amplifiers," in *IEEE Transactions on Microwave Theory and Techniques*.

Appendix D

TMTT 2019 Publication

Impact of the Input Baseband Terminations on the Efficiency of Wideband Power Amplifiers Under Concurrent Band Operation

Diogo R. Barros, *Student Member, IEEE*, Luís C. Nunes, *Member, IEEE*,
Pedro M. Cabral, *Senior Member, IEEE*, and José Carlos Pedro, *Fellow, IEEE*

Abstract— **This article presents a theoretical explanation of the efficiency degradation in wideband radio frequency power amplifiers (RFPAs) under concurrent dual-band operation that is still visible after eliminating all known causes related to the output matching network (OMN). First, the origin of this degradation, identified by the reduction of the PA's efficiency and linearity, is traced to the input baseband impedance terminations. Then, a theoretical model that describes the phenomenon and qualitatively predicts the efficiency variation under concurrent dual-band operation is presented using a simple model based on two-tone excitation. Finally, the proposed explanation is confirmed by comparing the efficiency performance of two 30-W GaN RFPAs of distinct instantaneous bandwidth determined by different input video-bandwidth terminations, under two-tone and concurrent dual-band operation. This article shows that, in addition to the adequate OMN design, an optimal input baseband impedance profile is also an important design constraint needed to keep the efficiency and linearity performance of RFPAs, for scenarios that require a wide instantaneous bandwidth.**

Index Terms— **Baseband impedance, instantaneous bandwidth, power amplifiers, video bandwidth, wideband.**

I. INTRODUCTION

BANDWIDTH and energy efficiency are two of the most important factors that shape the evolution of wireless communications systems. On the one hand, wide bandwidth is required to cope with the progressively higher data rate demand, as in wideband multicarrier/concurrent band scenarios. On the other hand, there is a widespread interest to minimize the energy consumption of these systems, not only for operational cost reduction but also for environmental awareness. Therefore, an extensive research effort is being

made to fully understand the phenomena that leads to performance degradation when a power amplifier (PA) is no longer excited with a continuous wave (CW) signal but with one of considerable instantaneous bandwidth [1]–[3].

Several studies have shown that the baseband impedance terminations are an important cause of performance degradation, and therefore, methods to correct it have been proposed. Williams *et al.* [4] have shown how the output and input baseband terminations affect the IM3 distortion, through the envelope analysis of measured time-domain waveforms. Bunz *et al.* [5] have reported linearity and efficiency degradation from both the input and output baseband terminations through experimental envelope source and load–pull measurements. Hu *et al.* [6] showed that an appropriate injection of the second-order baseband intermodulation component at the input, through feedback, can reduce the third-order intermodulation distortion (IMD) by 12 dB. Kwon *et al.* [7] have reported that the fifth-order IMD could also be improved by optimal control of the amplitude and phase of the injected second-order baseband intermodulation product. Chaudhary [8] reported an impedance optimization scheme at higher order baseband components.

To allow optimal device performance for wideband applications, devices started to include in-package circuitry to provide wideband low baseband impedance terminations at the device's intrinsic terminals [9]. In addition, baseband characterization and measurement methods have also been improved [10], [11].

Recently, Nunes *et al.* [12] reported a theoretical study of the efficiency degradation induced by the output baseband impedance terminations. However, the input baseband impedance impact on the wideband PA's efficiency is still largely unexplored and commonly ignored during the design stage. Only more recently, the mechanism of efficiency degradation associated with the input baseband impedance was introduced in [13], explaining that if it is not properly addressed, a bias fluctuation is generated, inducing a severe linearity and efficiency degradation in scenarios that require a very wide instantaneous bandwidth.

Therefore, the aim of this article is to expand the analysis presented in [13], explaining in a comprehensive, qualitative, and quantitative way, how the bias fluctuation generated by the baseband impedance terminations affects the PA performance

Fig. 1.   Simplified circuit representation of an RFPA.

Fig. 2.   (a) Conventional input bias circuit with stabilization resistor, (b) respective small-signal equivalent circuit, and (c) impedance profiles for several inductor and resistor values (with Cgs0 = 10 pF).

when excited with a wideband signal. For that, a simple model is advanced to estimate the efficiency degradation related to the input baseband impedance.

This article is structured as follows. First, in Section II, we revisited the performance degradation mechanisms due to the baseband impedance terminations. In Section III, we derive a simple theoretical model that is used to understand and to predict their impact on the PA's performance. Three specific baseband impedance termination scenarios were considered, which led to distinct degradation profiles. In Section IV, we experimentally demonstrate that the input baseband terminations can degrade PA performance and that it can be prevented through adequate IMN design. In addition, we demonstrate that the theoretical model is able to predict the performance degradation of practical wideband PAs, and thus, be used as a simple and fast tool to evaluate its instantaneous bandwidth. Finally, the conclusions of this article are summarized in Section V.

II. EFFICIENCY DEGRADATION MECHANISM RELATED WITH THE INPUT BASEBAND TERMINATION

Let us consider the simplified circuit representation of a radio frequency PA (RFPA) presented in Fig. 1. The PA is composed by three main blocks: the output matching network (OMN) to provide the required power and efficiency impedance matching at the output; the input matching network (IMN) to impose the matching for gain and stable operation; and finally, the device itself, whose nonlinear internal capacitances are determinant for this analysis. Please note that, since the device's extrinsic components are linear, they can be integrated into the matching networks.

As shown in [5], the OMN needs to provide nearly ideal baseband termination conditions, i.e., very low impedance to the intrinsic drain of the device, to prevent the output dependent efficiency and linearity degradation under modulated signal excitation. We assume that the OMN is always optimized to present optimal baseband impedance terminations in practical PA design so that we can focus solely on the performance degradation due to the IMN's baseband profile.

The profile of the input baseband impedance, Z_{S_BB}, is commonly imposed by the input bias circuitry. As a result, Z_{S_BB} is connected in parallel with both the C_{GS} and the input Miller reflected C_{GD}. Since the output baseband impedance is assumed to be short circuit, the voltage gain at the baseband components is zero, and therefore, the Miller component is
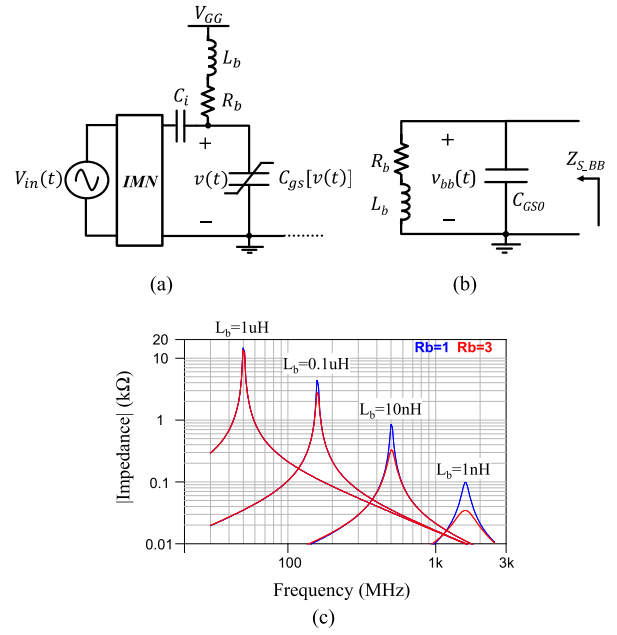
simply the C_{GS} value. From this point on, this C_{GD} Miller component is assumed to always be integrated into C_{GS} and will no longer be directly referred to in the remainder of this analysis.

In a conventional IMN design, a large inductor or a high characteristic impedance transmission line is commonly used in series with a resistor to simultaneously decouple the RF path from the bias circuit and ensure stable operation. This type of bias network is shown in Fig. 2(a). While this method greatly simplifies the design, Z_{S_BB} is commonly inductive in nature at low frequencies and, therefore, forms a parallel resonant circuit together with C_{GS}, as shown in Fig. 2(b). Depending on the quality factor, the baseband impedance at the resonant frequency can be very high, as presented in Fig. 2(c).

The reason why most PA designers ignore the input baseband impedance is that they assume that there is no current at the input of the device at these frequencies. However, these components are generated due to the nonlinearity introduced by the C_{GS} variation when the input is a wideband modulated signal. Since C_{GS} is a nonlinear capacitance, its current, i_C, is given by

$$i_C(t) = C_{GS}[v(t)]\frac{dv(t)}{dt} \qquad (1)$$

where $C_{GS}[v(t)]$ describes the variation of the capacitance with the intrinsic gate voltage. For instance, if we approximate the $C_{GS}[v(t)]$ variation (normally modulated by a hyperbolic tangent function [14]) with a first-order polynomial function

$$C_{GS}(v(t)) = C_{gs0} + C_{gs1}v(t) \qquad (2)$$

which corresponds to a quadratic charge function

$$Q_{GS}(v(t)) = q_{gs0} + C_{gs0}v(t) + \frac{C_{gs1}}{2}v(t)^2. \qquad (3)$$
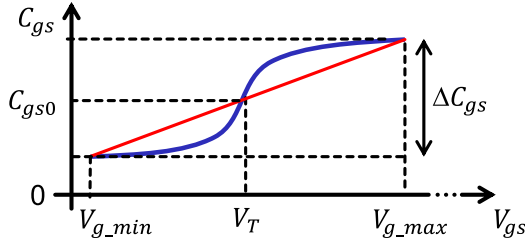
Fig. 3. $C_{GS}[v(t)]$ nonlinear profile and the respective curve fitting with a first-order polynomial model.
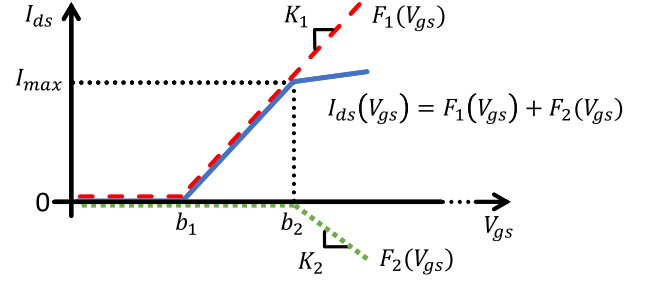

Fig. 4. Piecewise linear functions used to approximate the current source behavior: current mode operation (red dashed line), current saturation (blue solid line), and complete model (green dots).

Thus, the resulting baseband current component is

$$i_{\mathrm{BB}}(t) = -\frac{1}{4}V_P^2 C_{\mathrm{gs1}}\omega_m \sin(2\omega_m t) \qquad (4)$$

where V_P is the peak excitation voltage, and ω_m is half of the separation frequency. The coefficients C_{gs0} and C_{gs1} can be extracted using least squares and assuming a sinusoidal input excitation with the maximum $v(t)$ voltage amplitude, as shown in Fig. 3.

Since this current is supplied by the bias network circuit presented in Fig. 2(b), the baseband voltage developed at the intrinsic gate is given by

$$v_{\mathrm{BB}}(t)$$
$$= V_{\mathrm{GG}} + \frac{1}{4}|Z_{S_{\mathrm{BB}}}(2\omega_m)|V_P^2 C_{\mathrm{gs1}}\omega_m \sin[2\omega_m t + \angle(Z_{S_{\mathrm{BB}}}(2\omega_m))]. \qquad (5)$$

Please note that, by considering that $C_{GS}[v(t)]$ is only excited by the fundamental voltage component, we are neglecting the nonlinear feedback, i.e., the change in the fundamental voltage component due to the baseband component is not fed back into the model to update v_{BB}. However, even with this simplification, the model can predict reasonably well the bias fluctuation, as it will be shown later on.

For a typical inductive baseband impedance, $Z_{S\_BB} = j\omega_m L$, v_{BB} rises with the square of ω_m. Therefore, a large v_{BB} fluctuation can be generated at the intrinsic gate node at $2\omega_m$, disturbing the normal quiescent point of the PA. In particular, the conduction angle of the PA is changed between classes-A and C within the period of the envelope, leading to a variation of its linearity and efficiency, as shown in Section III.

Please note that v_{BB} is proportional not only to the magnitude of Z_{S_BB}, but also to the amplitude and bandwidth of the input signal and the variation of C_{GS}. Therefore, wideband, high-power PAs, which normally present higher C_{GS} variation, are expected to be more susceptible to the described phenomena, for the same baseband impedance conditions.

III. IMPACT OF INPUT BASEBAND VOLTAGE FLUCTUATION

In Section II, we have observed that the nonlinear C_{GS} can create an intrinsic baseband voltage fluctuation, which depends on the amplitude and phase of baseband termination, Z_{S_BB}.

To analyze the impact of the v_{BB} fluctuation, we use a current source model based on the piecewise linear squashing technique, as was already proposed in [15] and [16] to be able to directly calculate the fundamental and baseband components of the PA current. The model is composed of two piecewise linear functions, F_n, with different gains/derivatives (K_n) and input bias (b_n), as shown in Fig. 4, in which F_1 describes the current mode operation, and F_2 imposes the current saturation profile typically observed in highly efficient overdriven PAs. With this, we preserve the simplicity of the model without losing the qualitative representation of the PA's normal operation.

As a consequence of the model's simplicity, we can analytically compute the dc and fundamental Fourier components of each function, according to

$$I_0(V_{\mathrm{GG}}, A) = \sum_{n=1}^{2} \frac{K_n}{\pi}[(V_{\mathrm{GG}} - b_n)\theta_n + A\sin(\theta_n)] \qquad (6)$$

$$I_1(V_{\mathrm{GG}}, A) = \sum_{k=1}^{2} \frac{K_n A}{2\pi}[2\theta_n - \sin(2\theta_n)] \qquad (7)$$

where $2\theta_n$ is the conduction angle for each function, F_n, which, for an RF amplitude, A, and an input bias V_{GG}, can be computed as

$$2\theta_n = \mathrm{real}\left(2\mathrm{acos}\left(-\frac{V_{\mathrm{GG}} - b_n}{A}\right)\right). \qquad (8)$$

Please note that I_0 and I_1 represent the dc and fundamental components of a current waveform that tends to a square wave as the PA is driven deeper into saturation. This waveform is significantly different from the one observed in overdriven class-B PAs, where the short circuit harmonic terminations ensure that the drain voltage is always sinusoidal. This imposes a limit on the amplitude of the fundamental drain voltage component, $V_{1\_max} = V_{\mathrm{DD}} - V_K$, and, consequently, I_1 also becomes limited at

$$I_{1\_max} = \frac{V_{\mathrm{DD}} - V_K}{R_L}. \qquad (9)$$

However, if the current waveform is allowed to be square, the fundamental current component can indeed surpass this limit, as predicted by the model, and normally observed in class-F^{-1} PAs.

We start by analyzing how both V_{GG} and A impact the Fourier components (6) and (7), assuming that $K_2 = -K_1$, for different classes of operation. The bias voltages for each class are computed as $V_{\mathrm{GG}} = V_T + h \cdot I_{\max}/K_1$, with
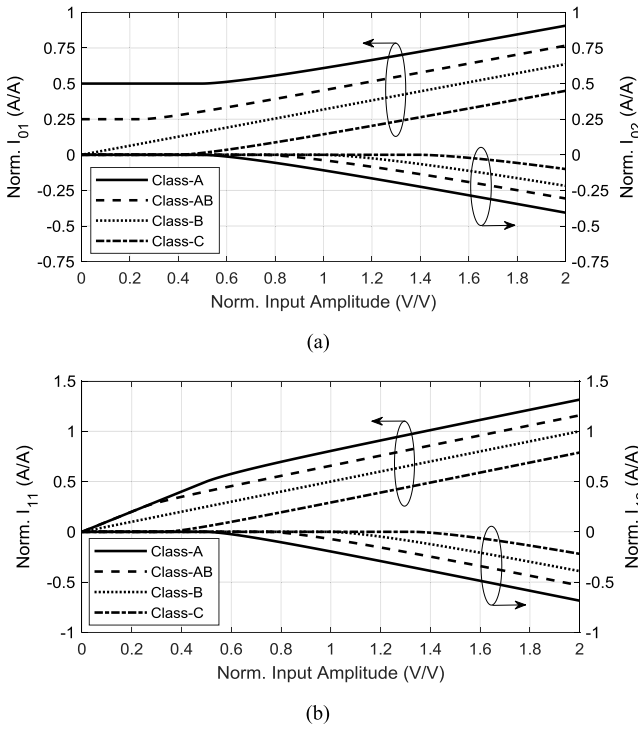
(a)

(b)

Fig. 5. Model predicted (a) dc and (b) fundamental components of each i_{DS} term, biased at different classes of operation, and normalized to I_{max}. The input amplitude is normalized to $b_2 - b_1 = I_{max}/K_1$.
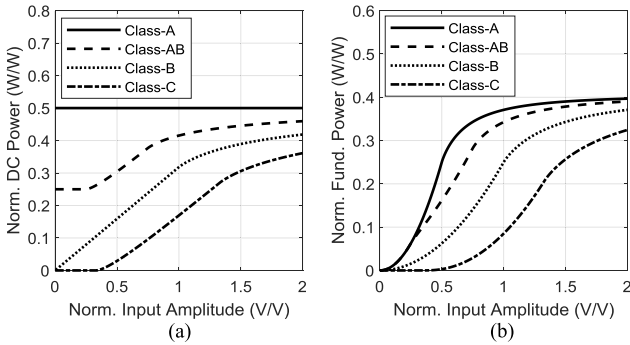

(a)   (b)

Fig. 6. Model predicted (a) dc and (b) fundamental powers, normalized to $I_{max}V_{DD}$, for a piecewise linear current source biased at different classes of operation.

$h = \{0.5, 0.2, 0, -0.3\}$, corresponding to classes-A, AB, B, and C, respectively. The dc and fundamental components of i_{DS}, I_0, and I_1, respectively, are presented in Fig. 5, normalized to I_{max}. Note that each component is the sum of two terms as described in (6) and (7), one for each basis function of the model, denoted by the index n. The combination of these terms ($I_0 = I_{0,1} + I_{0,2}$ and $I_1 = I_{1,1} + I_{1,2}$) leads to the dc and output powers and efficiency profiles presented in Figs. 6 and 7, respectively. The class-A bias voltage is defined as the sum of the threshold voltage, V_T, with half of the voltage excursion, $0.5 I_{max}/K_1$, with K_1 representing the device transconductance G_m, the class-B is defined with a bias voltage equal to V_T, and the class-AB is with a bias voltage in-between class-A and class-B. Class-C is defined with a bias below V_T voltage.
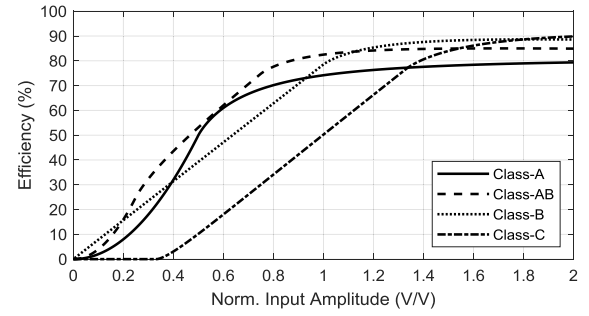

Fig. 7. Model predicted efficiency for a piecewise current source biased at different classes of operation. The input amplitude is normalized to $b_2 - b_1 = I_{max}/K_1$.
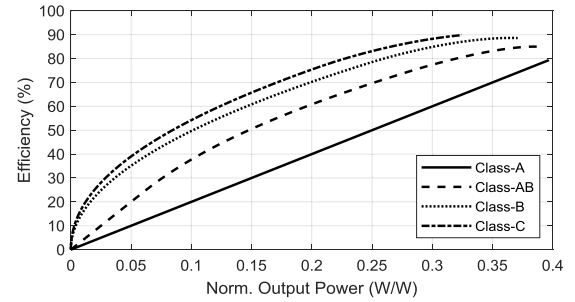

Fig. 8. Efficiency versus output power normalized to $I_{max}V_{DD}$, predicted by the model, for a piecewise current source biased at different operation classes.

The first observation we can make from the analysis of these results is that the second i_{DS} terms ($I_{0,2}$ and $I_{1,2}$) are only excited for very large-input power level in the same manner for all operation classes, as observed in Fig. 5. Since these terms represent the PA's compression, they only start to have an impact earlier or later, depending on the PA gain. Until there, the efficiency is mostly governed by the first i_{DS} terms ($I_{0,1}$ and $I_{1,1}$), the ones that describe the current mode operation.

Another aspect that we would like to highlight is the efficiency profile of the class-AB in comparison with the class-B PA. Looking into Fig. 7, it is possible to conclude that, for some input power levels, the efficiency of a class-AB PA is higher. This could be unexpected as we normally think in terms of the maximum efficiency (considering the onset of PA saturation) and that the PA is terminated with the optimum impedance for each operation class. However, this can be easily understood since an ideal class-B PA can have a maximum efficiency of $\pi/4$ and, therefore, at half of its input voltage excursion, its efficiency will be $\pi/8$, whereas, due to the higher gain of the class-A PA, this one will reach the maximum efficiency of 0.5, which is higher. Thus, if we sweep the input power, we start to see almost no efficiency in a class-AB PA, due to the large dc component without any output power, and then, due to the higher gain, the efficiency will grow faster.

In fact, if we represent the efficiency versus output power, as shown in Fig. 8, the class-B efficiency is always higher than the class-AB efficiency for the same output power level. However, representing the performance versus input power
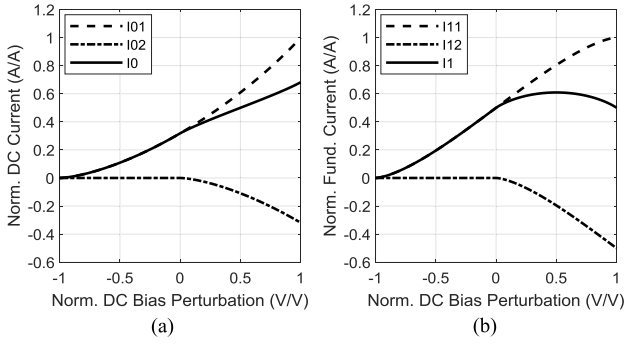
Fig. 9. Model predicted (a) dc current components and (b) fundamental current components normalized to the maximum current of the device, I_{max}. The dc bias perturbation is normalized to $b_2 - b_1 = I_{max}/K_1$.
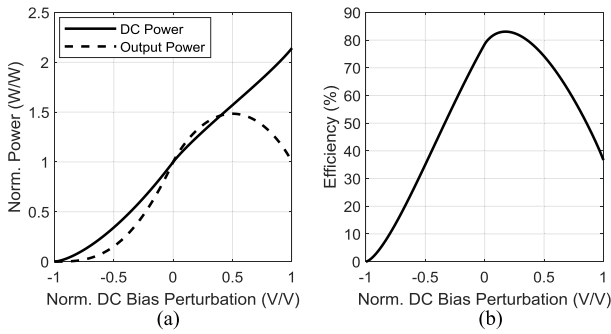

Fig. 10. Model predicted (a) dc and output powers normalized to the respective dc and fundamental powers obtained for a class-B at the onset of saturation and (b) the efficiency for swept dc bias voltage and under CW excitation at the edge of current saturation for class-B bias. The dc bias perturbation is normalized to $b_2 - b_1 = I_{max}/K_1$.

will be helpful to understand the efficiency degradation, due to the input baseband voltage fluctuation, when the envelope amplitude and the baseband voltage are changing in time.

Then, we evaluated the PA's performance with respect to the input bias voltage for fixed excitation amplitude (which will correspond to the baseband voltage variations when a modulated signal will be used). Thus, considering optimal load impedance and constant CW excitation with maximum amplitude for a class-B PA, the obtained dc and fundamental current components for different input bias voltages (normalized to the threshold voltage, i.e., the nominal bias of a class-B PA) are presented in Fig. 9.

When the bias voltage is reduced below the nominal bias, the peak voltage of the signal is lower due to the fixed amplitude excitation, meaning that $I_{0,1}$ and $I_{1,1}$ are the only components that are excited, and both components decrease as the PA is biased deeper into class-C. Thus, since the output power is quadratically dependent on I_1 and the dc power is approximately proportional to I_0, the efficiency decreases monotonically, as observed in Fig. 10. Please note that, to be easier to understand the change in the PA performance to the nominal bias ($V_{GG} = V_T$) we normalized the obtained powers to the ones calculated for the nominal bias, meaning that, for $V_{GG} = V_T$, both powers are equal to one.

Conversely, when the bias voltage is increased from the class-B bias voltage, the second terms $I_{0,2}$ and $I_{1,2}$ become progressively higher due to the current waveform clipping. Both the total dc and fundamental currents decrease with respect to the case where only the components $I_{0,1}$ and $I_{1,1}$ are considered, reducing the fundamental component, the output power, and the efficiency. However, there is a zone where if we increase the bias V_{GG} into class-AB, these components increase more slowly than $I_{0,1}$ and $I_{1,1}$, and the efficiency increases slightly due to the higher fundamental component of class-AB operation. Consequently, it is expected that the efficiency slightly increases for a small increase of V_{GG}, but for higher changes of V_{GG}, the efficiency will drop.

To study the impact of the baseband fluctuation on the PA's performance, we used two-tone signals with a fixed peak amplitude. For narrowband operation, when the baseband frequency spectral lines do not overlap with the fundamental components, i.e., for the case where the two-tone frequency separation, $2\omega_m$, is much smaller than the carrier frequency, ω_c, the envelope amplitude can be interpreted as a change of the amplitude A in (6) and (7), whereas the baseband voltage fluctuation can be interpreted as a bias variation, V_{GG}.

As described in Section II, the amplitude modulation of the signal generates a baseband current in the nonlinear C_{GS} capacitance, as derived in (4). Since the nonlinear C_{GS} is modeled through a first-order polynomial, and we are assuming that the fundamental components are a pure two-tone excitation, the baseband current can only have one frequency component at the two-tone frequency separation, $2\omega_m$. This current is supplied through a nonzero complex bias impedance, Z_{S_BB}, and produces a sinusoidal bias voltage fluctuation at the intrinsic gate terminal. Distinct performance degradation patterns are generated depending on the amplitude and phase of Z_{S_BB}, that we explore in detail in Sections III-A–III-C.

A. Inductive Input Baseband Impedance

First, we consider the scenario where $Z_{S\_BB}(2\omega_m)$ is purely inductive, i.e., the situation that usually happens when PAs are excited with modulated signals whose bandwidth is below the input bias network parallel resonance frequency. From (5), it is observed that $v_{bb}(t)$ is delayed by 90° with respect to $i_{bb}(t)$ and, as this current is 90° in advance to the RF envelope voltage, the sinusoidal baseband voltage is added in-phase to the envelope of the two-tone signal, i.e., the minimum and maximum of both baseband and envelope amplitude occur at the same time. Fig. 11(a) presents the obtained bias fluctuation for three values of $|Z_{S_{BB}}|$ (which corresponds to an impedance, that is $0\times$, $25\times$, and $50\times$ higher than the fundamental impedance), i.e., three different inductances. Please note that we have included the short circuit to mimic the ideal class-B case.

For an intermediate amplitude level of baseband impedance, Z_{S_BB2}, in the low power region, the dc bias point becomes lower than the threshold voltage, imposing a class-C operation (or even cut-off at very low envelope amplitude). Therefore, in this region, the efficiency is degraded. Conversely, in the high-power region, the bias voltage increases and, thus, the PA
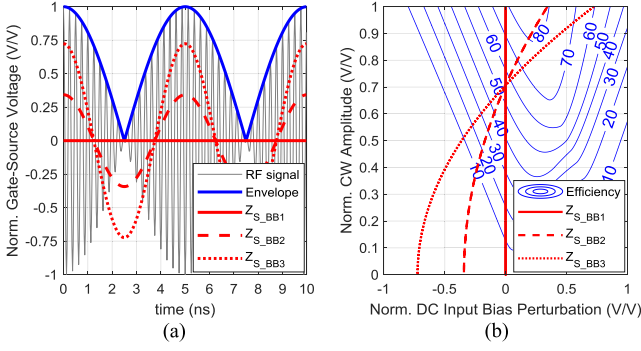
Fig. 11.   Model predicted (a) envelope of the two-tone signal and (b) efficiency contours, where the dynamic bias fluctuation for three different purely inductive baseband impedances are overlapped. The dc bias perturbation and the gate-to-source voltage are both normalized to $b_2 - b_1 = I_{max}/K_1$.
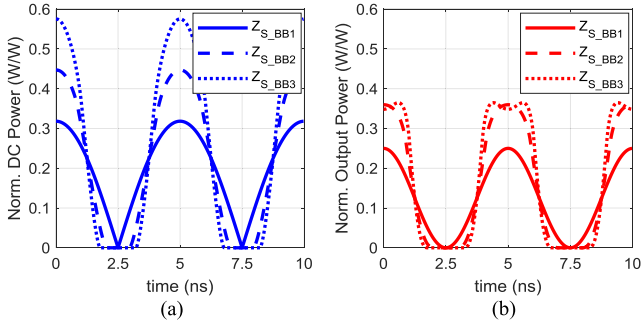

Fig. 12.   Model predicted (a) dc power and (b) fundamental power waveforms normalized to $I_{max} V_{DD}$ for three different purely inductive baseband impedances.
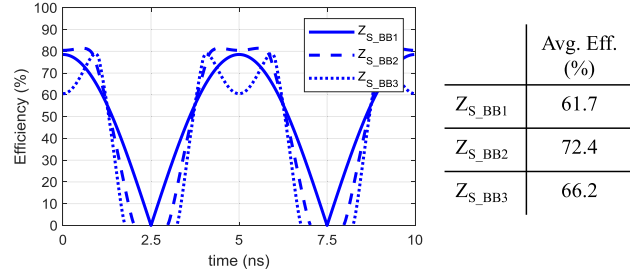

Fig. 13.   Model predicted instantaneous efficiency waveform for three different purely inductive baseband impedances and the respective average efficiency computed from the average dc and output powers.

becomes biased at class-AB. However, since the excitation amplitude is fixed, the peak voltage also increases, reaching the region where the instantaneous current starts to saturate, i.e., where the second i_{DS} piecewise linear branch starts to have an impact. At the intermediate power region, the bias fluctuation is very small, and therefore, the PA operates with the nominal class-B bias, showing nearly the same performance.

This variation of operation classes is in accordance with what was observed in the instantaneous dc and fundamental power waveforms, presented in Fig. 12, and in the respective instantaneous efficiency presented in Fig. 13.

For the selected Z_{S_BB2}, the second term of i_{DS} is not severely excited and, therefore, according to what was previously presented, the instantaneous efficiency is higher in the high-power region due to the class-AB bias, and lower at
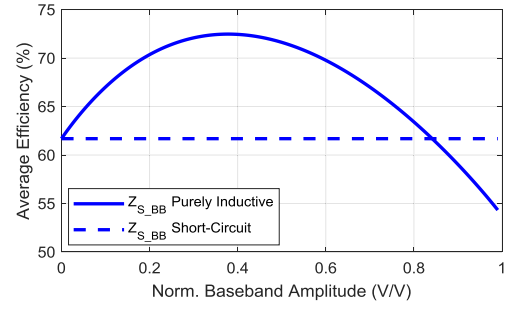

Fig. 14.   Model predicted two-tone average efficiency at several bias fluctuation amplitudes for a purely inductive bias impedance. The baseband amplitude is normalized to the peak amplitude of the two-tone signal, $b_2 - b_1 = I_{max}/K_1$.
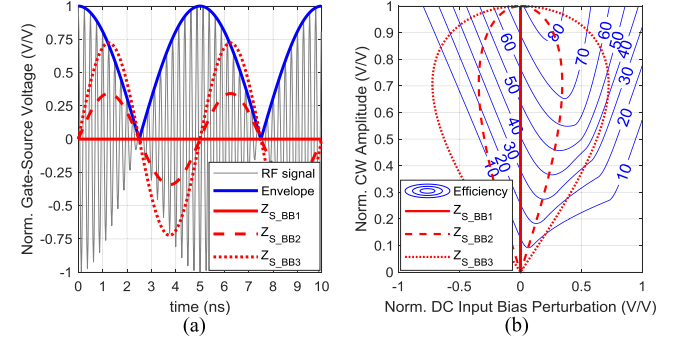

Fig. 15.   Model predicted (a) envelope of the two-tone signal and (b) efficiency contours, where the dynamic bias fluctuation for three different purely resistive baseband impedances are overlapped. The dc bias perturbation and the gate-to-source voltage are both normalized to $b_2 - b_1 = I_{max}/K_1$.

the low power region due to class-C operation with the same excitation amplitude. The instantaneous dc and output powers at the envelope high-power region will have more impact on the PA performance, since the PA will operate more time in this region according to the probability density function (PDF) of the two-tone signal envelope amplitude, being expected a higher average efficiency.

However, note that if the fluctuation is very high, i.e., higher baseband impedance, as it is the case of Z_{S_BB3}, or two-tone frequency separation, the PA becomes biased closer to class-A at the high-power region of the envelope and, therefore, the second term of i_{DS} becomes dominant, which results in an efficiency decrease. This can be observed in Fig. 14, where the bias fluctuation was swept.

Please note that, if the magnitude of $Z_{S\_BB}(2\omega_m)$ is sufficiently high, the baseband amplitude fluctuation can be so large that it biases the PA at class-A in the high-power region and at deep class-C in the low-power region. Therefore, the transistor's absolute maximum ratings may be crossed, permanently damaging the device.

B. Resistive Input Baseband Impedance (Resonance)

When $Z_{S\_BB}(2\omega_m)$ is purely resistive, e.g., when the input bias circuit reaches its parallel resonance, the baseband component and the RF envelope are in quadrature, following (5), and as shown in Fig. 15 for three different magnitudes of $Z_{S\_BB}(2\omega_m)$, which corresponds to an impedance that is $0\times$, $25\times$, and $50\times$ higher than the fundamental impedance.
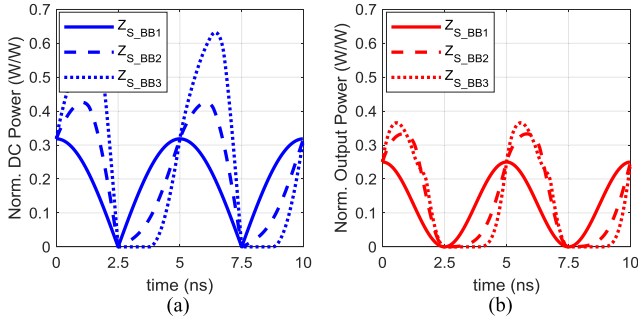
Fig. 16. Model predicted (a) dc power and (b) fundamental power waveforms normalized to $I_{\max}V_{DD}$ for three different purely resistive baseband impedances.
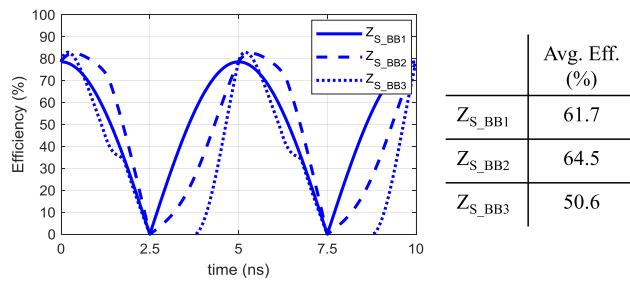

Fig. 17. Model predicted instantaneous efficiency waveform for three different purely resistive baseband impedances and the respective average efficiency computed from the average dc and output powers.
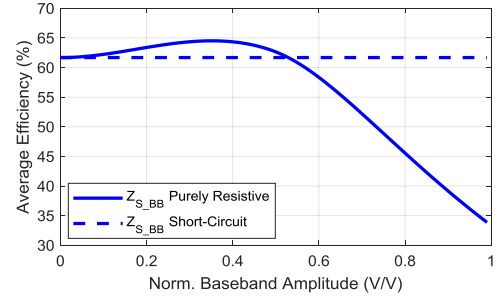

Fig. 18. Model predicted two-tone average efficiency at several bias fluctuation amplitudes for a purely resistive bias impedance. The baseband amplitude is normalized to the peak amplitude of the two-tone signal, $b_2 - b_1 = I_{\max}/K_1$.
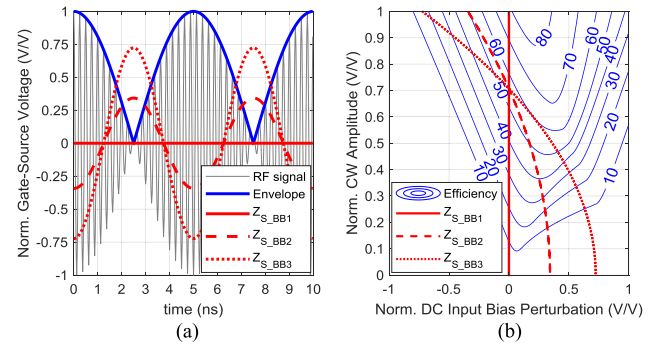

Fig. 19. Model predicted (a) envelope of the two-tone signal and (b) efficiency contours, where the dynamic bias fluctuation for three different purely capacitive baseband impedances are overlapped. The dc bias perturbation and the gate-to-source voltage are both normalized to $b_2 - b_1 = I_{\max}/K_1$.

If $Z_{S\_BB}(2\omega_m)$ is purely resistive, the obtained bias fluctuation is zero at both the high- and very low-power regions of the envelope. However, the maximum negative and positive bias fluctuations occur at mid-power levels on the ascending and descending envelope regions, respectively.

Thus, when the bias fluctuation is small (i.e., when the first term of the i_{DS} is dominant, as is the case of Z_{S_BB2}), an efficiency degradation is observed in the ascending envelope due to the class-C operation, but it is compensated by a similar efficiency increase in the descending envelope region, where it operates at class-AB.

Since the dc and output power curves are not purely symmetric with respect to the input bias, leading to the asymmetric efficiency contours presented in Fig. 15 (b), a slight increase in the average efficiency is expected for low baseband impedance. The waveforms of the instantaneous dc and output power and the respective efficiency are presented in Figs. 16 and 17, respectively.

However, if the bias fluctuation is sufficiently high (e.g., as is the case of Z_{S_BB3}), the PA becomes biased near class-A during part of the descending envelope where the $I_{1,2}$ term becomes dominant, and the efficiency decreases due to the lower output power, as we have seen previously in Fig. 10. Since the instantaneous efficiency now also degrades in the descending envelope, it is expected that the average efficiency decreases.

To observe this efficiency behavior, Fig. 18 presents the computed average efficiency as the baseband fluctuation is swept. As expected, for low amplitude bias fluctuation,

the average efficiency is unaffected and starts to degrade as the amplitude increases.

C. Capacitive Input Baseband Impedance

Finally, when $2\omega_m$ is already above the parallel resonant frequency, so that the baseband impedance at the envelope frequency $Z_{S\_BB}(2\omega_m)$ is purely capacitive, the RF envelope and the baseband voltage are in the opposite phase, according to (5), and as presented in Fig. 19 (again for three different magnitude values of $Z_{S\_BB}(2\omega_m)$, which corresponds to an impedance that is $0\times$, $25\times$, and $50\times$ higher than the fundamental impedance). Thus, the baseband fluctuation is at its minimum when the envelope is at the maximum amplitude and, conversely, at its maximum when the envelope amplitude is lowest.

Therefore, the PA operates at class-A with lower efficiency in the very low-power region of the envelope, and at class-C in the high-power region, where the efficiency is also lower due to the constant excitation amplitude. However, at the medium–low-power region, the efficiency is higher because the PA becomes biased at class-AB. This is what is shown in Figs. 20 and 21, for the dc and fundamental powers and efficiency, respectively.

Nevertheless, for a two-tone signal, the efficiency at the highest power region has the most impact on the average efficiency due to the PDF's profile. Therefore, we should always observe efficiency degradation in this scenario,
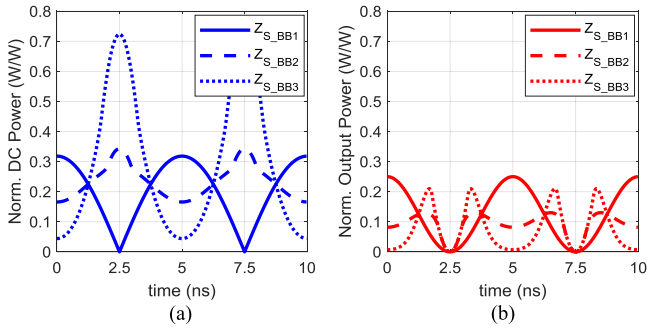
Fig. 20. Model predicted (a) dc power and (b) fundamental power waveforms normalized to $I_{\max}V_{DD}$ for three different purely capacitive baseband impedances.
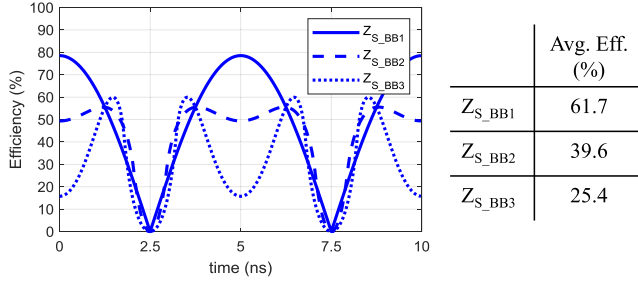

Fig. 21. Model predicted instantaneous efficiency waveform for three different purely capacitive baseband impedances and the respective average efficiency computed from the average dc and output powers.
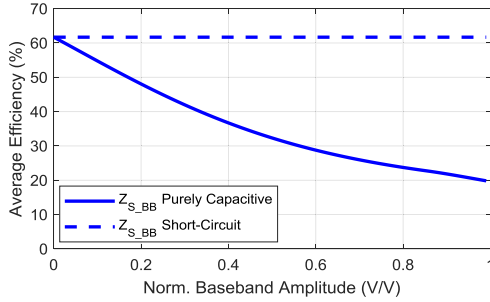

Fig. 22. Model predicted two-tone average efficiency at several bias fluctuation amplitudes and for a purely capacitive bias impedance. The baseband amplitude is normalized to the peak amplitude of the two-tone signal, $b_2 - b_1 = I_{\max}/K_1$.

regardless of the baseband fluctuation's amplitude. This is, indeed, the observed efficiency profile presented in Fig. 22, in which the baseband voltage amplitude is swept.

IV. EXPERIMENTAL RESULTS

In order to quantitatively evaluate the efficiency and linearity degradation expected in a real device, two PAs with different input bias networks were designed using Wolfspeed's CGH27030F GaN HEMT and implemented on a 0.76-mm Isola Astra substrate. A photograph of the implemented PAs is presented in Fig. 23 and the circuit IMNs representations for PA1 and PA2 and their OMN are presented in Figs. 24 and 25, respectively.

The IMN and OMN were designed to minimize the variation of the efficiency, output power, and gain profiles over a 650-MHz bandwidth span. The simulated and measured
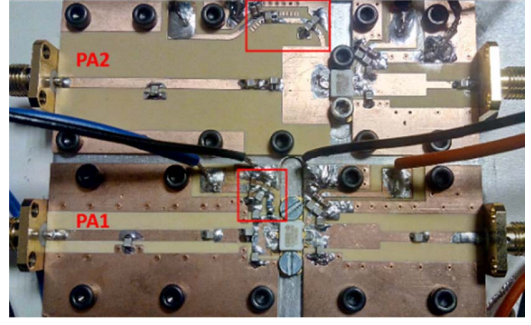

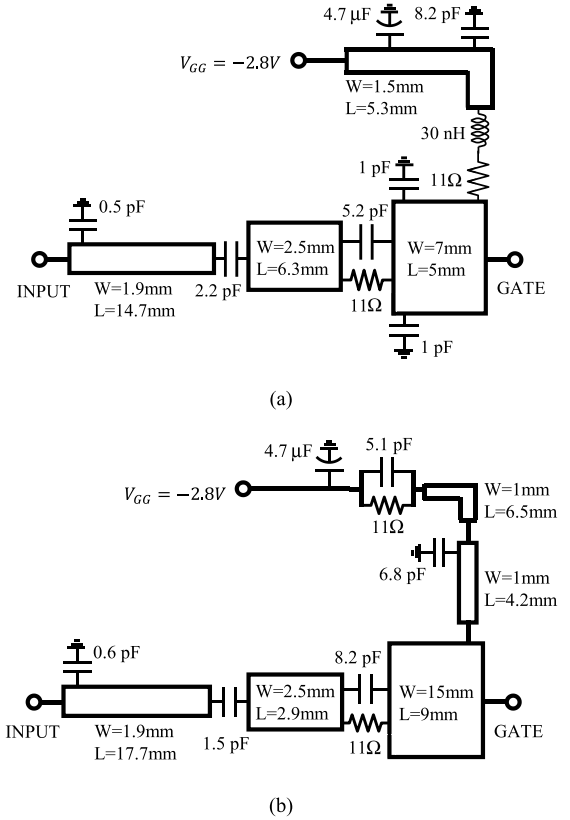Fig. 23. Photograph of the implemented PAs.

Fig. 24. IMN of (a) PA1 and (b) PA2.

efficiency, PAE, and output power of each PA, at the 2.5-dB compression level, are presented in Figs. 26 and 27, respectively.

While the OMN was optimally designed to obtain very low baseband impedance up to 1 GHz, the IMN of each PA was designed to present two distinct Z_{S_BB} profiles to evaluate efficiency and linearity degradation. One was conceived to correspond to the conventional structure previously presented in Fig. 2(a) (PA1), while another was appropriately designed to avoid a parallel resonance with the device's input impedance (PA2). This was achieved by adding a capacitor in parallel with the low-frequency stabilization resistor and by replacing the inductor by a short-length transmission line. In practice, this is the same as reducing the quality factor of the parallel resonant circuit and increasing the resonance frequency. With these changes, the input matching for the fundamental and the
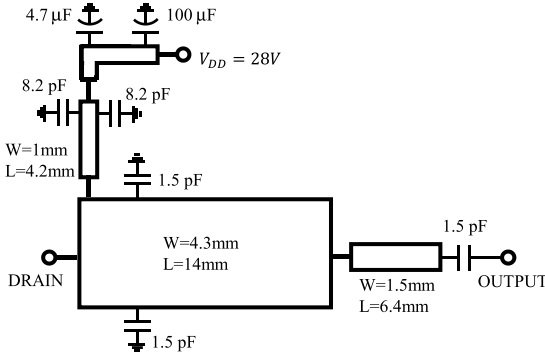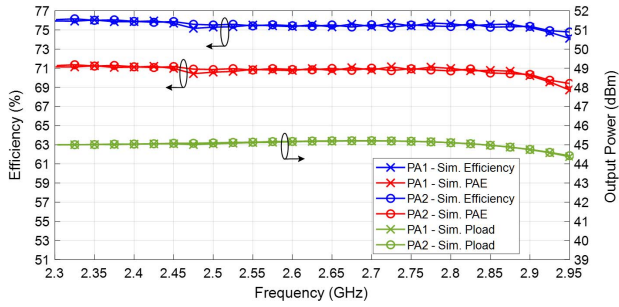
Fig. 25. OMN of the implemented PAs.

Fig. 26. Simulated efficiency, PAE, and output power under CW excitation, at the 2.5-dB gain compression point.
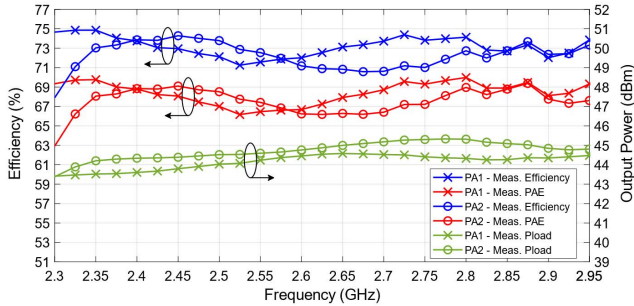

Fig. 27. Measured efficiency, PAE, and output power under CW excitation, at the 2.5-dB gain compression point.
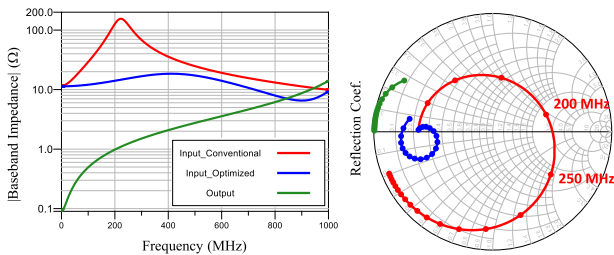

Fig. 28. Simulated baseband impedance profiles at the intrinsic gate and drain reference planes for the designed input and output networks.

bias circuit must be designed together since, without the large inductor, they will load one another. Both impedance profiles are presented in Fig. 28.

The dynamic behavior of the PA was assessed under a two-tone excitation, centered at 2.55 GHz, with a constant average available power of 26 dBm. The separation between the tones was swept between 10 and 400 MHz. The simulated and
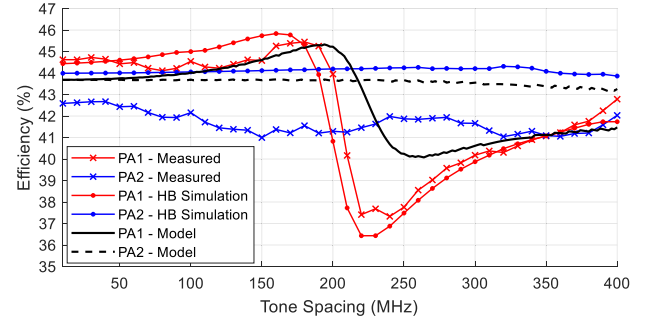

Fig. 29. Simulated, measured, and model predicted the average efficiency of both implemented PAs, under two-tone excitation.

TABLE I
MODEL PARAMETERS

Name	Value
K_1	1.23 S
b_1	-2.8 V
K_2	-0.98 S
b_2	-0.5 V
C_{gs0}	12.1 pF
C_{gs1}	1.27 pF/V

measured average efficiency is presented in Fig. 29, as reported in [13].

For PA1, both the simulated and measured average efficiencies have a sharp degradation of nearly 8% immediately above 200 MHz, where the impedance presented by the IMN at the baseband is closer to the parallel resonance. This is also the frequency region where the linearity of the PA is most degraded with an increase in the third-order IMD power of 15 dB, with respect to the initial tone separation of 10 MHz, as presented in the conference article [13].

Conversely, for the optimized network of PA2, both the efficiency and linearity remain nearly unchanged over the entire video bandwidth. The measured average efficiency is 2% lower at the lower tone separations and has higher variation over the instantaneous bandwidth than the one predicted by the simulation, which is attributed to the small differences in the CW figures of merit of each PA.

The theoretical model was validated by comparing the average efficiency behavior with the measurements as the tone separation increases. First, the model's parameters (K_n, b_n, and C_{GS} parameters) were fit to reproduce the performance of the implemented PAs under CW excitation, see Table I. Then, we computed the average efficiency for the same tone separation sweep and input available power that we used in the measurements. The computed average efficiency is presented in Fig. 29. The model is able to predict the qualitative behavior by presenting the same profile over the full frequency separation sweep.

The model also predicts the efficiency within a 2% tolerance, except in the 200–250-MHz tone separation range where the baseband impedance is very high and the first-order approximation of the C_{GS} capacitance is insufficient. In addition, since the model is built under the assumption that the RF envelope is independent of the generated baseband
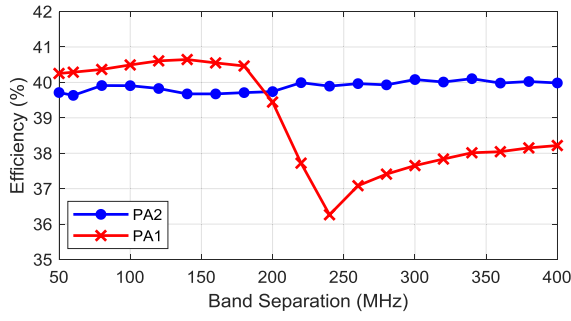
Fig. 30. Measured average efficiency of each implemented PA under concurrent dual-band LTE signals, with 5-MHz bandwidth, for several band separations.

Fig. 31. Measured ACPR of each implemented PA under concurrent dual-band LTE signals, with 5-MHz bandwidth, for several band separations.

distortion, this inaccuracy cannot be fully removed without using a recursive algorithm to accurately determine the intrinsic v_{GS} voltage.

Nevertheless, the frequency at which the efficiency degradation is maximum is predicted with an error of about 25 MHz that is usually enough for most PA applications where designers are interested in evaluating the instantaneous bandwidth.

Finally, we tested each PA in concurrent dual-band operation with 5-MHz orthogonal frequency-division multiplexing (OFDM) signals at each band with a peak-to-average power ratio (PAPR) of 9.7 dB. The separation between bands was swept from 50 to 400 MHz at a center frequency of 2.55 GHz. Power equalization was performed at the output, in single-band operation, to ensure that the PA is driven up to the same output peak power level in both bands and for all band separation values. The selected output power level was the one that would lead to a similar gain compression of 2.5 dB for each PA presented in Fig. 27.

First, the PA was driven at each band independently, i.e., in single-band operation, and the output signal was linearized using digital pre-distortion (DPD), obtaining in this way the desired reference condition and output peak power level. Then, both bands were driven simultaneously to measure the adjacent channel power ratio (ACPR) at each band and the average efficiency. Although the power equalization could be done by simply increasing the power of the input signal of each band, the benefit of DPD is that, conceptually, if the PA behaved linearly in the presence of both bands, the output signal would be undistorted. Therefore, the distortion that we now measure is a direct consequence of driving the PA with a wide concurrent band signal due to cross modulation.

The efficiency variation profile in PA1, presented in Fig. 30, closely follows the one predicted by the model and observed in the measurements with two-tone signals, as previously shown in Fig. 27. In addition, a clear degradation of the PA's linearity near the 200-MHz band separation is observed in the measured ACPR, which is presented in Fig. 31. This result complements the IMD3 measurements that were performed in [13], by showing that even if one could filter out the out-of-band IMD components at the output, the improper input baseband profile also generates in-band distortion that can only be removed with DPD.

In PA2, both the average efficiency and ACPR profiles are nearly flat near the 200-MHz band separation, which indicates that the cause of the observed degradation was eliminated.
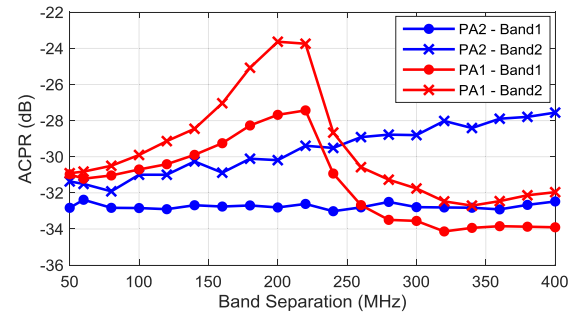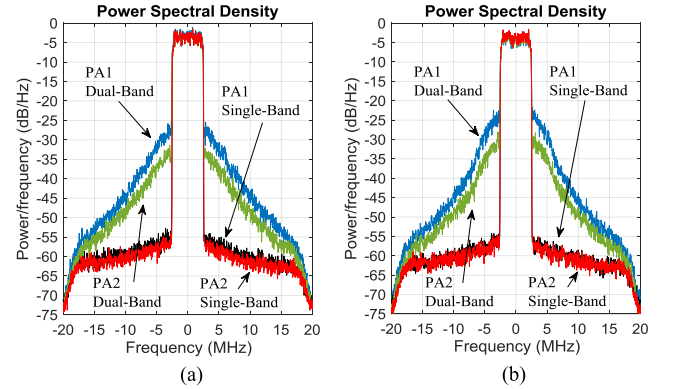

Fig. 32. Measured normalized output spectrum of the (a) left and (b) right fundamental bands, at an output peak power of 44.5 dBm, under single- and dual-band LTE excitations, with DPD, extracted for single-band operation.
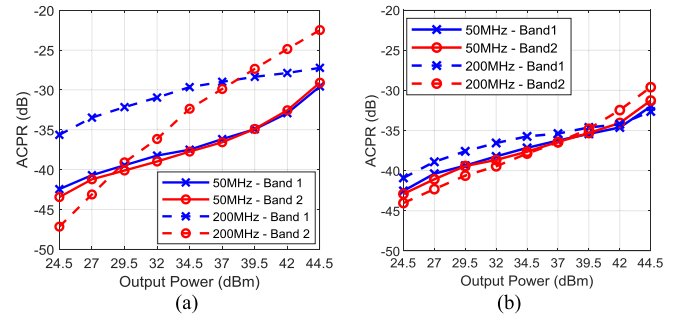

Fig. 33. ACPR of (a) PA1 and (b) PA2, when operated in concurrent dual-band excitation, measured for several output peak power levels at each band calibrated in single-band operation using DPD.

These results indicate that the efficiency degradation behavior predicted for two-tone signals is closely correlated with the one observed with real dual-band communication signals. The ability to roughly predict the efficiency degradation profile with a simple and analytic model is not only a significant improvement to the overall design process but also provides insight on the underlying degradation mechanisms that can be useful for higher complexity PAs.

The output spectra of both long-term evolution (LTE) bands, for the 200-MHz frequency spacing and at a peak output power of 44.5 dBm, are presented in Fig. 32. As observed, with the DPD correction performed for each band individually, we decreased the ACPR to −50 dBc at the desired output power level. Then, under concurrent band operation, the increase of distortion in PA1 is higher than the one observed for PA2.

Finally, the linearity degradation versus output power for the 50- and 200-MHz frequency separations is presented in Fig. 33. Naturally, both PAs present similar distortion behavior when the frequency separation is small. However, for the 200-MHz separation, a clear increase of the ACPR in PA1 is observed, even at low-power levels, whereas in the PA2, the ACPR profile is practically unchanged.

V. Conclusion

This article relates the limited PA efficiency performance observed in certain circumstances with the input network baseband terminations. The source of this limitation lies on the parallel network composed by the IMN baseband impedance termination and the device input capacitance, producing a large intrinsic gate voltage modulation at baseband frequencies. The corresponding PA conduction angle modulation leads to a degradation of both the linearity and efficiency. A simple theoretical model that predicts the qualitative efficiency variation profile of the PA under concurrent band operation was presented. We demonstrated that the model provides not only a qualitative understanding of the degradation mechanism but also an estimation of the input baseband impedance impact on the PA's performance.

This degradation mechanism was experimentally verified and demonstrates that if the IMN baseband impedances are not properly chosen, the PA can present an average efficiency much lower than the one obtained from the expected theoretical difference between the modulated and CW signals.

References

[1] X. Chen, W. Chen, G. Su, F. M. Ghannouchi, and Z. Feng, "A concurrent dual-band 1.9–2.6-GHz Doherty power amplifier with Intermodulation impedance tuning," in *IEEE MTT-S Int. Microw. Symp. Dig.*, Tampa, FL, USA, Jun. 2014, pp. 1–4.

[2] X. Chen, W. Chen, F. M. Ghannouchi, Z. Feng, and Y. Liu, "Enhanced analysis and design method of concurrent dual-band power amplifiers with intermodulation impedance tuning," *IEEE Trans. Microw. Theory Techn.*, vol. 61, no. 12, pp. 4544–4558, Dec. 2013.

[3] J. Li, W. Chen, F. Huang, and Z. Fend, "Multiband and multimode concurrent PA with novel intermodulation tuning network for linearity improvement," *IEEE Microw. Wireless Compon. Lett.*, vol. 28, no. 3, pp. 248–250, Mar. 2018.

[4] D. J. Williams, J. Leckey, and P. J. Tasker, "Envelope domain analysis of measured time domain voltage and current waveforms provide for improved understanding of factors effecting linearity," in *IEEE MTT-S Int. Microw. Symp. Dig.*, Philadelphia, PA, USA, vol. 2, Jun. 2003, pp. 1411–1414.

[5] B. Bunz, A. Ahmed, and G. Kompa, "Influence of envelope impedance termination on RF behaviour of GaN HEMT power devices," in *Proc. Eur. Gallium Arsenide Other Semiconductor Appl. Symp. (GAAS)*, Paris, France, Oct. 2005, pp. 649–652.

[6] Y. Hu, J. C. Mollier, and J. Obregon, "A Nevv method of third-order intermodulation reduction in nonlinear microwave systems," *IEEE Trans. Microw. Theory Techn.*, vol. MTT-34, no. 2, pp. 245–250, Feb. 1986.

[7] Y.-P. Kwon, Y.-C. Jeong, Y. Kim, and C.-D. Kim, "A design of predistortion linearizer using 2nd order low frequency intermodulation signal injection," in *Proc. IEEE 33rd Eur. Microw. Conf.*, Munich, Germany, Oct. 2003, pp. 249–252.

[8] M. Akmal, "Broadband baseband impedance control for linearity enhancement in microwave devices," *Int. J. Elect., Comput., Energetic, Electron. Commun. Eng.*, vol. 9, no. 8, pp. 953–959, Dec. 2015.

[9] I. Takenaka, K. Ishikura, H. Takahashi, K. Hasegawa, K. Asano, and N. Iwata, "Improvement of intermodulation distortion asymmetry characteristics with wideband microwave signals in high power amplifiers," *IEEE Trans. Microw. Theory Techn.*, vol. 56, no. 6, pp. 1355–1363, Jun. 2008.

[10] M. J. Pelk, L. C. N. de Vreede, M. Spirito, and J. H. Jos, "Base-band impedance control and calibration for on-wafer linearity measurements," in *Proc. ARFTG 63rd Conf. Spring*, Fort Worth, TX, USA, 2004, pp. 35–40.

[11] M. Akmal et al., "The effect of baseband impedance termination on the linearity of GaN HEMTs," in *Proc. IEEE 40th Eur. Microw. Conf.*, Paris, France, Sep. 2010, pp. 1046–1049.

[12] L. C. Nunes, D. R. Barros, P. M. Cabral, and J. C. Pedro, "Efficiency degradation analysis in wideband power amplifiers," *IEEE Trans. Microw. Theory Techn.*, vol. 66, no. 12, pp. 5640–5651, Dec. 2018.

[13] D. R. Barros, L. C. Nunes, P. M. Cabral, and J. C. Pedro, "Impact of the input baseband impedance on the instantaneous bandwidth of wideband power amplifiers," in *IEEE MTT-S Int. Microw. Symp. Dig.*, Boston, MA, USA, Jun. 2019, pp. 1–4.

[14] L. C. Nunes, P. M. Cabral, and J. C. Pedro, "AM/AM and AM/PM distortion generation mechanisms in Si LDMOS and GaN HEMT based RF power amplifiers," *IEEE Trans. Microw. Theory Techn.*, vol. 62, no. 4, pp. 799–809, Apr. 2008.

[15] C. Fager, J. C. Pedro, N. B. de Carvalho, H. Zirath, F. Fortes, and M. J. Rosario, "A comprehensive analysis of IMD behavior in RF CMOS power amplifiers," *IEEE J. Solid-State Circuits*, vol. 39, no. 1, pp. 24–34, Jan. 2004.

[16] J. C. Pedro, L. C. Nunes, and P. M. Lavrador, "A new large-signal intermodulation and spurious analysis tool," in *IEEE MTT-S Int. Microw. Symp. Dig.*, Seattle, WA, USA, Jun. 2013, pp. 1–4.

Diogo R. Barros (S'14) was born in Penalva do Castelo, Portugal, in 1990. He received the M.Sc. degree in electronics and telecommunications engineering from the University of Aveiro, Aveiro, Portugal, in 2015, where he is currently pursuing the Ph.D. degree in electrical engineering.

He has been a Junior Researcher with the Institute of Telecommunications, Aveiro, since 2016. His current research interests include nonlinear distortion analysis, wideband high-efficiency PA design, and advanced MISO Doherty-outphasing power amplifier architectures.

Mr. Barros is a Student Member of the IEEE Microwave Theory and Techniques Society (IEEE MTT-S) and a member of the IEEE MTT-S Student Branch Chapter at the University of Aveiro.

Luís C. Nunes (S'13–M'17) was born in Guarda, Portugal, in 1986. He received the M.Sc. and Ph.D. degrees in electrical engineering from the University of Aveiro, Aveiro, Portugal, in 2010 and 2015, respectively.

From 2016 to 2017, he was an RF Design Engineer with Huawei Technologies Sweden AB, Kista, Sweden. He is currently a Researcher Assistant with the Institute of Telecommunications, Aveiro. His current research interests include active device modeling, nonlinear distortion analysis, and the design of microwave circuits, especially high-efficiency and linear power amplifiers.

Dr. Nunes is a member of the IEEE Microwave Theory and Techniques Society and the IEEE Electron Devices Society.

IEEE TRANSACTIONS ON MICROWAVE THEORY AND TECHNIQUES, VOL. 67, NO. 12, DECEMBER 2019

Pedro M. Cabral (S'04–M'07–SM'16) was born in Aveiro, Portugal, in 1979. He received the Electrical Engineering and the Ph.D. degrees from the University of Aveiro, Aveiro, Portugal, in 2002 and 2006, respectively.

He is currently a Senior Researcher with the Institute of Telecommunications, Aveiro, and an Assistant Professor with the University of Aveiro. His current research interests include active device nonlinear modeling, design of microwave circuits, high-efficiency power amplifiers, and wireless transmitter architectures.

Dr. Cabral has been a reviewer for several publications, including the IEEE Transactions on Microwave Theory and Techniques, the IEEE Transactions on Computer-Aided Design of Integrated Circuits and Systems, the IEEE Transactions on Instrumentation and Measurement, and the IEEE Transactions on Circuits and Systems—I: Regular Papers.

José Carlos Pedro (S'90–M'95–SM'99–F'07) received the Diploma, Ph.D. and Habilitation degrees in electronics and telecommunications engineering from the University of Aveiro, Aveiro, Portugal, in 1985, 1993, and 2002, respectively.

He is currently a Full Professor with the University of Aveiro. His current research interests include active device modeling and the analysis and design of various nonlinear microwave circuits. He is the leading author of two books and has authored or coauthored more than 200 articles in international journals and symposia.

Prof. Pedro received various prizes, including the Marconi Young Scientist Award in 1993, the 2000 Institution of Electrical Engineers Measurement Prize, the 2015 EuMC Best Paper Microwave Prize, and the Microwave Distinguished Educator Award. He has served the scientific community by acting as a reviewer and editor of several conferences and journals, including the IEEE Transactions on Microwave Theory and Techniques. He is currently the Editor-in-Chief of the IEEE Transactions on Microwave Theory and Techniques.